2016

INVESTIGATION AND MODELING OF Al3(Sc, Zr) PRECIPITATION STRENGTHENING IN THE PRESENCE OF ENHANCED SUPERSATURATION AND WITHIN Al-Cu BINARY ALLOYS

Kyle Deane
Michigan Technological University, kjdeane@mtu.edu

INVESTIGATION AND MODELING OF $Al_3(Sc, Zr)$ PRECIPITATION STRENGTHENING IN THE PRESENCE OF ENHANCED SUPERSATURATION AND WITHIN Al-Cu BINARY ALLOYS

By

Kyle Deane

A DISSERTATION

Submitted in partial fulfillment of the requirements for the degree of

DOCTOR OF PHILOSOPHY

In Materials Science and Engineering

MICHIGAN TECHNOLOGICAL UNIVERSITY

2016

This dissertation has been approved in partial fulfillment of the requirements for the Degree of DOCTOR OF PHILOSOPHY in Materials Science and Engineering.

Department of Materials Science and Engineering

Dissertation Advisor: *Paul Sanders*

Committee Member: *Stephen Kampe*

Committee Member: *Douglas Swenson*

Committee Member: *Timothy Eisele*

Department Chair: *Stephen Kampe*

Contents

Acknowledgements

I would like to express my deepest gratitude for my advisor, Dr. Paul Sanders, for all the help and guidance he has given over the last several years. Even before I began my journey through graduate school, he gave me the opportunity to lead my own research projects through the Advance Metalworks Enterprise and paid undergraduate research work. He has continued to guide and support me as I tackled the work discussed in this dissertation, and the experience and knowledge I've gained will prove invaluable as I move forward with my career after graduate school.

I would like to thank my committee members, Dr. Stephen Kampe, Dr. Douglas Swenson, and Dr. Timothy Eisele, for reviewing my paper and giving me valuable suggestions for future work.

I would like to thank Dr. Stephen Kampe and Dr. Douglas Swenson further for sharing their expertise over the years as we collaborated on the HSLA Aluminum project. A large portion of my work was built on the principles and techniques I learned as a student in their courses, and it was very helpful to receive their input and guidance as I continued to learn through my research.

I would like to thank the faculty and staff of the Materials Science and Engineering Department, for their support and friendship. I would especially like to thank Paul Fraley, Thomas Wood, and Patrick Quimby for guiding me as I navigated the endless seas of equipment failure and technical issues that is graduate school. Without these fine gentlemen we would all be lost. I would also like to add a shout out to Dr. Dan Seguin, for gladly helping me with TEM work even when he had a seemingly full schedule.

I would like to thank all of my fellow graduate students, for the countless brainstorming sessions, cookouts, and good times that kept us all sane. I would especially like to thank Dr. Joseph Licavoli for being one of my biggest mentors in my early research career and for continuing to let me bounce ideas and issues off of him even after he moved across the country. I also must extend my heartfelt gratitude to Zachary Morgan for diving into my Matlab model with me to unravel all of the bugs I had been struggling with for months. I would also like to thank Mathew Tianen for letting me stay in his house when the funding for my project expired, and for keeping me company as I worked long hours writing this document.

I would like to thank all my family and friends for continuing to be supportive of me, and continuing to remember that I exist as the years I've spent in Houghton (the distant wilderness of the UP) creeps closer and closer to double digits.

Lastly, I would like to thank my wife, Dr. Jie Li. She has become the best part of every day, whether she's cooking delicious food for me during long writing sessions, or helping me find laughter and joy in-between. I really don't know how I could have gotten to this point in my research without her, and I'm happy to say that she's stuck with me forever.

Abstract

Diffuse Al-Sc and Al-Zr alloys have been demonstrated in literature to be relatively coarsening resistant at higher temperatures when compared with commonly used precipitation strengthening alloys (e.g. 2000 series, 6000 series) [1–3]. However, because of a limited strengthening due to the low solubility of scandium and zirconium in aluminum[4,5], and owing to the scarcity and therefore sizeable price tag attached to scandium [6], little research has been done in the way of optimizing these alloys for commercial applications.

With this in mind, this dissertation describes research which aims to tackle several important areas of Al-Sc-Zr research that have been yet unresolved. In Chapter 4, rapid solidification was utilized to enhance the achievable supersaturation of the alloy in an effort to increase the achievable precipitate strengthening. In Chapter 5, Additive Friction Stir processing (AFS), a novel method of mechanically combining materials without melting, was employed in an attempt to pass the benefits of supersaturation from melt spun ribbon into a more structurally useful bulk material. In Chapter 6, a Matlab program written to predict precipitate nucleation, growth, and coarsening with a modified Kampmann and Wagner Numerical (KWN) model, was used to predict heat treatment regimens for more efficient strengthening. Those predictions were then tested

experimentally to test the validity of the results. And lastly, in Chapter 7, the effect of zirconium on Al-Cu secondary precipitates was studied in an attempt to increase their thermal stability, as much higher phase fractions of Al-Cu precipitates are achievable than Al-Zr precipitates.

Chapter 1: Introduction

1.1 Research Goals

The research discussed in this dissertation was undertaken to achieve a greater knowledge of the Al-Sc and Al-Zr systems, and more specifically to apply this knowledge toward the goal of making these alloys more useful in an industrial or military setting. Current usage of dilute Al-Sc and Al-Zr alloys is limited in part because of financial concerns, but also due to the limited strengthening achievable in these alloys. This work approached this goal through the completion of several tasks:

1. Quantify the potential strengthening benefit of artificially increased supersaturation through rapid solidification.
2. Discover methods for and explore feasibility of creating structurally useful forms out of supersaturated, rapidly solidified ribbon.
3. Determine efficient heat treatment regimens for achieving peak strength in these dilute alloy systems through the use of accurate predictions of precipitation behavior.

4 Determine if Zr can decrease the coarsening rate of precipitates found in commonly used alloys and essentially increase the magnitude of thermally stable strength while avoiding the use of costly scandium.

1.2 Motivations for Research

The main motivation for this research is to add to the wealth of knowledge on dilute Al-Sc and Al-Zr alloys with a goal of making these alloys more accessible for industrial and/or military use. Currently Al-Sc alloys are somewhat limited to high-end sporting equipment such as tennis rackets and bike frames [1,2], largely due to the fact that Sc is not actively mined and is therefore expensive [6]. A better understanding of these alloys could potentially lower their cost drastically, as a demonstration that higher strengthening is possible with new heat treatment schedules and/or methods for supersaturation could increase the demand for Sc and facilitate the opening of new Sc sources. A better understanding of how Sc and Zr interact with other Al-based precipitates could also potentially lower the quantity of Sc or Zr needed to achieve thermally stable microstructural features, which would in turn lower the cost of these alloys and make them more accessible for everyday use.

1.3 Organization of the Dissertation

This dissertation, continuing in the following chapters, begins with general background in Chapter 2. This background includes information about precipitate strengthening in Al alloys, the effect of increasing temperatures on that strength, reasoning for looking into

the elemental additions that were chosen for this project, a discussion of the current and historical use of Al-Sc and Al-Zr alloys, and methods of achieving and maintaining supersaturation. In Chapter 3, all experimental techniques used in this research are displayed in detail. These methods are also more briefly mentioned in the experimental chapters as they are discussed in order to facilitate flow and show the particular parameters.

Chapters 4 through 7 deal primarily with specific experiments that were performed to achieve several different goals. The first two of these experimental chapters discuss research into creating and using overly supersaturated Al-Sc and Al-Zr alloys with the help of melt spinning and AFS. Following these chapters is another experimental chapter discussing work done into prediction of precipitate behavior in dilute Al_3Sc alloys towards the final goal of developing efficient heat treatment regimens to quickly achieve the maximum potential of strengthening. Then, the final experimental chapter describes work done in an attempt to thermally stabilize Al-Cu precipitates with additions of slow-diffusing Zr so as to lock in a greater phase fraction of optimally strengthening precipitation phase than is possible with Zr alone. The dissertation is finally capped off with a conclusion chapter which summarizes the results and conclusions discussed in each of the experimental chapters.

Chapter 2: Background

2.1 General Overview of Sc and Zr Usage in Al Alloys

Aging in dilute Al-Sc alloys has been observed to form coherent L12 precipitates [1,7]. These precipitates demonstrate a higher thermal stability than more traditional precipitation strengthening Al alloys (eg. Al-2xxx, Al-6xxx), meaning that Al-Sc alloys can be used at higher temperatures than those alloys without the unwanted coarsening and overaging of strength that results. As depicted in Table 2.1, this increased thermal stability is a result of Sc having a relatively low diffusivity in Al when compared to other common precipitating additions such as Cu, Si, and Mg, as the coarsening kinetics become bottlenecked by the low mobility of solute atoms. In addition, a mismatch strain of only 1.32% between the matrix and the L12 Al_3Sc precipitate phase [8] allows for a relatively stable precipitate interface and a limited driving force for coarsening [7]. Sc has a limited solubility below 673K (400˚C) of <0.01at% [9], meaning that the vast majority of solute atoms in the matrix can be precipitated out during aging to increase the strength. However, one downside to using Sc as a strengthening addition is that it has a low maximum equilibrium solubility of only 0.23 at% at the eutectic temperature [7].

Table 2.1: Diffusivities of Precipitate Forming Al Alloy Additions

Element	**Si** [10]	**Cu**[11]	**Mg** [12]	**Sc** [13]	**Zr** [14]
$\mathbf{D_{673K(400^{\circ}C)}}$ **m²/s**	3.5×10^{-13}	1.5×10^{-15}	9.4×10^{-15}	2.0×10^{-17}	1.2×10^{-20}

Al-Sc alloys were first developed in the former Soviet Union and used in MiG 29 aircraft and other aerospace applications [1]. Currently they have found a market in light weight, fatigue resistant high-end sporting equipment, such as baseball bats and bicycle frames [2]. One of the key factors slowing their adoption into other industries such as the automotive or aerospace industries is the general scarcity and cost of Sc. This scarcity is not due to a lack of Sc abundance on Earth; it is instead due in large part to it being found almost exclusively as trace quantities and extracted only as a byproduct from other mineral operations and old tailing piles [2,6]. It is generally believed that sufficient interest in these alloys would drive the cost of Sc down as new operations would open up to meet industrial demand [1].

A commonly researched supplemental addition in Al-Sc alloys is zirconium, as it has a lower diffusion coefficient than Sc and forms a metastable, coherent L12 precipitate. These properties, when combined with the right heat treatment regimen, result in an aged microstructure in which the precipitates have Sc-rich cores and Zr-rich outer shells [1]. Heat treatments to this effect should incorporate multiple heat treatment steps, as the kinetics between Sc and Zr are different enough that a single step heat treatment would precipitate one nicely while neglecting the other. If achieved, the external shell of Zr acts to limit the coarsening behavior of the Sc atoms at temperatures up to 723K (450˚C) [15]

because of a diffusivity two orders of magnitude smaller than that of Sc and a mismatch strain of only 0.75%. While Zr also benefits from solvus concentrations below 0.01 at% below 673K (400˚C) [5], the drawback of using Zr in this manner is that it has an even smaller maximum equilibrium solubility in Al than Sc does, at only 0.078 at% [7].

These trialuminide precipitates offer the most strength to the alloy when the order strengthening mechanism is dominant at precipitate radii between 1 and 3 nm [16–18]. At larger radii, Orowan strengthening becomes dominant as it becomes more efficient for dislocations to loop around precipitates than shear through them [16,19–21]. Both mechanisms provide increased strength with an increase in total phase fraction of the precipitate phase, but Orowan strengthening is also dependent on the average radius of the precipitates (given a known phase fraction), decreasing in effect as the radii increase. This is because Orowan strengthening depends largely on the distance between precipitates, and the only way to increase precipitate radius at constant phase fraction is through coarsening. During coarsening, smaller precipitates dissipate to provide the necessary atoms for growth in the more energetically favorable larger precipitates. This dissolution effect lowers the number density of precipitates and in turn increases the inter-precipitate spacing.

2.2 Precipitate Strengthening Mechanisms in Aluminum

Strengthening in aluminum alloys is commonly achieved through the use of precipitation strengthening, whereas a solid solution is aged at a temperature within a two phase region

of the phase diagram to cause nucleation and growth of finely dispersed crystals of a second phase. These precipitates formed during aging can strengthen the material by impeding dislocations in several ways, related to factors such as difference in lattice parameter, crystal structure, crystalline order, and shear modulus. In general, if no change in average precipitate radius or structure is observed, an increase in precipitate phase fraction will result in an increased strength. Changes in average precipitate radius can either predictably increase or decrease the strengthening effect, depending on the strengthening mechanisms that are currently dominant. The relevant strengthening mechanisms for FCC aluminum matrix phase with coherent $L1_2$ precipitates are discussed in 2.2.1 through 2.2.3. These mechanisms are:

1. Coherency and Mismatch Strengthening – These mechanisms impede dislocation motion due to the strain in the matrix associated with stretching to bond with coherent precipitates of slightly differing lattice parameters (coherency strengthening) and due to differences in shear modulus between the precipitate and matrix phase causing the dislocation line tension to be altered (mismatch strengthening). These mechanisms are discussed together as they are both at their most effective strengthening at coherent precipitate-matrix interfaces during precipitate shearing dislocations, and should therefore be considered to increase the strength together [19,20].

2. Order Strengthening – This mechanism impedes dislocation motion due to the energy increase associated with disrupting the organization of an ordered

precipitate (such as in Al_3X) as a dislocation shears through it. This antiphase boundary energy, as it is referred to, is at a maximum as the dislocation shears through the center of a precipitate, so it is does not stack with and is considered separately from the coherency and mismatch mechanisms [19,20].

3. Orowan Strengthening – This mechanism occurs as the precipitates become too large to shear and dislocations can only pass precipitates through dislocation looping. Because dislocation looping and precipitate shearing are directly competing methods of dislocation motion, this mechanism does not stack with any of the previously mentioned precipitation strengthening mechanisms and is considered separately [19,20].

2.2.1 Mismatch and Coherency Strengthening

Mismatch and coherency strengthening are unique mechanisms with differing causes and behavior, which will be examined in this section. However, as mentioned in the last section, they will be discussed together here because the mechanisms are complementary to each other as they both offer the greatest strength increase as dislocations pass through the precipitate-matrix interface. As a counterexample, the greatest order strengthening effect occurs as dislocations pass through the center of the precipitates, where the effect of mismatch and coherency is at a minimum. For this reason, the order strengthening effect is not added to the combined mismatch and coherency strengthening effects, but is instead viewed as a competing mechanism.

Coherency strengthening can be thought of as an extension of solid solution strengthening due to solute atom size, in that the base cause of strengthening is due to differences in size between average atomic radii in the precipitate phase and in the matrix. In precipitates where the average atomic radius is similar to that of the matrix but not identical, coherent atomic bonding will occur at the precipitate-matrix interface. The slight changing of lattice parameters as the interface is crossed creates a strain field in both phases, which lessens with distance from the interface. As dislocations move through the material, a greater amount of energy is required to move through the strain fields associated with these effects, resulting in an observable strengthening of the material. Mismatch strengthening is a phenomenon caused by the differences in shear modulus values between the precipitate and matrix phase. As a dislocation enters a precipitate while passing through the material, the dislocation line tension is changed [19,20].

Mismatch strengthening is described by Equation 2.1 [19], where M is the Taylor mean orientation factor of 3.06 for multicrystalline Al [22], G_p is the shear modulus of the precipitate, 68 GPa [23,24], and G_m is the shear modulus of the matrix, 25.4 GPa [28]. The magnitude of the Burgers vector of aluminum, b, is 0.286 nm [28], the phase fraction is denoted as f, and the average radius is denoted as $\overline{R}$.

$$\sigma_{mis} = 0.0078 * M * \sqrt{\frac{f}{G_m} * \left(G_p - G_m\right)^3} * \left(\frac{\overline{R}}{b}\right)^{0.275} \qquad \text{(Eqn. 2.1)} \qquad [19]$$

Coherency strengthening is described by Equation 2.2 [19], where M is the Taylor mean orientation factor of 3.06 for multicrystalline Al [22], and G_m is the shear modulus of the matrix, 25.4 GPa [25]. The Burgers vector of aluminum, b, is 0.286 nm [28], the phase fraction is denoted as f, and the average radius is denoted as $\overline{R}$. The lattice parameters of the matrix and precipitate phase are denoted as a_m and a_p respectively.

$$\sigma_{coh} = 2 * M * G_m * \sqrt{\frac{\overline{R}f}{b} * \left(\frac{a_p - a_m}{a_m}\right)^3} \qquad \text{(Eqn. 2.2)} \qquad [19]$$

2.2.2 Order Strengthening

Order strengthening is a mechanism wherein dislocations are impeded due to the preference of stoichiometric precipitate phases to order themselves in a predictable manner. For various reasons, these preferred structures help minimize the energy in the system, and any deviation from the ideal structure results in an increase in energy known as an antiphase boundary energy (APBE). Assuming that the precipitates are able to be sheared (not so large or brittle that another mechanism becomes dominant), a dislocation moving through an ordered precipitate systematically converts preferred A-B bonding into A-A and B-B bonds across the slip plane, creating a strengthening effect in the material roughly proportional to the phase fraction of the precipitate phase [20].

This approach to understanding order strengthening can be acceptable in some systems, but it is important to note that in some systems it is too simple. As described in the last

paragraph, order strengthening derives its strength from the APBE associated with disordering ordered precipitates. However, the disorder left in the wake of a dislocation essentially attracts other incoming dislocations in order to restore the original order, which negates the strengthening effect of the original dislocation. If this effect was unchallenged by competing factors, paired dislocations would move easily through the sample, and order strengthening would be a non-entity within the given material. The reason that order strengthening is an important mechanism in some materials is entirely due to competition from the intrinsic repulsion between dislocations. The competition between these two forces dictates the separation between dislocations. If the ratio of $APBE/G_b$ is small, there is little benefit to traveling as pairs, so it is assumed dislocations travel alone and can cause order strengthening. If the ratio is large, the benefit to traveling in pairs far outweighs the cost, and order strengthening is not observed due to near instantaneous negation of the APBE [20]

.

Order strengthening is described by Equation 2.3 [19,20], where M is the Taylor mean orientation factor of 3.06 for multicrystalline Al [22], and G_p is the shear modulus of the precipitate, 68 GPa. [23,24] γ_{APB}, the precipitate antiphase boundary energy, is taken to be ~0.5 J/m^2 for the (111) plane [16,23,24,27,25,26]. The Burgers vector of aluminum, b, is 0.286 nm [28], and the phase fraction is denoted as f.

$$\sigma_{ord} = 0.44 M G_p \frac{\gamma_{APB}}{b} f^{1/2} \qquad \text{(Eqn. 2.3)} \qquad [19,20]$$

From this equation it is clear that the order strengthening effect does not vary with precipitate radius change, but increases with phase fraction. This means that the order strengthening effect increases during phase formation (both nucleation and growth) and reaches a plateau when the solute levels reach equilibrium.

2.2.3 Orowan Strengthening

Orowan strengthening, also referred to as dislocation looping or bowing, differs from the previously mentioned mechanisms in that the dislocation never cuts through the precipitates. This scenario generally occurs either with precipitates that are incoherent with the matrix or with coherent precipitates that have become too large and therefore resistant to shearing [19,20].

When a dislocation becomes pinned on such a "hard obstacle," it is impossible for the dislocation to continue unchanged. Unpinned sections of the dislocation will continue to move forward, increasing the length of the dislocation front by deviating from the initially relatively linear front. As the dislocation continues to pull forward, the sections of the dislocation front immediately adjacent to the pinning location will bow around the precipitate, eventually becoming close enough to each other on the backside to combine. At this point, the trailing sections of the dislocation front are also combined and can be "pinched off" and move forward with the front unimpeded. A small dislocation loop is left around the precipitate, giving rise to the nomenclature [19,20].

Orowan strengthening is described by Equations 2.4 and 2.5 [19,20], where G_m, the shear modulus of the matrix, is taken to be 25.4 GPa [23], and v is the Poisson's ratio for Al at 0.345 [22]. The average precipitate radius, $\overline{R}$, is calculated from the LSW lines described in previous sections, and the edge-to-edge interprecipitate spacing, λ_{e-e}, is estimated geometrically using the average precipitate radius and the phase fraction.

$$\sigma_{or} = \frac{0.4MG_m b * \ln\left(\frac{2\bar{R}}{b}\right)}{\pi\lambda_{e-e}\sqrt{1-v}} \qquad \text{(Eqn. 2.4)} \qquad [19,20]$$

$$\lambda_{e-e} = \bar{R}\left(\sqrt{\frac{2\pi}{3f}} - \frac{\pi}{2}\right) \qquad \text{(Eqn. 2.5)} \qquad [19,20]$$

From this equation it can be determined that the Orowan strengthening effect increases with phase fraction but simultaneously decreases with growing precipitate radius. This results in an initial increase in strength as precipitate phase is formed, followed by an overaging effect as coarsening continues to increase the average precipitate size at later heat treatment steps even after all possible precipitate phase is formed [19,20].

2.2.4 Determining Dominance in Strengthening Mechanisms

Determining which strengthening mechanisms are dominant at different stages of the precipitation progression can be accomplished by calculating the theoretical strengthening effects of each potential mechanism and understanding how the different mechanisms interact with each other [19,20].

In general it can be assumed that a dislocation will take the easiest path through a material. For example, if the potential strengthening effect of shearing an ordered precipitate (ordered strengthening) is lower than that of looping around the precipitate (Orowan strengthening), then the precipitate will be sheared. This is highly intuitive, as it would be strange for a dislocation to be pinned by and loop around a precipitate if it was easily able to shear through it. If instead the Orowan strengthening effect is lower, then the dislocation will loop around the precipitate. Recall that the two methods in question react differently to average radius change (with a constant precipitate phase fraction), meaning that, as the precipitate radii increase, the dominance will shift from Order strengthening to Orowan strengthening as Orowan strengthening diminishes [19,20].

The nature of the mechanism also has to be taken into account. In the example discussed in the last paragraph with Order and Orowan strengthening, the strengthening effects cannot be added to each other as only one mechanism can be at play at a time. However, as mentioned in section 2.1.1, Mismatch and Coherency strengthening happen simultaneously, meaning that their strengthening effects stack. In such a case, the potential strengthening of the stacking mechanisms must be lower than the individual strength of each competing mechanism (such as Order and Orowan) in order to be dominant. In this research, the Mismatch and Coherency combined strengthening effect is only dominant at very low radii (generally less than 1nm), so the majority of strengthening observed is due to either Order or Orowan strengthening [19,20].

2.3 Effect of Solidification Rate on Achievable Supersaturation

Interest in increasing the strengthening potential of Al-Sc and Al-Zr alloys is quickly met with the issue of limited solubility. While the general shape of the solvus line in both binary alloys, only showing significant solubility concentrations at elevated temperatures, is conducive to precipitate strengthening, the maximum solubilities for these systems when held slightly below the eutectic temperature are restrictively low (0.078at%Zr and 0.23at%Sc) [4,5]. One potential way to overcome such a limitation is to solidify these alloys from the melt rapidly enough that there is minimal time for the Sc and/or Zr atoms to arrange themselves as the second phase. In such a way, it is possible to create alloys with supersaturated solid solutions comparatively higher than with conventional casting methods [3]. However, there are some limitations of this approach, which will be outlined in the next several paragraphs.

First, it must be noted that forcing higher than equilibrium solubilities in alloys such as described here is strictly temporary. In traditional precipitation strengthening alloys there is generally a temperature that the alloy can be held at to fully dissolve the precipitates and revert the microstructure back to a single phase solid. This is very useful in application cases where a part has been overheated, causing the precipitates to coarsen and lose strengthening effectiveness. In the case where rapid solidification is used to create artificially high solubilities, there is no way to fully undo the precipitation and start over if the microstructure becomes unfavorable, as the solute concentration is higher than

the equilibrium solvus value at the eutectic temperature. This inability to fully solutionize necessitates a higher level of care to ensure that overaging temperatures and localized melting are avoided throughout the processing and use of such alloys. Thankfully, the thermally stable nature of Al_3Sc and Al_3Zr precipitates when compared to other aluminum precipitation systems (Al-Cu, Al-Mg-Si) [3,7,16,18,29], makes them ideal candidates for use under such limitations as they overage at higher temperatures.

Secondly, the achievable supersaturation levels in these alloys are dependent on solidification rate. Literature suggests guidelines for the rates that are necessary for certain supersaturation levels in Al-Sc alloys [3], but as accurately measuring solidification rate becomes more challenging with increasing solidification rate, it is beneficial to determine the achievable supersaturation levels experimentally for any rapid solidification setup that is intended to be used in this manner (as described in Ch 4.2.1). There are several rapid solidification methods which can achieve solidification rates up to 10^5-10^7 °C/s, such as the melt spinning described in Ch. 3.1, 4, and 5, but these methods invariably achieve such a rapid solidification by solidifying the liquid with a very thin section size. In terms of the industrial application, this material (ribbon, powder, etc) must be consolidated in some way without causing the supersaturation levels to fully deplete in order to prove useful.

It must also be noted that rapid solidification causes micro-scale and even nano-scale grain sizes, which can negatively affect creep resistance in these alloys, as deformation mechanisms at high homologous temperatures in aluminum alloys utilize grain boundary

sliding. Because of the retarding affect Sc and especially Zr have on recrystallization [30,31], combined with the previously discussed inability to post-process solutionize, it is exceedingly difficult to increase the grain size.

2.4 Consolidation of Rapidly Solidified Materials

The beneficial cooling rate of rapid solidification allow for the creation of unique materials with desirable properties, such as the supersaturated Al-Sc ribbon discussed in this work. Unfortunately, rapid solidification is only achievable with exceedingly small section sizes to allow for sufficient thermal flow, which means that the end product is limited to thin ribbons or powders.

The treatment of aluminum powders with a goal to create a bulk material has been thoroughly covered in literature, with the typical procedure involving sintering at elevated temperatures to break up the aluminum oxide layers surrounding each particle. However, the research discussed in this manuscript deviated from that in the literature by aiming to retain any supersaturation in solution in the rapidly solidified material, making it necessary to avoid a sintering step. This necessitated the development of the two step process described in later chapters, wherein room temperature compaction into a loose billet was performed and the loose billet was then used as a consumable tool for friction stir processing.

Chapter 3: Experimental Techniques

3.1 Rapid Solidification

Rapid solidification was used in the experiments described in Chapters 4 and 5 to increase the supersaturation of Sc and Zr in the FCC Al phase. There are many methods of rapid solidification, all of which result in the production of material with very thin cross sections. In this work, all rapid solidification was performed in a custom melt spinner constructed at Michigan Technological University. Melt spinning is a process where a metal charge is melted and then sprayed in a fine stream onto a spinning chilled wheel. The stream of molten metal flattens on the wheel before solidifying, and is then thrown off of the wheel as a continuous ribbon. The melt spinner used for this research consists of an induction coil positioned over a large copper wheel in a vacuum chamber.

3.1.1 Melt Spinning Crucibles

The melt spinner was designed to accept both quartz and graphite crucibles, although the experiments described in this work used quartz exclusively, as shown in Figure 3.1. Quartz crucibles were chosen mainly due to the relative ease of monitoring the melt operation when compared to graphite crucibles. Unlike the graphite crucibles, the geometry of the quartz crucibles allowed for a topper assembly with a borosilicate

viewport, enabling accurate assessment of melt temperatures with a ratio pyrometer. Geometric considerations aside, graphite gives off a considerable amount of black body radiation which can skew pyrometer measurements. The transparency of the quartz crucibles also allowed for visual monitoring of the melt, which was useful as a second check to ensure the pyrometer was properly aligned and reporting believable temperatures. One significant downside to the use of quartz for high temperature Al melting is that aluminum oxide (Al_2O_3) is more stable than quartz (SiO_2) (Fig. 3.2b). If left unchecked, this stability discrepancy drives the chemical reaction $4Al + 3SiO_2 \rightarrow 2Al_2O_3 + 3Si$, resulting in an Al alloy with an unintentionally high Si content. However, this effect can be minimized with the use of an aerosolized yttria coating, as yttria is more stable than both quartz and alumina, as seen in the Ellingham diagram in Figure 3.2.

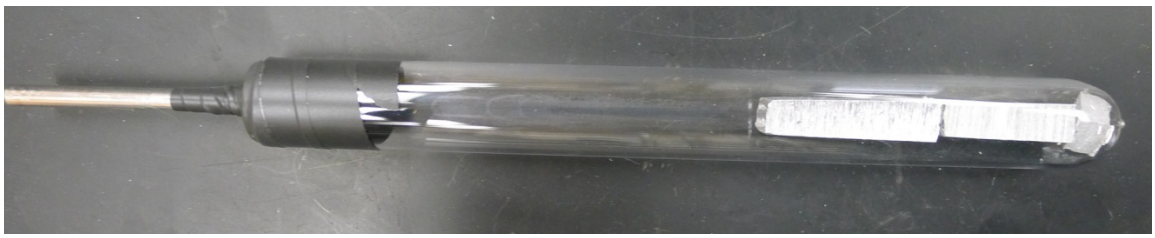

Figure 3.1: This image shows a quartz crucible intended for melt spinning. Inside, a charge made up of weighed pieces of master alloy is visible, and a simple rubber plug acting to cap the crucible is shown sealing the left end of the crucible with electrical tape. In this configuration, an argon source is attached through the plug, leaving the orifice on the opposite side of the crucible as the only unimpeded opening.

These crucibles are created individually in a glass lathe by using a hydrogen torch to neck down the middle of a 25 mm OD quartz tube. The necked down section is then cut with a diamond saw, and each half of the tube is fashioned into a crucible. In order to properly shape and size the orifice, the orifice was further necked down around an inserted piece of 0.7 mm mechanical pencil graphite. The graphite is uniquely suited as an orifice guide due to the benefits of being thermal shock resistant, self lubricating, and consistent in sizing.

After the crucibles were cooled to room temperature, an aerosolized yttria coating (ZYP Coatings) was sprayed into the interior of each crucible until the yttria solution formed a puddle near the orifice end. The crucibles were then spun slowly by hand until the solution was dried, taking care to ensure an even covering of the crucible surface. To ensure that the orifice was clear of yttria, pressurized air was blown through the orifice from the exterior, commonly resulting in sudden removal of blockage. Finally, before the yttria coated crucibles could be used, it was important to burn out any residual organics from the aerosol yttria. This burning out was accomplished by placing the crucibles in a high temperature furnace at 1273K (1000˚C) for 20 minutes.

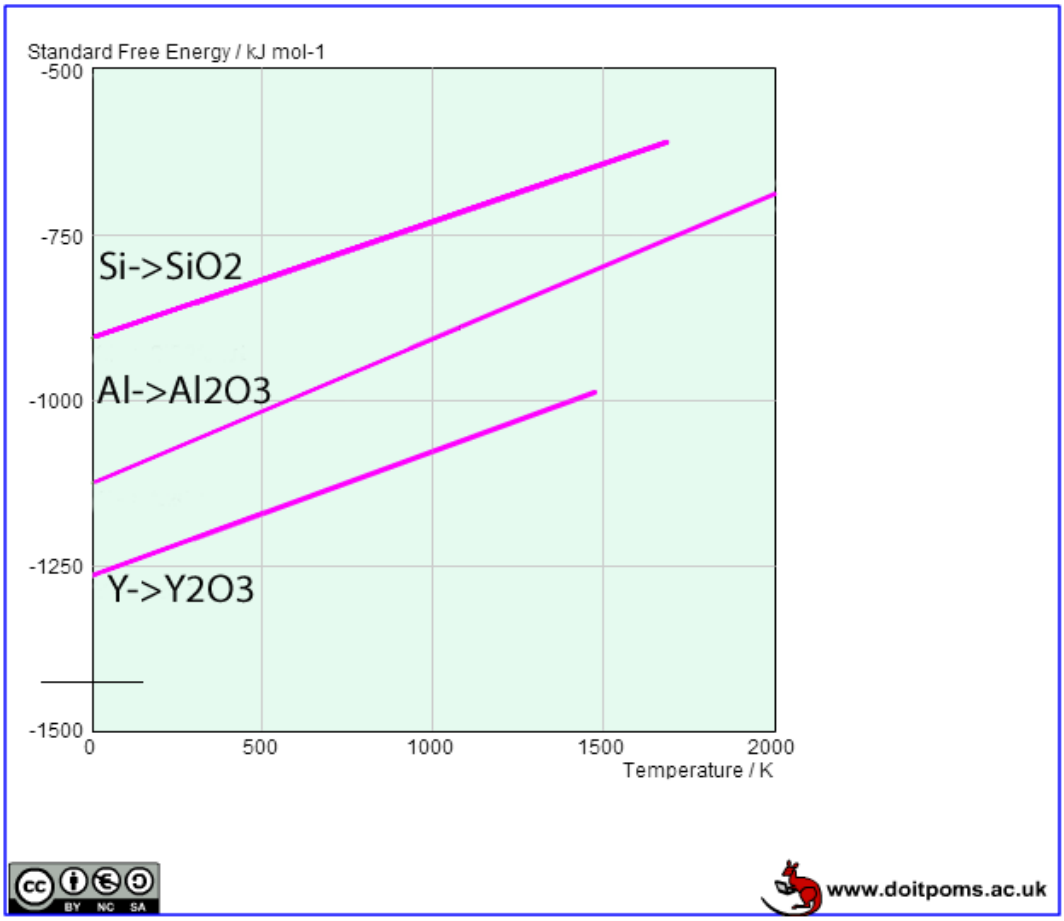

Figure 3.2: This image represents Ellingham diagrams showing the stability of Al_2O_3 vs SiO_2 vs Y_2O_3, and was generated on the University of Cambridge online resource (http://www.doitpoms.ac.uk/tlplib/ellingham_diagrams)

3.1.2 Setting up the Melt Spinner

Pieces of master alloys were weighed and combined in the correct ratios to create the targeted alloys as described in Section 3.13, and the resulting charges were placed into the prepared quartz crucibles individually. The crucibles were then inserted into the induction coil of the melt spinner from above. Prior to this, the induction coil had been

insulated with aerosolized yttria coating and electrical tape to limit the chance of electrical arcing from the coil to the wheel through liquid metal splatter during ribbon formation.

At this point, although the charge could be melted in the crucible, it would flow out of the orifice at the bottom before any significant superheat and hold was achieved. To control the flow through the orifice, the stainless steel topper assembly loosely mounted in the chamber was used to cap the crucible. This topper, while not blocking the orifice in any way, blocks all other gas exchange between the interior and exterior of the crucible, which in turn creates a situation where surface tension and minor differences in gas pressure keep the liquid metal from flowing through the orifice (similar to holding liquid in a straw by capping the top with your thumb). This topper assembly features o-rings to ensure an airtight fit with the crucible, a hose attachment leading to an argon tank to allow for adjustment of internal gas pressures, an upward facing borosilicate viewport for pyrometer measurements, and a clamp attachment point to ensure that the topper doesn't fly off of the crucible when the internal pressure exceeds the pressure in the rest of the chamber. A second clamp, lined with a woven fiberglass fabric, was used to gently hold the crucible in position to stop the crucible from pushing out of the topper downward in such an overpressure situation. Once affixed to the crucible/topper assembly, the vertical positioning of the clamps was adjusted and fixed with the adjustment of nuts on a threaded guiding rod. In this way, the crucible orifice was positioned to be just under the bottom of the induction coil, approximately 1 cm away from the copper-beryllium wheel.

At this point, the targeting mode of the pyrometer (a Micro-Epsilon ratio pyrometer with 0.5% accuracy, 5 ms response time) was activated. In this mode, a visible red light is shone through the pyrometer, which is fixed to an adjustable bracket looking through the top borosilicate viewport of the chamber. This red light served to highlight the view path of the pyrometer and allow for slight changes to be made to the pyrometer and crucible alignment for proper measurement of the charge throughout the entire melting process. Once the alignment was satisfactory, the pyrometer was switched back to measurement mode and the chamber door was shut.

3.1.3 Melt Spinner Operation

Using a mechanical rough pump, the internal pressure of the chamber was reduced to ~0.1 Torr. At this point the diffusion pump was activated, eventually decreasing the pressure to $8x10^{-5}$ Torr. It is important to note that at this time, the pressure in the chamber is identical to the pressure in the crucible, as there is no liquid in the crucible to create a barrier. The next stage was to backfill the chamber with 99.999% purity argon, although there are considerations that must be taken into account in regards to the exact procedure. During the melting operation, it is preferable to have a slightly lower pressure within the crucible than in the chamber, as this pressure differential helps to hold the liquid metal in. This can be accomplished by melting the charge while argon is being backfilled, which requires specific timing. Generally the order of operations was:

1) Start the copper wheel spinning at 1500 rpm
2) Start the induction coil heating the sample
3) Immediately start backfilling the chamber with argon
4) When pyrometer display reads over 973K (700˚C), turn off chamber argon flow
5) As the pyrometer approaches 1373K (1100˚C), quickly reduce induction power
6) Maintain temperature at 1373K (1100˚C) for 1 minute by adjusting power
7) Turn off induction power and immediately open the crucible's argon line
8) Ribbon should form and be sent into the catch

After complete ribbon formation, the ribbon was allowed to cool for approximately 10 minutes before the chamber was backfilled with air and the ribbon was removed. Ribbon was generally several meters long with cross sectional dimensions of ~50 μm x 3000 μm.

It is important to make visual checks of the crucible throughout the melting process. If the pyrometer is not accurately reading the temperature of the melt, the melt can reach a much higher temperature than intended. With experience, this can be easily noticed as the intensity of black body radiation will be noticeably higher, as shown Figure 3.3. If at any time noticeable deviations from intended operation are observed through the viewport, power to the induction coil should be cut immediately. To protect the copper wheel, it should never be turned off while the charge material is still a liquid.

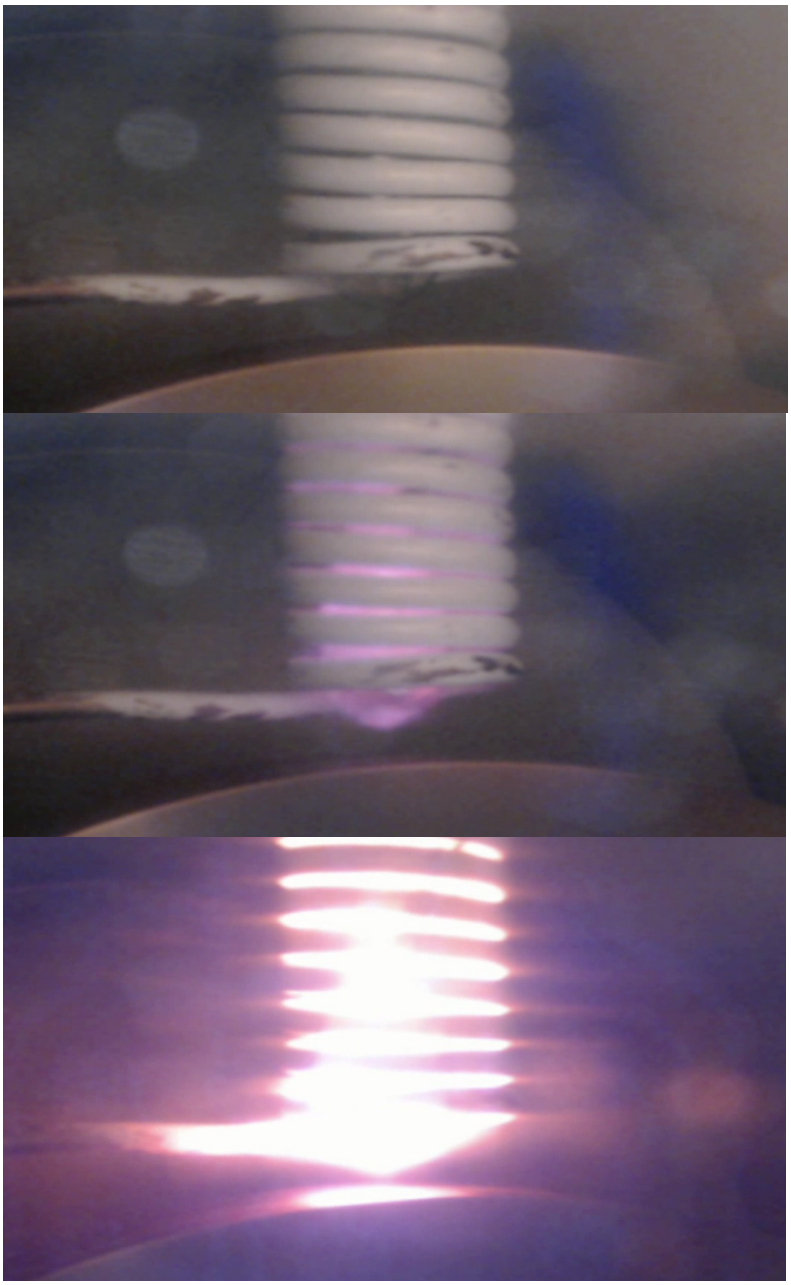

Figure 3.3: This series of images shows the progression of black body radiation as the sample is heated. In these images, temperature is estimated as below 700˚C, around 900˚C, and around 1100˚C, respectively, although the intensity of this appearance will vary in practice due to aerosolized coatings of the crucibles, brightness correction in the camera used, etc.

3.2 Consolidation of Ribbon

In these experiments, avoidance of re-melting the supersaturated melt spun ribbon was critical to eliminate the possibility of primary Al_3Sc and Al_3Zr precipitation. In fact, it is ideal to eliminate any unnecessary increases in temperature, in order to maintain the supersaturated state and limit nucleation and growth of these precipitates. To this end, all processes for consolidation of the melt spun ribbon into feedstock material for AFS was performed at a room temperature of 298K (25˚C).

The initial step in ribbon consolidation is to mill the ribbon into fine flakes through the use of a SPEX 8000-D ball mill. The 65 mL stainless steel vials that were used for this operation, shown in Figure 3.4, could accommodate approximately 5 g of ribbon at a time. Four 0.635 cm diameter stainless steel balls were inserted into the vial with the ribbon to facilitate the milling, and 0.1 g of stearic acid was added to limit agglomeration of the ribbon. All vials were opened and the contents rearranged after approximately 30-45 seconds, when the telltale sound of the steel balls bouncing from cap to cap in the vial began. At this point a straight path had usually formed through a mass of as yet unbroken ribbon, allowing the steel balls to bounce between caps without doing any appreciable work. Rotating the ribbon mass 90˚ invariably resulted in the breaking up of the remainder of the ribbon before an accumulated time of only 1.5 minutes, whereas before employing the method of rotating the ribbon, it was rare to see the ribbon entirely reduced to flakes before 5 minutes of milling.

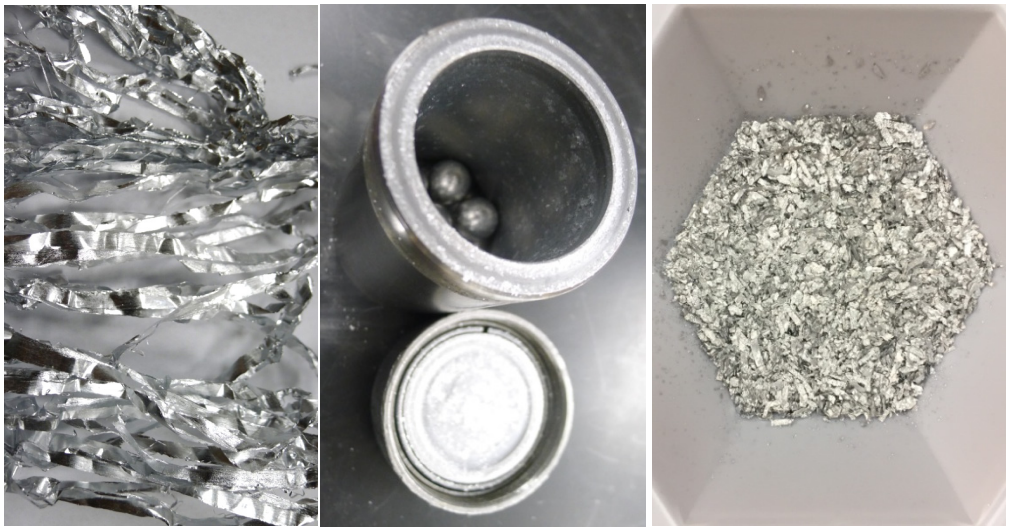

Figure 3.4: Melt spun ribbon was briefly ground in a stainless steel SPEX mill vial, shown above, containing four 0.635 cm diameter stainless steel balls. After approximately 1.5 minutes, the ribbon was reduced to a flakey powder.

Through trial and error with X-ray diffraction lattice parameter analysis (Ch 3.6), it was observed that the lattice parameter was reduced by a consistent amount over the course of milling (Figure 3.5). Initially this was believed to be caused by a reduction in solute concentration due to the formation of precipitate phase, but that theory was ruled out when the effect was found to exist in pure Al melt spun ribbon as well. It is believed that this effect is due to the reduction of lattice strain caused by rapid solidification. Because of this effect, ribbon was always milled for at least 1 minute to ensure comparisons between lattice parameters would have significance.

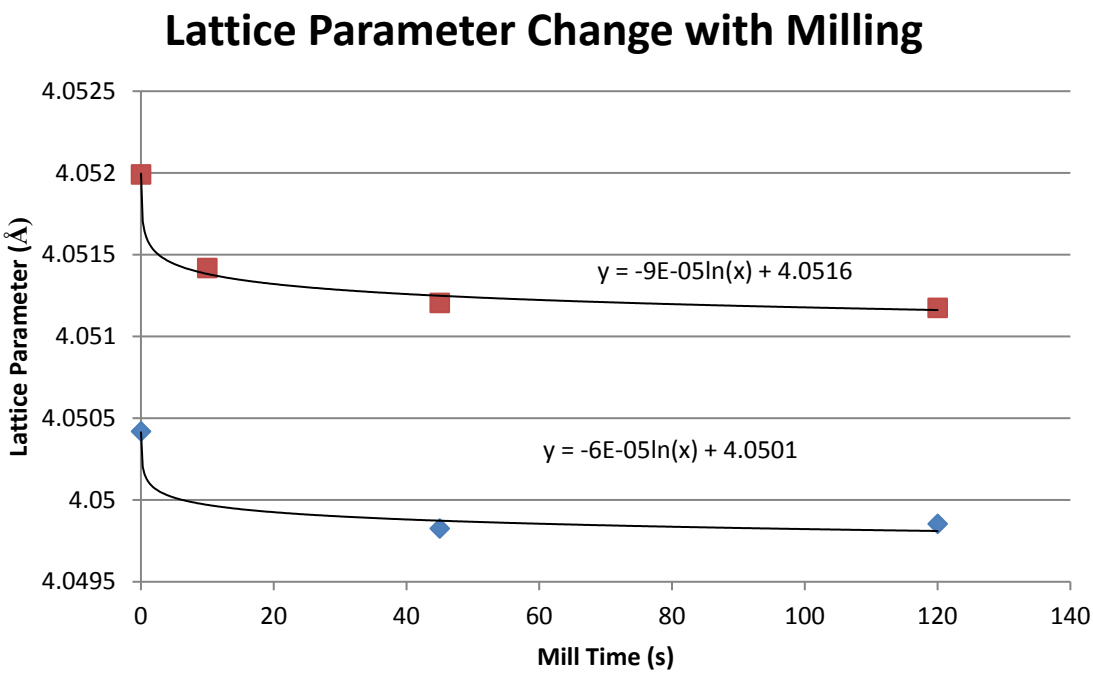

Figure 3.5: This graph demonstrates the lattice parameter change, as determined by XRD, of melt spun ribbon after milling for different times in a SPEX mill. The blue ribbon points represent pure Al ribbon, while the red represents Al-0.2at%Sc-0.2at%Zr ribbon. A similar initial drop was seen in all alloys tested.

3.3 Additive Friction Stir Processing

Additive Friction Stir processing (AFS) is a method for mechanically combining two solid materials without any localized melting. It is a derivative of the more traditional friction stir welding, where a tool is used to join two workpieces together by applying axial pressure and rotation as the tool moves along the adjacent edges of the workpieces in question, blending them together. The main notable differences between friction stir

welding and AFS are that (A) the tool that is used is a consumable comprising of one of the alloys that is to be combined, and (B) this is method is typically applied to the surface of a single workpiece to create an affected surface layer instead of along a gap to join two pieces together.

In this work, all AFS was performed off-site by our partners, Aeroprobe Inc. Melt spun ribbons with varying levels of enhanced Al-Sc and Al-Zr supersaturation were fabricated and cold compacted into suitable 0.9525 cm wide feedtock pellets at Michigan Technological University and shipped to Aeroprobe for processing. There they were stirred into 99.99% pure aluminum 0.635 cm plates and then sent back to Michigan Tech for analysis. Images of the feedstock pellets and processing specifics are omitted from this work at Aeroprobe's request.

3.4 Heat Treating

Heat treating was performed on all samples in either box furnaces or a vacuum furnace. The capabilities and procedures for each furnace are described in the following sections.

3.4.1 Box Furnaces

Box furnaces with no cover gas were used most frequently for heat treating operations in this work. A representative of the box furnaces used is shown in Figure 3.6. Before samples were inserted into a box furnace, a type K thermocouple was inserted into the furnace so that the juncture rested exactly where the samples would sit. The furnace was

then heated up until the inserted thermocouple stabilized at the target temperature. The PID controllers on these furnaces read temperature from internal thermocouples mounted in the top of each furnace, and therefore must be set at higher temperatures than the target temperature in order to compensate for thermal gradients in the box. Once the temperature was acceptable, the box would be opened and the sample would be quickly placed in the location of the thermocouple, touching the junction. In order to allow the temperature to stabilize, 15 minutes were allowed for the sample in the furnace before the time was started for the prescribed heat treatment. After the allotted time was complete, the sample was removed and quenched immediately in room temperature water.

Figure 3.6: This image shows one of the box furnaces used for this experimentation. Every furnace had some amount of temperature discrepancy, so external thermocouple readers were used to monitor the temperature at each sample.

All heat treatments were run with limited numbers of samples in order to keep the samples clustered tightly in the middle of the furnace next to the thermocouple. Because of the nature of box furnaces, nearing the refractory walls on either side would increase the temperature and potentially give misleading heat treatment information.

3.4.2 Vacuum Furnace

A Vacuum Industries, Inc vacuum furnace, shown in Figure 3.7, was used to heat treat samples that were more sensitive to oxidation. Whereas bulk samples could be heat treated in air and then polished quickly to remove the increased thickness of the alumina layer, heat treating ribbons and cold compacted ribbon pellets did not offer these flexibilities. With the ribbon only being 20 microns in places, it was deemed unacceptable for the hardness testing, for the X-ray diffraction characterization (XRD), and for the eventual integration into AFS substrate that the ribbon be heat treated in air.

The vacuum furnace can only be opened at temperatures below approximately 373K (100°C), so it necessitates placing samples inside before the temperature is ramped up. The ribbon samples were balled up and placed on a steel tray inside the chamber that could be taken out of the furnace between trials for consistency and ease of positioning. Before increasing the heat, the chamber was vacated to a vacuum level of approximately $1x10^{-5}$ Torr. At this point, the vacuum was ramped up to the desired temperature over the course of 15-20 minutes and held for the allotted time. At the end of the required time, the chamber was flooded with industrial purity argon to a level of ~500 Torr to allow for

faster cooling. The samples cooled down to a temperature below 373K (100°C) over the course of ~30 minutes and were then removed.

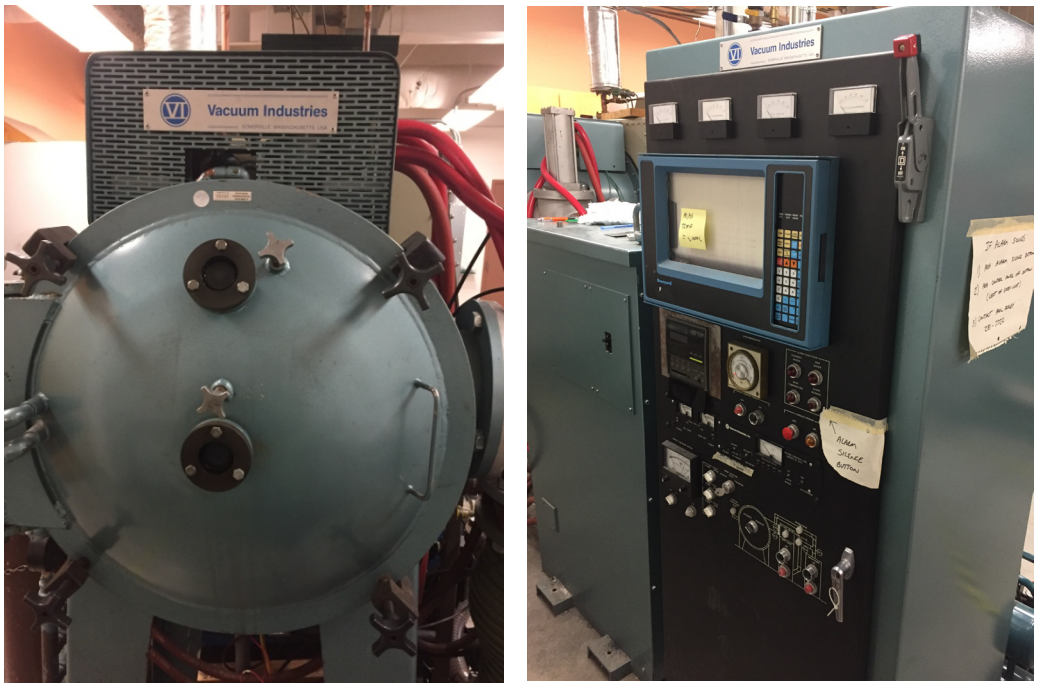

Figure 3.7: These images show the vacuum furnace used for the heat treatment of melt spun ribbon. The left image shows the actual vacuum chamber, which contains resistance heating elements, and the image on the right shows the control panel for the furnace's operation.

3.5 Inductively Coupled Plasma - Optical Emission Spectroscopy

To verify that alloys used in these experiments were within acceptable compositional ranges, Inductively Coupled Plasma Optical Emission Spectroscopy (ICP-OES) was performed. To prepare samples for ICP, they must be fully dissolved in acid, so it was necessary to cut bulk samples into thin wafers (~0.5 mm thick) using a Japax LUX3 Wire-cut EDM (Electrical Discharge Machining) to increase the surface area available for dissolution. Melt spun ribbons are already thin enough for easy dissolution, so EDM was not used for samples discussed in Ch. 4 and 5. It is also important to note that Cu concentration will likely be artificially high in samples that were cut in the EDM because of discharge from the 0.0254 mm diameter Berocut brass wire used, so in trials where Cu content was investigated, an alternate method of drilling holes in the sample and collecting chips was employed to create easily dissolvable pieces.

For each sample, a maximum of 0.4 g (actual values calculated based on alloy concentrations) of thin material was microwave digested in 6 mL of 70% HCl and 2 mL of 37% HNO_3, using an Anton Paar microwave digestion setup. Following this digestion, the fully dissolved samples in acid solution were poured from the Teflon digestion tubes into hydrophobic 100 mL volumetric flasks. To catch any acid solution that remained in the tube, distilled water was sprayed on the walls, swished around, and poured into the flask twice. The total solution volume in the flask was then brought up to 100 mL using

more distilled water. At this point, the samples were emptied into hydrophobic 125 mL nalgene bottles for storage until the actual ICP analysis could be performed.

An optical emission spectrometer (Perkin Elmer Optima 7000DV ICP-OES) was then used with standards (Inorganic Ventures) to determine the concentrations of the elements of interest (Sc, Zr, Si, Fe, and/or Cu) in each solution. ICP works essentially by nebulizing a liquid sample (the acid solution) and introducing it to an argon plasma. Upon contact with the plasma, particles in the nebulized solution are quickly dried, atomized, excited and relaxed. Different wavelengths of light are emitted from each atom present, and the amount of light representing each alloy is proportional to the quantity of such atoms in the solution. These wavelengths are detected and quantified by a CCD detector, and the intensities of the peaks are calibrated in the software against standards with similar concentrations of elements.

3.6 XRD Analysis of Solute Concentration

For each melt-spun alloy, 2 g of ribbon was milled in a SpexTM ball mill for 1 minute and subsequently compacted at 70 MPa and room temperature into a 25 mm diameter puck (see Section 3.2 for more details). In preparation for analysis in an XDS2000 powder x-ray diffractometer, this puck was placed on a piece of moldable clay and then pressed and held in a level orientation by a weighted glass slide for 1 hour. The diffractometer was used to collect the (111), (220), (331), and (420) peaks of the Al matrix, and lattice parameters were calculated for each peak. While each peak on a given

scan describes the same lattice parameter, sample displacement can introduce systematic errors that diminish as the angle of diffraction, 2Θ, approaches 180˚. At such an angle, the displacement error is considered insignificant and the corresponding lattice parameter value considered true. Plotting the calculated values of each peak in a given scan against a function of 2Θ known as the Nelson-Riley function results in a straight line with an extrapolated y-intercept corresponding to the true lattice parameter value [32].

While knowledge of the lattice parameter at a given time doesn't give any indication of the solute concentration levels in the sample by itself, the lattice parameter of a matrix phase does change linearly with the addition of solute atoms. By observing several different alloys with identical processing conditions but differing concentrations, it is possible to create a reliable correlation relationship. Experimental observations of higher concentration alloys will also likely show that the correlation described above does have a limit, after which the lattice parameter of the matrix remains steady even with the addition of more solute atoms. This is due to the fact that precipitation occurs in equilibrium conditions if concentrations of the solute atom increase above the solubility limit.

3.7 Vicker's Hardness Testing

Hardness testing in general is a technique where a diamond indenter is pressed into the surface of a material with a known load. After the load is removed, the size of the indentation is recorded and a hardness value is determined by the calculated displaced

volume. Specifically, Vicker's hardness testing, which uses a four sided pyramidal indenter, was performed throughout the works described in this dissertation. Vickers hardness testing, when recorded in units of MPa, can be estimated as approximately one third of the yield strength for that material, allowing monitoring of strength without the need to create and test dozens of tensile test samples. The two hardness machines used throughout the course of this testing are shown in Figure 3.8.

Figure 3.8: These images show the two makes of hardness tester used for the experimental work described in this paper. Shown on the left is a LECO MHT Series 200 unit, which has an automatic XY stage for analysis of grids. Shown on the right is a LECO M-400-G1, used for randomly distributed testing.

Hardness tests were performed automatically in a grid, with loads of 10-50g and a hold time of 15s. Indentation marks were measured by an operator using the hardness testing software with either a 20x or 50x objective lens (chosen on a per sample basis depending on the sizes of indentation marks). Samples discussed in this work that were subjected to hardness testing were polished down in preparation to either a 1 micron diamond or a 0.04 micron colloidal silica finish, depending on the set of experimentation. Due to the small indenting loads used, a fine polish is important to limit variability in the results. It was not necessary to ensure both faces of the sample were level while preparing each sample, as the sample holder was self leveling for the intended test surface.

3.8 Electrical Conductivity Testing

Electrical conductivity was tested in samples with a Fischer Technologies Sigmascope SMP10, shown in Figure 3.9. To ensure an accurate and consistent reading, samples were required to be relatively flat and to have sufficient surface area to fully accommodate the end of the probe. However, the surface did not require polishing, as the probe read at an offset of 0.5 mm into the sample. At the time of each measurement, the temperature of the sample was determined with the integrated thermocouple by holding the probe on the sample for 30 seconds or until readings stabilized. Once accurately determined, the sample temperature was input into the tester settings and used to correct the conductivity measurement readings. At this point, measurements were performed rapidly in different locations across the sample.

Figure 3.9: This image shows the electrical conductivity meter used for the experiments described in this work. By placing the probe (black cable to the right) on the surface of a sample, the observed conductivity is displayed on screen and can also be recorded on a computer through an RS232 or USB port.

3.9 Scanning Electron Microscopy Analysis

3.9.1 Sample Preparation

The preparation procedure for SEM samples varied depending on the original morphology, and the specific procedures are described in Section 3.12. Regardless of morphology, the samples were completely encased in epoxy, ground and polished to achieve a final polish using 0.04 micron colloidal silica.

The mounted samples were then carbon coated to ensure a conductive surface and to mitigate the buildup of charge on the surface during SEM operation. Immediately before SEM analysis, a sample was removed from its cover and inserted into an SEM sample holder. Generally a two-sample holder was used to allow for more efficient analysis of multiple materials, or to allow the use of pre-prepared standards for WDS analysis. Double sided carbon tape was laid down from unimportant areas on the carbon coated sample surfaces to convenient areas on the sample holder, creating paths to ground. Placement of the tape required delicacy, as the sample surface immediately adjacent to the tape would be unobservable in the SEM due to electrical charging of the frayed tape edges.

3.9.2 Backscatter Electron Imaging

Backscatter Electron Imaging (BEI) is a method of Scanning Electron Microscopy (SEM) where only high energy electrons that have been reflected out of the sample through elastic scattering interactions with atoms in the sample. These electrons originated with the electron beam source (LaB_6 or tungsten filament), as opposed to secondary electrons which originated in the electron orbitals of atoms in the sample before being dislodged by the beam.

While secondary electrons give information concerning the topographical surface features of a sample, backscattered electrons can be used to determine relative average atomic number values for regions in the sample. Elements with higher atomic numbers

will backscatter more electrons than elements with smaller atomic numbers. This can be useful as an analysis tool. For instance, in Chapter 5 BEI is used to observe variations in Zr content across an AFS weld. EDS mapping had been previously attempted for this operation, but the Zr concentration proved too low to be detectable.

In this research, BEI was performed on a JEOL JSM-6400 SEM. A working distance of 39 mm was used and the coarse condenser lens (CL) was set to 4, and the aperture was set to 1. Because of the low concentrations of Zr in the samples observed in Chapter 5, the amount of white noise in the live image screen obscured all semblance of contrast, even after fully optimizing the contrast settings. The contrast patterns discussed and shown in Chapter 5 became apparent only with the long raster performed to capture the image.

3.9.3 Wavelength Dispersive Spectrometry

Wavelength Dispersive Spectrometry (WDS) work for this research was performed in the JEOL JSM-6400 SEM. Sample preparation for use with WDS is the same as in standard SEM (Section 3.9.1), but it becomes necessary to include in the sample holder a second mounted sample containing several material standards. For this research, Al-Sc and Al-Zr master alloys were used as the standards for Al, Sc, and Zr respectively, as the large primary Al_3X precipitates that they contain are stoichiometric.

When using the WDS, the consistency of beam conditions is very important in order to achieve meaningful comparisons between analyses. Unlike in EDS, where the testing

location can be found with the SEM beam image before zooming in and analyzing the concentration at a point within the image, it is necessary to use an optical microscope to position the beam between points. To this end, a section of a material called Willimite is placed in the sample containing the samples. Willimite gives off light when impacted with the beam, so the location of the beam within the viewing area of the optical microscope can be found and marked with a wax pencil.

In order to calibrate the Sc and Zr detectors at the beginning of each WDS session, the beam was then maneuvered to one of the Al_3X precipitates (lining the mark that was made with the wax pencil up). The peaks were measured repeatedly until at least 3 consistently similar values were found. Once the peaks were found for each element of question and the correction values changed in the program to reflect them, points on the actual sample could be measured. Because each point analysis takes >5mins when using WDS, it was beneficial that the program can be set up to run multiple scans along a line/grid/etc.

3.10 Transmission Electron Microscopy Analysis

3.10.1 TEM Sample Preparation

TEM sample prep involves making sections of samples which have nanoscale thickness. This is generally done using one of three methods: nanoscale milling with a Focused Ion Beam (FIB) or equivalent equipment, creating holes in thin samples using electropolishing, or microtoming epoxy containing a dispersion of fine powder created

from the samples. In these studies, only the latter two were utilized, and both methods were found to yield TEM images of similar quality. Compared to the uniform thicknesses achieved with milling, both of the methods used require a large amount of TEM time searching for areas with proper thickness, whether at the edges of holes created by electropolishing or at the edges of powder particles that were partly removed during the microtoming process. However, milling TEM samples is prohibitively more expensive than the other two methods, as the process requires more expensive equipment and it takes at minimum several hours to make each sample. All things considered, electropolishing samples was the preferred method in this research because of the ease of sample preparation for a variety of sample geometries and the ability to specify a single location on a sample for analysis.

All TEM samples that were prepared using microtoming in this work were created from melt spun ribbon material and discussed in Chapters 4 and 5. As discussed in those chapters and in Section 3.2, the ribbon was ground into a powder using a Spex mill with 0.635 cm diameter steel balls for 1 minute. The majority of the resulting powder consisted of particles that were too large to be used for TEM sample prep (~1 mm diameter), but these larger particles were always accompanied by a finer dispersion of powders in the bottom of the vial. After milling, all particles were transfered into white plastic hexagonal weighing dishes before being compacted into discs for XRD or feedstock material for AFS. The finest particles remained in the dishes after pouring due to static cling and were gently consolidated in a corner of the dish using a methanol spray bottle. This fine powder was then encased in a hard epoxy by ACMAL staff. When thin

slices of the epoxy/powder composite were removed with microtoming, it was statistically probable that some of the powder particles were cut thin enough to transmit electrons through. These thin slices were then stored in a TEM grid storage box, shown in Figure 3.10.

Figure 3.10: All TEM samples were stored within a TEM grid storage box, as shown. Locations of different alloys/processing parameters can be documented using the letter/number grid coordinate labels adjacent to the grid.

Sample preparation using electropolishing required similar amounts of preparation in ribbon when compared to microtoming, but required considerably less work when creating TEM samples from bulk material (as in Chapters 6 and 7). The basic procedure

followed to prepare samples for electropolishing operations on the bulk samples described in this work are as follow, while the procedure for melt spun ribbons is similar but omits the first 6 steps:

1. Cut a 0.5-0.8 mm thick slice from the sample using EDM
2. Superglue the slice to a 3.175 cm diameter Bakelite blank
3. Polish the exposed face of the sample to at least a 1 micron diamond finish (similar to Section 3.12, with care not to polish through slice)
4. Remove sample from Bakelite with a razor, flip, and re-glue
5. Continue polishing sample until one of the edges begins to disappear
6. Remove sample with a razor and wash glue off with an acetone bath
7. Punch 3 mm dia. discs out of the sample with a specialized hole punch
8. Reduce the thickness of the discs to approximately 50 microns using a Gatan Disc Grinder system and 1 micron diamond and/or 0.04 micron colloidal silica polishing methods
9. Store the finished TEM samples in a well marked grid storage box

Once several sufficiently thin 3 mm discs for each sample were prepared, electropolishing was performed on each disc individually using a Metalthin instrument with a solution consisting of 29% reagent grade nitric acid and 71% reagent grade methanol. The solution was kept below 243K (-30˚C) with a Multicool recirculating methanol refrigeration unit. The relevant operating settings for the Metalthin instrument were: 20-30 volts, jet speed of 4, sensitivity of 7-8.

3.10.2 TEM Operation

All TEM analysis was performed on a JEOL JEM-2010 high resolution transmission electron microscope. All images were captured with a Gatan Orius SC200 high-speed digital camera, and all chemical analysis of nanoscale features was performed using an Oxford energy dispersive spectrometer (EDS).

3.11 Cutting Samples

Throughout this research there were several situations where samples required cutting, such as to allow for proper melt charges or to section samples for analysis. The methods described in this section were used for various reasons/circumstances and have unique benefits and problems.

3.11.1 Wire EDM

Wire EDM (electrical discharge machining) is a method of cutting samples through spark erosion. The following description concerns the operation of a JAPAX LUX3 EDM, shown in Figure 3.11, the machine that was exclusively used for EDM work in this research. A conductive sample is secured to a motorized stage in such a way that it is grounded, and a spool of Bedra Bercocut bronze wire is continuously unwound past the edge of the sample and rewound on the other side. Distilled water, maintained at proper conductivity by a JAPAX #PW20X Wire EDM Filtration Unit, is sprayed around the wire and onto the sample, providing conductive pathways to spark to the sample while simultaneously cooling the sample. At this point, an electrical current is set up across the

wire, and sparks will jump to the sample if it is close enough. While the stage can be controlled manually to slowly cut the sample, generally a program is set up using G-code to describe the cutting path, speed, etc of the wire.

Figure 3.11: Electrical Discharge Machining was performed using a JAPAX LUX3 EDM, as shown in this image. The right portion of this machine (from this viewpoint) contains the control panels at top and the wire spooling/unspooling behind dark plastic guards. The left portion contains the cutting portion of the wire along with a guarded XY table. Moving the XY table introduces samples to the wire, allowing for precision cutting.

Wire EDM is primarily used in this research to cut thin sections for TEM sample preparation, and to cut ICP-OES samples from alloys where the copper content is of no concern, such as the Al-Sc and Al-Zr alloys. Typical machine settings for the Al alloys used in this research are:

- T_{off} = 10
- T_{on} = 4
- Io = 3
- V = 4
- Vs = 4
- % = 100
- Feed = 10
- Tension = 6
- F varies with thickness (Sheeting = ~8)
- Basc II for uniform thickness, Basc I for nonuniform

3.11.2 Saws and Shears

Typically saws and/or shears were used when the integrity of the exact sample composition was important. Examples of this are in alloy charge preparation for melting operations and in the preparation of alloys for ICP-OES (Section 3.5). Alternate cutting methods, such as EDM and abrasive cut-off discs, have the potential to contaminate the sample being cut, especially in soft samples such as Al. With saws and shears there was still the chance for contamination from material that had been previously cut using the same tool, but this contamination was simple to remove with a post-process cleaning

procedure when compared to the embedded SiC grits that could result from cutting with the abrasive cut-off discs.

Typically for large scale cutting operations, as in the sectioning of master alloy ingots into more appropriate sizes for small charges, a horizontal bandsaw with sufficient coolant was used. The post-process cleaning procedure for this method was to remove all burs on sample edges with a cleaned metal rasp, soak the samples for at least 5 minutes in an ultrasonic acetone bath to remove the cutting fluid, wash all faces of each sample piece individually with soapy water and a cotton ball, rinse with running water, and then rinse with ethanol or methanol.

If small samples needed to be cut in half, etc, for the proper weights to be met during melt charge preparation, a handsaw was occasionally used. The blade of the handsaw was checked for cleanliness and washed with methanol before each use. During cutting, care was taken to keep the temperature of the sample low, either by limiting the speed of cutting, or by repeatedly quenching the sample in the sink.

For very fine adjustments of weight during melt charge measurement, a pair of end cutting nippers allowed for controlled removal of sufficiently small pieces to reach target weights satisfactorily. Typically corners would be cut off and saved, as they were the easiest section to remove and were often useful in later charges that were slightly underweight. This method was most effective with 4N purity Al, as it is very ductile, but with reasonably thin samples, all Al-based master alloys used could be adjusted this way.

3.11.3 Abrasive Cutoff Discs

The majority of sample surfaces that were polished in the course of this research (for SEM, optical microscopy, or hardness) were initially cut using an abrasive cut-off disc. The disc, typically an Allied High Tech Products 35.56 cm 80-10025 disc, was housed in a LECO CM-24 Cut Off Machine with integrated coolant recirculation. The large samples, firmly clamped in the machine, were slowly sectioned by the cut-off disc in a steady, pecking motion, ensuring the flowing coolant had sufficient opportunity to mitigate the generated heat. Any grits that may have become embedded in the soft Al samples was completely removed by subsequent grinding and polishing operations.

3.12 Grinding and Polishing Samples

All hardness, conductivity, and microstructural analysis (SEM, TEM, and optical) described in this research required prior grinding and polishing operations. Depending on the original condition of the sample and the final application, the steps involved varied. For instance, starting with an uneven surface required an initial low-grit grinding operation to create a flat surface, while starting with a freshly cut surface would not. If the final goal was analysis by SEM, the final polish required was finer (typically 0.04 micron colloidal silica) than if the final goal was hardness or conductivity testing. The current section attempts to describe all grinding and polishing procedures used in such a way that all scenarios within this research are made clear.

3.12.1 Mounting Samples

The majority of samples discussed in this research required some form of mounting in order to be hardness tested, with the exception being arc melted samples. Mounting samples was always necessary for any SEM and nanoindentation analysis. Depending on the intended processing and original form of the sample, different methods were used, as will be described in this section.

In samples that were prepared from standard melt spun ribbon, the ribbon was supported on its side using plastic spring mounting clips within a 3.175 cm diameter mounting cup. The use of plastic mounting clips as opposed to steel mounting clips is an important distinction; when steel clips were substituted, it was found that the steel slowed up polishing enough to allow chemical erosion of the Al ribbon, presumably due to PH discrepancies with the polishing media.

In such ribbon samples, and in samples which consisted of loose or compacted powder particles, it was important to ensure that any epoxy used would completely fill any voids between ribbons/particles and would not pull away from the samples once solidified. To achieve this, a vacuum was pulled around the samples and epoxy was allowed to bubble inside the vacuum until it stopped. Once the epoxy was calm, it was poured around the samples, resulting in a vacuum impregnated epoxy sample with minimal delamination between the ribbon and the epoxy.

In samples prepared from bulk materials, such as in the cross sections of AFS paths in Chapter 5 and in the Al-Cu-Zr alloys discussed in Chapter 7, samples were generally sectioned small enough to fit inside 3.175 cm diameter mounting cups using an abrasive cut-off saw (Section 3.11). If possible, each sample was marked with a Wen Power Tools electric engraver. If that was not feasible (ribbons, powder, etc), scotch tape with the necessary sample information written on it was affixed directly to the relevant mounting cup. Quickset epoxy (Acrylic Powder #185-10005 and Acrylic Liquid #185-10010) was then mixed thoroughly in a 2:1 powder to liquid ratio by volume and poured into the mounting cups, ensuring that the sample was entirely covered. After the epoxy solidified (typically ~5min), each sample was marked on the back of the epoxy with the electric engraver to allow for easy identification.

In cases where the samples were scheduled for multiple iterations of a heat treat → polish → test → repeat cycle, methods were developed to remove the necessity of re-mounting/grinding/polishing the sample between every heat treatment step. The first iteration of such a method involved the creation of a pure Al sample holder on the lathe. This sample holder, shown schematically in Figure 3.12, was the appropriate size for use in the SEM, hardness, and nanoindentation testers (3.175 cm), and held the sample in place with the use of a set screw. Because the sample holder was aluminum, it had the benefit over epoxy of being able to withstand the heat treatment temperatures, and it had the benefit over other material options (steel, etc) of polishing at approximately the same rate as the sample. A sample can be polished, tested, and heat treated without ever removing the sample, meaning that theoretically only minor polishing operations between

heat treatments would be required to remove the oxide layer. However, there were complications with this method that necessitated the development of an alternate method, namely: 1) polishing media was difficult to completely remove from between the sample and holder, causing pads to be contaminated, and 2) heat treating the at high homologous temperatures caused deformation in the holder due to the set screw, requiring periodic tightening of the screw and eventual replacement of the holder.

As an alternative to the aluminum sample holder, samples were set in epoxy as described earlier in this section and polished/tested. Before the next heat treatment step, samples were broken out of the epoxy by compressing the epoxy adjacent to the samples in a bench-mounted vice. The epoxy would break and the sample would be free. After heat treating, the still-polished sample would be placed face down on packaging tape and held down with a plastic rod. A mounting cup (without the bottom piece) was placed around the sample on the tape, and epoxy was poured around the sample. This method ensured that the polished surface of the sample would not be covered by a thin layer of epoxy and necessitate re-grinding/polishing. Once the epoxy was solidified, only minor polishing was required to restore the fine polish of the sample. Testing could then be conducted again, followed by breaking out and further heat treatments.

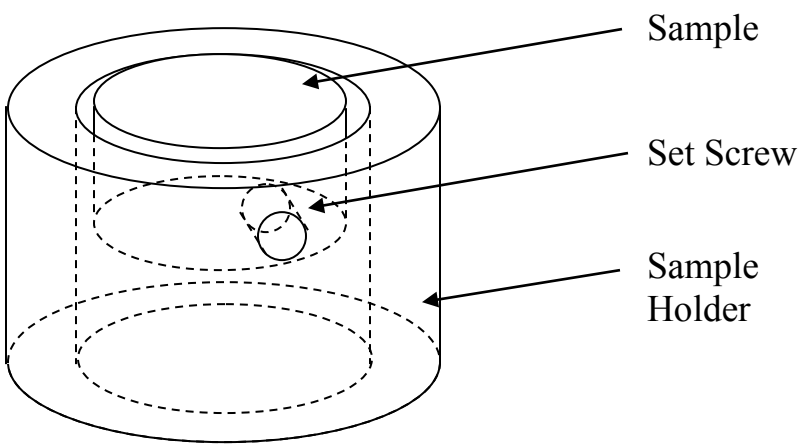

Figure 3.12: This schematic describes a consumable sample holder used in several of the analyses within this work. The ring itself is made of a similar material to the sample that is to be tested (in this case aluminum). A set screw is used to hold the sample in place through the whole polishing, analysis, and heat treatment cycle.

3.12.2 Grinding Operations

In samples with originally uneven surfaces, such as the rounded bottoms of arc melted samples, and in some epoxy mounted samples where the preferred plane of analysis was more than 1 mm below the epoxy surface, grinding operations were performed on a LECO GR-20 Coarse Grinder with 60 grit SiC and water cooling. Samples that were too thin to hold safely by hand were held with a pair of vice-grips.

In samples with relatively flat surfaces (including those ground flat as in the previous paragraph), hand grinding operations were performed to fully expose the sample and reduce the average thickness of abrasions, moving from 120 to 240 to 400 to 600 grit

SiC. At each step, the samples were held firmly and abraded in a single orientation (generally perpendicular to the direction of immediately prior grinding) until no scratches remained visible from previous operations. The sample was then rotated 90 degrees before repeating this process with the same grit to ensure that no deeper scratches were being hidden due to a shared orientation. Between each grinding step, the samples were simply rinsed off with water to remove excess large grits.

3.12.3 Polishing Operations

Once the sample had been ground to 600 grit, further polishing was performed using a LECO Polisher Grinder Table with progressively finer polishing media. Although the polishing steps used varied throughout the course of this research due to availability, a typical representation of these steps is listed in Table 3.1.

Table 3.1: Typical Fine Polishing Stages

Step	Polishing Pad	Lubricant/Media
1)	LECO 800 Grit SiC	Water
2a)	LECO 1200 Grit SiC	Water
2b)	Allied Final P	Red Lube / 3 micron diamond paste
3)	Allied Final P	Red Lube / 1 micron diamond paste
4)	Allied Final-POL	Allied 0.04 micron Colloidal Silica Suspension

Between each polishing step the samples were washed with a cotton ball and soapy water, rinsed, and then placed in an ultrasonic bath in ethanol for approximately 5 minutes. After being removed from the bath, they were force dried with compressed air.

3.13 Melting Charge Preparation

All of the samples discussed in this research were originally created through a melting process by combining an assortment of master alloys and pure Al ingots. Calculations used to determine the ratios of these ingredients required for target compositions, methods employed to prepare these charges, and special considerations will be considered in this section.

3.13.1 Calculations of Charge Materials

As alloy composition in this research is displayed primarily in atomic percent (at%), calculating the masses of master alloys required for charges first required the conversion of the target at% to weight fraction, as described in Equation 3.1. Once the weight fraction of each elemental composition was known, the mass of each element in the target alloy could be determined by multiplying the weight fraction by the target alloy mass. Dividing the mass of each element by the weight fraction of that element in the relevant master alloy yielded the mass of the master alloy required. Once all master alloy masses were calculated, the remainder of the target mass was accounted for with pure Al (99.99%).

$$wt\%_{x1} = 100 * \frac{at\%_{x1} * m_{x1}^{atomic}}{\sum(at\%_i * m_i^{atomic})}$$ Equation 3.1

3.13.2 Preparation of Charge Materials

Charges for use in melt spinning and the various melting operations employed in this research were prepared through the combination of the master alloys depicted in Table 3.2.

Table 3.2: Master Alloy Compositions and Suppliers

Name	Composition	Supplier
Pure Al	99.99at%Al	Belmont Metals
Al-Sc	Al-1.2at%Sc	KB Alloys
Al-Zr	Al-3.2at%Zr	KBM Master Alloys
Al-Cu	Al-30at%Cu	Milward Alloys

A horizontal band saw was used to slice each of the relevant master alloys into pieces small enough to fit in the relevant crucible (e.g., ~1.5 cm x ~1.5 cm for melt spinning). Generally more pieces were cut than were required, to allow easier pairing of pieces to achieve target weights. Once the pieces were all cut, a metal rasp was used to remove the burrs from the edges of each piece to allow easier cleaning. All sections were then scrubbed individually with soapy water and placed in an acetone-filled ultrasonic bath to remove any coolant or metal residual contaminants left over from the cutting operations.

After removal from the bath and drying, the samples were weighed with a Mettler balance (0.0001 g resolution) and sorted into small piles with total weights similar to the target weights for individual charges. A hand saw was used to cut down samples if they were more than ~0.1g too large and there were no better alternatives. A pair of end cutting nippers was used for fine-tuning the weight to achieve the target mass, as described in Section 3.11.2.

All final charges for melt spinning had a mass of approximately 30 g. All charges created for the arc melter had a final mass of approximately 10g, and all charges for the VIM had a target mass of approximately 600g.

3.13.3 Special Considerations for Charge Materials

Due to the large amount of primary precipitation caused by the high concentration of Sc and Zr in Al-Sc and Al-Zr master alloys and the density differences between $Al_3(Sc,Zr)$ precipitates and liquid Al, primary precipitates formed during the initial casting of ingots consistently sank to the bottom of the ingot. This results in ingots with significant segregation, with the lower section being Sc/Zr rich (~6.9at% in the case of Zr) and the upper section having the same composition as the solubility limit for Sc/Zr in Al. Line scans taken vertically on cross sections of the ingots with EDS showed that the transition between the lower and upper region was sudden and that the composition did not vary significantly from the mean within each region. In addition, thresholding to determine area fraction of SEM and optical images (Figure 3.13) taken from both of the regions was

found to be sufficient in determining the compositions by assuming precipitates were 25% (Sc,Zr) and the matrix was dilute.

In order to reach target compositions when making charges with these alloys, there were two main tactics employed, depending on the amount of master alloy required. The first method, used almost exclusively with the Zr master alloys due to their high average concentrations of 5-10wt% Zr, was to remove and discard the dilute upper region and assume that the remaining portion was homogenous (as was indicated with random sampling through microstructural and ICP-OES analysis). In the Al-Sc master alloys, which were lower in concentration (1.6-2wt% Sc) and therefore used in larger amounts, it was possible cut and use thin, representative vertical slices as depicted in Figure 3.14.

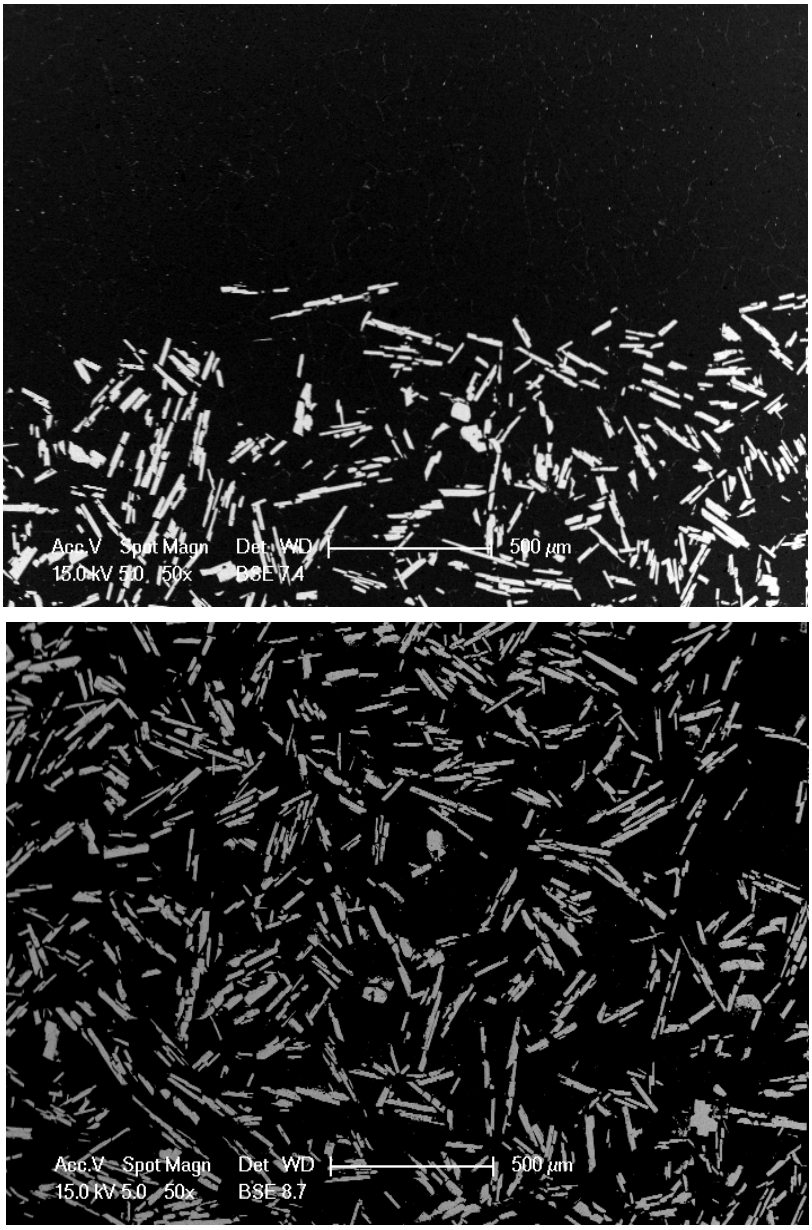

Figure 3.13: These BEI images taken from within the Al-10wt%Zr master alloy demonstrate the morphology of the Al-Zr, and to a lesser extent Al-Sc, master alloys. The first image shows the gravity induced transition from Zr-poor to Zr-rich regions within the alloy. The second image is representative of all images taken below the transition. Thresholding yields similar area fractions of precipitate for all such images.

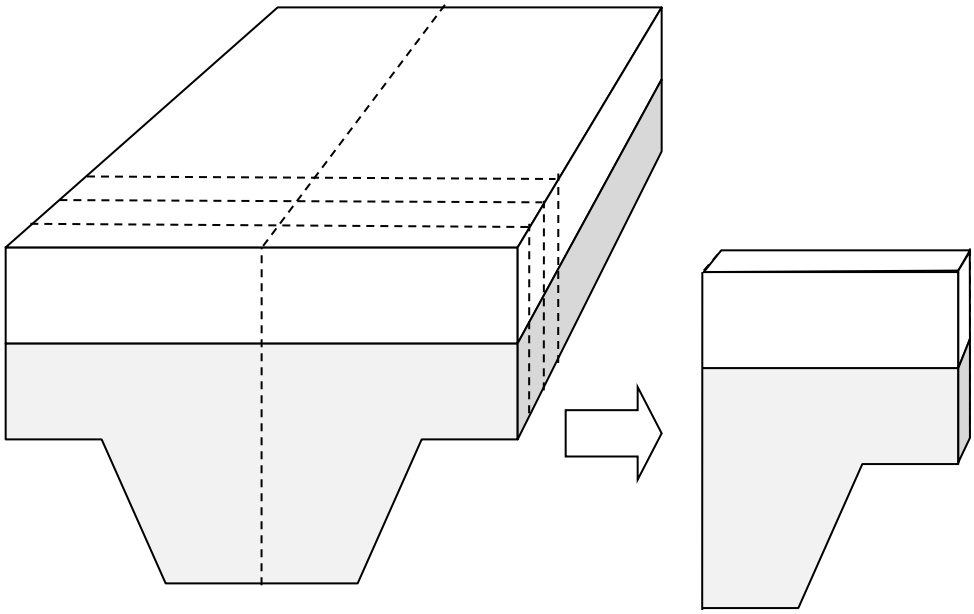

Figure 3.14: This schematic demonstrates the general method used to cut uniform samples out of a gravitationally segregated master alloy (such as Al-Sc and Al-Zr). The grey sections are Sc/Zr/etc rich regions, the white sections are dilute Al, and the dotted lines are where the sample should be cut. Each of the resulting pieces were approximated to have the same composition, and all sample compositions were verified with ICP after melting.

3.14 Vacuum Induction Melting

Chapters 4 and 5 deal with samples that were originally created using melt spinning, but Chapters 6 and 7 deal exclusively with bulk samples, which required the use of alternate methods. This section discusses the primary bulk sample creation methods vacuum induction melting.

3.14.1 Vacuum Induction Melter Overview

The vacuum induction melter (VIM) is a vacuum chamber that is outfitted with a tiltable induction coil. The coil is positioned in such a way that a 60 mm dia. by 170 mm tall graphite crucible can be inserted into the middle, to allow for the melting of ~600g of aluminum charge materials. The coil is also set up to use a computer program to tilt the crucible consistently (discussed briefly in Section 3.14.2), pouring the molten metal into the mouth of an awaiting permanent mold (discussed in Section 3.14.3). While the crucible is positioned vertically for melting, a quartz viewport positioned at the top of the chamber allows temperature observation with a Accufiber HF-3 optical pyrometer. The chamber itself is vacated through the combined use of a rough mechanical vacuum pump and a diffusion pump to a vacuum level of around $1x10^{-5}$ Torr.

3.14.2 Computer Assisted Pouring Program

Prior to this research, casting in the VIM was entirely done with manual tilting of the crucible. Because the chamber only allowed visibility during the pour from limited angles, and because it was very difficult to reposition the mold within the chamber after the door had been closed, it was not uncommon for differences in mold placement and pouring speed between operators to cause near misses and wasted pours. To fix this, a system was developed and installed to make the pour velocity (and in turn the positioning required for the mold) consistent.

For the mechanical portion of the system, an Applied Motion Products STM 23S-3AE stepper motor was affixed to the VIM in such a way that it could be slid into position to mesh with a large half gear attached to the induction coil tilt axis. The stepper motor communicates and is controlled by serial commands through a dedicated computer via an RS-232 port.

The program to control the stepper motor was written in LabView, and is shown in detail in Appendix A.1. A link to the downloadable guide to stepper motor serial commands is included to describe the commands used. The user interface gives options to adjust acceleration, velocity, and tilt position variables for the coil, although the numbers fed to the stepper motor are run through a series of constant multipliers (gear ratios, etc.). One downside to this program is that it assumes it is at step 0 when it is first run, so in cases where the program is terminated at a position other than step 0 (such as when the coil is fully tilted), the gears will need to be disengaged and repositioned before the next use.

3.14.3 Design of the Permanent Mold

When casting materials in the VIM, it was necessary to have a mold to pour into. Previously at Michigan Tech, an efficient permanent mold had been developed for creating sample rods with minimal porosity and diameter of ~19mm. This sample morphology is easily cut, mounted for analysis, turned into tensile bars, or swaged. Simulations of the mold using Magmasoft software show laminar flow through the four rod features of the mold. In addition, the effect of shrinkage porosity is mitigated because of the runner acting as a bottom-feeding riser (Figure 3.15). Unfortunately, the original

permanent mold was physically too large to place in the vacuum chamber, and the volume of liquid metal required to fill it exceeded the capacity of the VIM crucibles. With this in mind, the original SolidWorks mold design files were modified, and a smaller version was developed and subsequently machined out of grey iron using a CNC. Grooves were milled into the side of the mold along the mating surface edge to allow for the prying apart of the two halves.

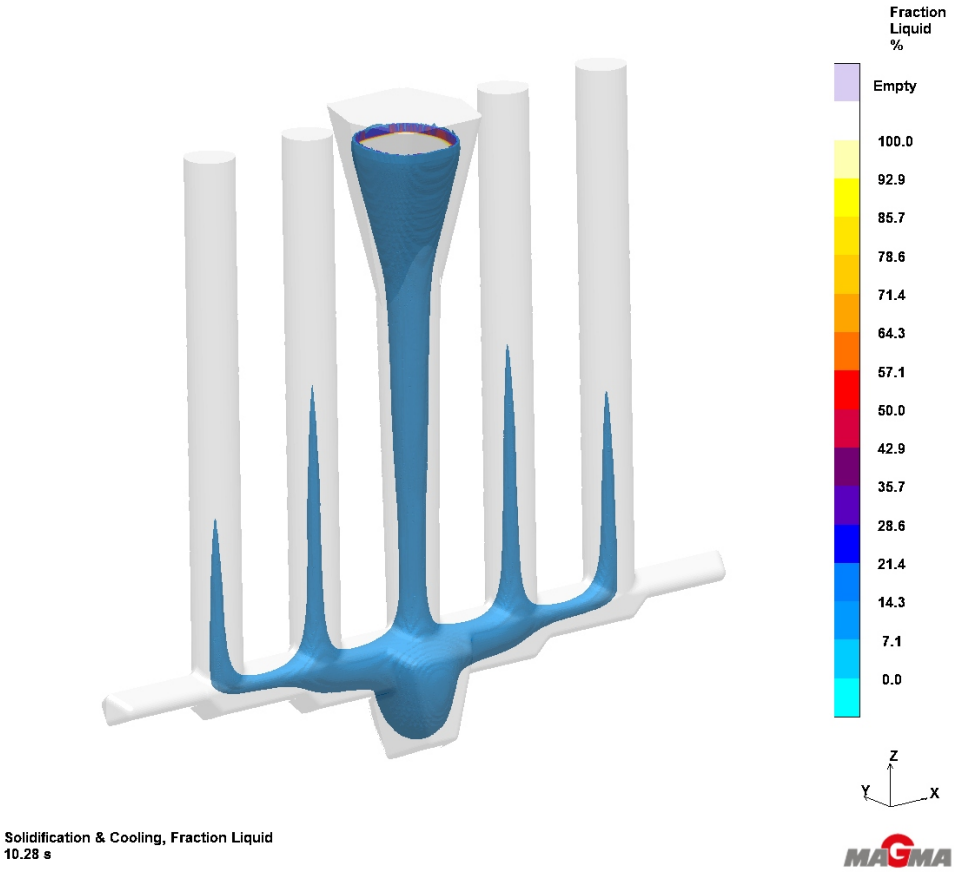

Figure 3.15: This image is a screenshot of a Magma simulation for the mold used to cast cylindrical samples. The colored sections of this image denote the fraction liquid remaining as the part solidifies. As the simulation continues, the sprue and runners fully solidify last, and head pressure from the sprue causes bottomfeeding of the cylindrical samples.

The general design of the mold has several distinct benefits. Firstly, it was designed to create enough material for multiple tensile tests in one pour. Also, it was designed to fill from the bottom, vastly reducing the turbulence within the rods. The stepped riser also played a significant role in reducing turbulence, as the cross sections of the runner progressively reduced simultaneously as the liquid Al stream reached the cylinders and was split between two paths. Finally, having a sprue and sprue basin that were thicker than the cylinders allowed the cylinders solidify first. Because of this, any shrinkage porosity that may have formed within the bottom half of the cylinders was mitigated by a bottom-feeding riser effect.

3.14.4 General Operation of the VIM

While the exact process and parameters varied throughout the course of this research depending on the goal and on past experience, those differences will be discussed in the relevant experimental chapters. This section describes typical operating procedures.

To first prepare the chamber for a pour, all cooling water, pneumatic lines, and electronic components were turned on. The chamber was vented, and latex gloves were donned for working within the chamber. With the computer program, the induction coil was sent to and left in the fully tilted position, so that the assembled permanent mold could be positioned to properly receive the pour. Once the mold was adequately placed, the coil was returned to its vertical position. Appropriately weighed and cleaned charge materials

were arranged loosely, but compactly so as to fit, inside a graphite crucible (60 mm internal dia. by 170 mm) , which was then inserted into the induction coil.

The chamber was then sealed, and the vacuum level was reduced to approximately $9x10^{-5}$ Torr with the assistance of a mechanical rough pump and a diffusion pump. At this point, the induction coil and pyrometer were powered on, and the sample began inductively heating. Checking on the sample regularly for unexpected behavior, the sample was allowed to reach 673K (400˚C) before the vacuum pumps were isolated and the chamber was backfilled with ~684 Torr of ultra high purity (5N) argon. Once the temperature reached the target value, induction power was reduced to maintain the temperature for a time (usually 10 minutes, depending on the experiment) to allow for full dissolution and mixing of the master alloys. After the time was achieved, the crucible was sent to and held at the fully tilted position, to allow the molten metal to pour into the mold. The crucible was returned to vertical, and the chamber was vented and opened once the pyrometer again read below 673K (400˚C). The sample was knocked out of the mold and allowed to cool to room temperature, and the chamber was closed back up and briefly evacuated.

Chapter 4: Precipitate Evolution and Strengthening in Rapidly Solidified Supersaturated Al-Sc and Al-Zr Alloys

Submitted for publication in Metallurgical and Material Transactions A

4.1 Abstract and Background

4.1.1 Abstract

Because of the low diffusivities of scandium and zirconium in aluminum, trialuminide precipitates containing these elements have been reported to possess excellent thermal stability at temperatures of 573K (300˚C) and higher. However, the relatively low equilibrium solubilities of these elements in aluminum limit the achievable phase fraction and, in turn, strengthening contributions from these precipitates. One method of circumventing this limitation involves the use of rapid solidification techniques to

suppress the initial formation of precipitates in alloys containing higher solute compositions. This work specifically discusses the fabrication of supersaturated Al-Sc, Al-Zr, and Al-Sc-Zr alloys via melt spinning, in which supersaturations of at least 0.55 at% Zr and 0.8 at% Sc are shown to be attainable through XRD analysis. The resulting ribbons were subjected to a multistep aging heat treatment in order to encourage a core-shell precipitate morphology [1], the precipitate evolution behavior was monitored with XRD and TEM, and the aging behavior was observed. While aging in these alloys is shown to follow similar trends to conventionally processed materials reported in literature, with phase fraction increasing until higher aging temperatures cause a competing dissolution effect, the onset of precipitation begins at lower temperatures than previously observed and the peak hardnesses occurred at higher temperature steps due to an increased aging time associated with increased solute concentration. Peaking in strength at a higher temperature doesn't necessarily mean an increase in thermal stability, but rather emphasizes the need for intelligently designed heat treatments to take full advantage of the potential strengthening of supersaturated Al-Sc-Zr alloys.

4.1.2 Introduction

Aging in Al-Sc alloys with compositions low enough to allow for homogenization has been observed to form coherent $L1_2$ precipitates [7]. These precipitates demonstrate a higher thermal stability than current commercially available Al alloys as a result of Sc having a relatively low diffusion coefficient in Al and a mismatch strain of only 1.32% between the matrix and precipitate phase [7]. One downside to using Sc as a strengthening addition is the low maximum equilibrium solubility of only 0.23 at%[7].

A frequently used supplemental addition in Al-Sc alloys is zirconium, as it has a lower diffusion coefficient than Sc and forms a metastable, coherent $L1_2$ precipitate. These properties result in an aged microstructure in which the precipitates have Sc-rich cores and Zr-rich outer shells. The external shell of Zr acts to limit the coarsening behavior of the Sc atoms at temperatures up to 723K (450˚C)[15] because of a diffusivity two orders of magnitude smaller than that of Sc and a mismatch strain of only 0.75%. The drawback of using Zr in this manner is that it has an even smaller maximum equilibrium solubility in Al than Sc does, at only 0.078 at%[7].

These trialuminide precipitates offer the most strength to the alloy when the order strengthening mechanism is dominant at precipitate radii between 1 and 3 nm[16][17]. At larger radii, Orowan strengthening becomes dominant as it becomes more efficient for dislocations to loop around precipitates than shear through them[16][19][20][21]. Both mechanisms provide increased strength with an increase in total phase fraction of the precipitate phase, but Orowan strengthening is also dependent on the average radius of the precipitates, decreasing in effect as the radii increase.

The experiment discussed in this work was designed to study the precipitate evolution and strengthening effect of alloys that have higher-than-equilibrium supersaturations and are subjected to a multistep heat treatment. These alloys were created with a process known as melt spinning, which continuously casts a thin ribbon (20-100μm thick in this experiment) onto a quickly spinning copper wheel. These thin ribbons can solidify at rates of 10^5-10^7 K/s, which is rapid enough to suppress the formation of primary

precipitate phases in alloys with high supersaturations of Sc and Zr to create a homogenous solid solution[3].

4.2 Structure of Experiments

The rate of solidification and resulting undercooling achieved in the melt spinning process has a direct effect on the amount of Sc and Zr supersaturation possible in the Al ribbons. To determine the maximum achievable supersaturation values, a series of alloys with different concentrations of Sc and Zr were first melt spun and analyzed with x-ray diffraction (XRD). By observing how the lattice parameter of the Al matrix changed with increasing solute concentration, it was possible to determine the solute content at which primary precipitates start to form. The relation of lattice parameter to solute concentration is linear; the deviation from linearity at increasing concentrations can be assumed to be due to differences in the bulk concentration and the solute concentration [3]. All bulk compositions were measured using inductively coupled plasma optical emission spectroscopy (ICP-OES).

Once the relevant limits of solute concentration were found, ribbon was processed for 3 different low alloy aluminum compositions: one with a Sc addition, one with a Zr addition, and one with both Sc and Zr. A portion of ribbon from each alloy was analyzed using XRD to determine the lattice parameter. After this initial analysis, the XRD sample and the remaining ribbon were subjected to a multistep heat treatment. Between each step

of the treatment, further XRD analysis was conducted, and at several temperatures ribbon was removed to create transmission electron microscopy (TEM) specimens.

4.2.1 Determination of Achievable Supersaturation Levels

The XRD procedure is described fully in Sections 3.3 and 3.6, which is briefly summarized here for ease of reference. For each melt-spun alloy, melt spun ribbon was milled in a Spex ball mill for 1 minute and subsequently compacted at 70 MPa and room temperature into a 25 mm diameter puck. Using a powder x-ray diffractometer, several characteristic peaks of the FCC Al phase were collected and used to calculate lattice parameter values. While each peak on a given scan describes the same lattice parameter, sample displacement can introduce systematic errors that diminish as the angle of diffraction, 2Θ, approaches 180˚. At such an angle, the displacement error is considered insignificant and the corresponding lattice parameter value considered true. Plotting the calculated values of each peak in a given scan against a function of 2Θ known as the Nelson-Riley function results in a straight line with an extrapolated y-intercept corresponding to the true lattice parameter value [32].

4.2.2 Melt Spinning Overview

The melt spinning procedure is described fully in Section 3.1, which is briefly summarized in the following description. Crucibles were prepared from 25 mm quartz tubes with a 0.7 mm orifice. The interior of the tubes were coated with aerosolized yttria (ZYP Coatings) to minimize the $3SiO_2 + 4Al \rightarrow 2Al_2O_3 + 3Si$ reaction at high

temperature and therefore minimize the amount of Si contamination in the melt. The charges were melted under an argon environment and held for 1 minute at 1373K (1100˚C), as observed through a quartz window by a Micro-Epsilon ratio pyrometer (0.5% accuracy, 5 ms response time). Melt spinning was conducted with a wheel speed of 1500 rpm in a 99.999% purity argon environment, backfilled after a vacuum level of $8x10^{-5}$ Torr was reached. After cooling, the ribbon was removed from the chamber and stored in air. The ribbon was several meters long with cross sectional dimensions of ~50 μm x ~3000 μm.

4.2.3 Heat Treatment and Testing of Melt Spun Ribbon

The heat treatment schedule was chosen for easy comparison with the literature [16,29], and is thus a multistep heat treatment with 3 hour holds at increasing temperature steps from 473 to 898K (200 to 625°C) (Figure 4.1). Compacted pucks were subjected to this heat treatment in a vacuum furnace at $1x10^{-5}$ Torr. Between each step, the furnace was flooded with argon and the samples were removed for XRD lattice parameter analysis. A ribbon specimen for each alloy was heat treated in the same furnace, and segments were removed at several steps for TEM imaging.

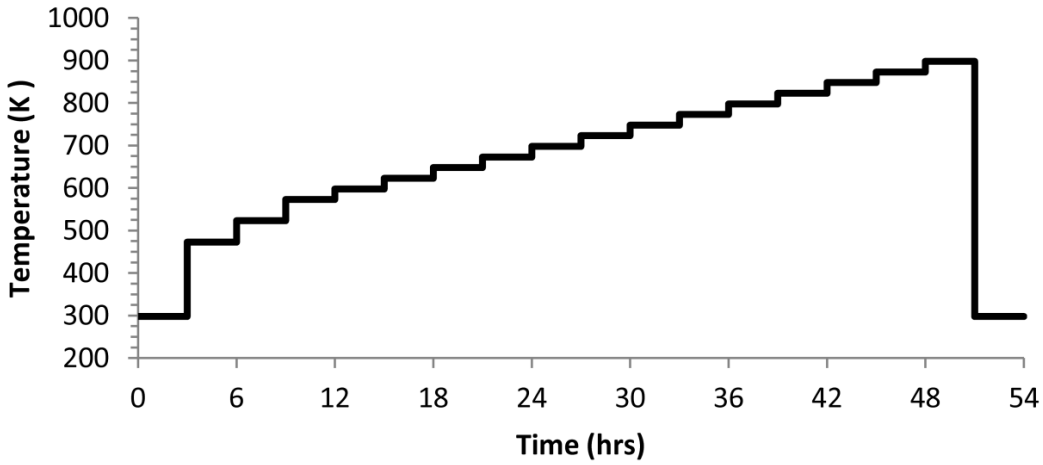

Figure 4.1: Multistep heat treatment used in this experiment and in literature. Each heat treatment step was held for 3 hours [16,29].

4.3 Results and Discussion

4.3.2 Extent of Initial Supersaturation

Figure 4.2 shows an example of a Nelson-Riley extrapolation to determine the true lattice parameter of an alloy (specifically an Al-0.4 at%Sc ribbon). The true lattice parameter of the matrix in the alloy can be determined from the y-intercept, and is presented in Figure 4.2 with error bars representing 2 standard deviations of the intercept. The slope of the line is dependent on the extent of displacement error. It is important to note that the standard deviation of the intercept for this extrapolation in each sample remained relatively constant between $3x10^{-5}$ and $4x10^{-6}$ nm regardless of the slope.

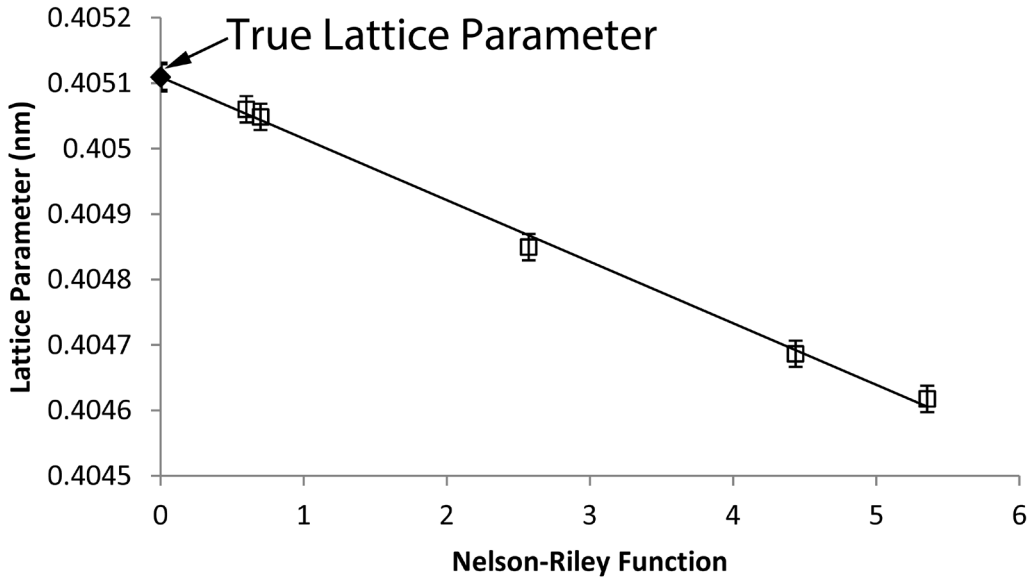

Figure 4.2: Nelson-Riley extrapolation to determine the true lattice parameter of the matrix phase, using XRD data gathered from compacted Al-0.4 at%Sc ribbon.

As outlined in Section 4.2, melt spun ribbons of progressively increasing alloy concentrations were analyzed with ICP-OES to verify their composition as well as with XRD to determine their lattice parameters. So long as the lattice parameter changes linearly with increasing solute, it is assumed that the solute atoms are entirely in solution. Primary precipitation in higher concentration alloys is indicated by a lack of lattice change with further concentration increase. Through this analysis it was found that Sc can be forced into solution with a concentration of at least 0.8 at% with the specified melt-spinning parameters while the achievable solution concentration of Zr was limited to approximately 0.55 at% (Figure 4.3). As both Sc and Zr have < 0.01 at% solubility in Al below 673K (400˚C) [5,9], these solute concentrations are almost entirely supersaturation and available to form precipitates.

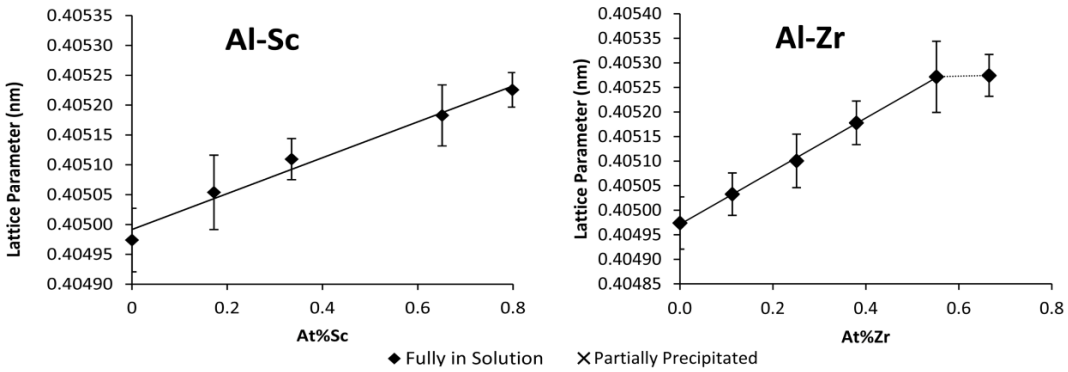

Figure 4.3: Lattice parameter changes of the matrix phase as the concentrations of Sc and Zr are increased. It can be seen that the Al-Zr relationship deviates from linearity, indicating the loss of solute concentration to primary precipitation. Error bars represent standard error of the Nelson-Riley intercept.

4.3.3 Lattice Parameter Change with Heat Treatment

With the information gathered in the last section, the compositions of three alloys were chosen to study precipitate evolution throughout heat treatment. These alloys (Table 4.1) contain Sc and Zr at half the maximum concentration observed in the binaries in Figure 4.3. Another analysis, similar to those described in Section 4.3.2, was performed to verify that ternary alloys with the given Sc-Zr ratio and concentrations above Al-0.4 at% Sc-0.27 at%Zr could be maintained fully in solution with melt spinning. Table 4.1 also lists expected impurity levels from the charge materials as well as the observed impurity levels in the alloys. All concentration levels were verified by ICP chemical analysis. Iron impurity levels are slightly higher than the expected value, calculated with master alloy chemical composition sheets, although literature indicates that Fe precipitates out into

large primary precipitates and has little effect on Sc and Zr based nanoprecipitates [33]. Silicon levels are also considerably higher due to contamination from the quartz tube., with similar Si levels having been shown in literature to increase the diffusion rate of Sc in Al by lowering the vacancy migration energy [33,34].

Table 4.1: Expected and Observed Alloy Compositions

	Al-Sc		**Al-Zr**		**Al-Sc-Zr**	
Element	**Expected**	**ICP**	**Expected**	**ICP**	**Expected**	**ICP**
Sc (at%)	0.400	0.384	-	-	0.400	0.394
Zr (at%)	-	-	0.270	0.266	0.270	0.266
Si (at%)	0.002	0.035	0.002	0.025	0.002	0.021
Fe (at%)	0.001	0.006	0.001	0.005	0.001	0.009

Samples of each alloy were melt spun, compacted into discs, and heat treated. Figure 4.4 demonstrates how the lattice parameter changes for each alloy between each heat treatment step.

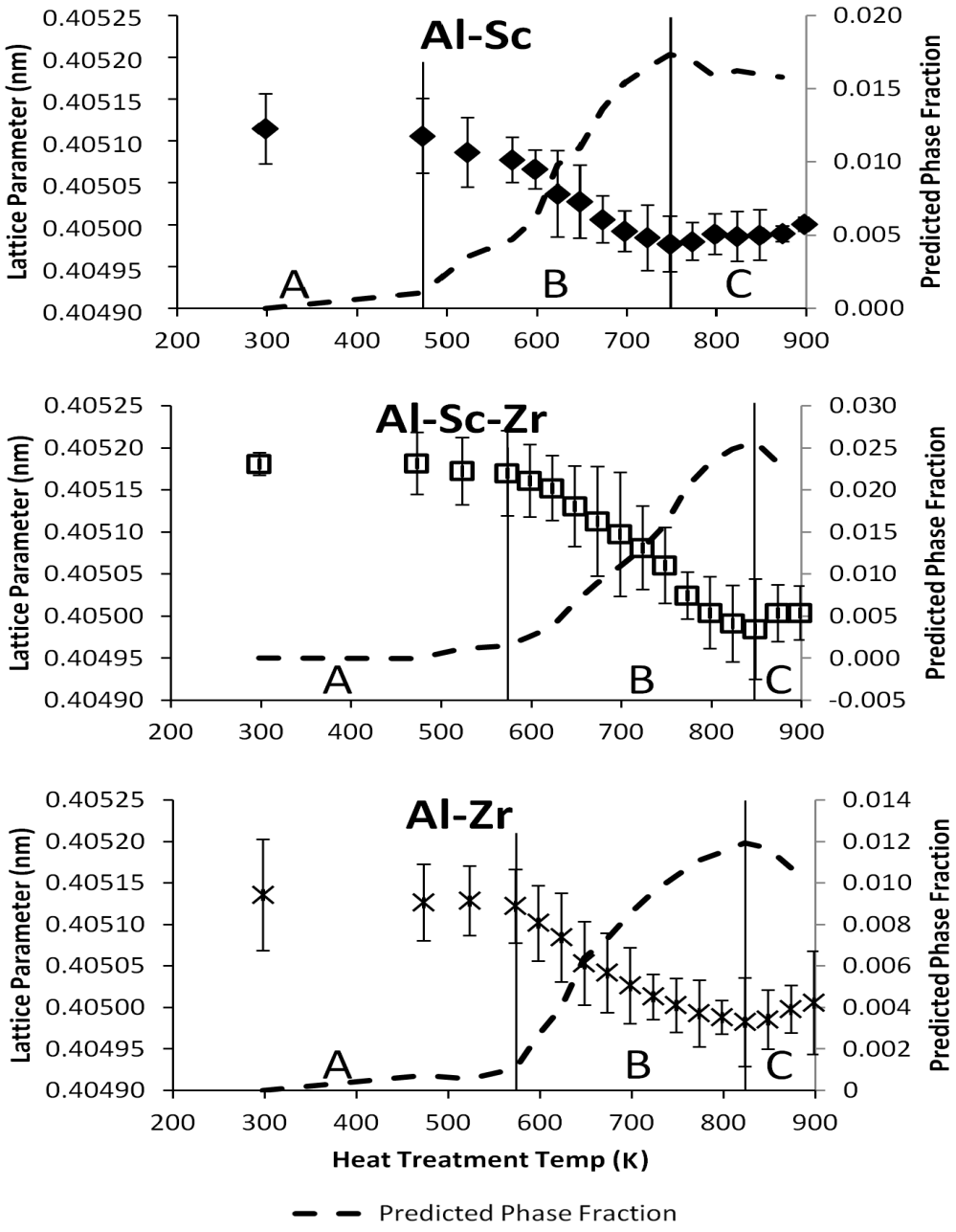

Figure 4.4: Representation of how heat treatment of the 3 alloys affects the lattice parameter of the matrix, which in turn describes the solute concentration. Lattice values are presented with error bars representing 2 standard deviations of the intercept, and the onset of precipitate phase formation and dissolution are also shown.

From these data, it is apparent that precipitation begins at roughly 473K (200˚C) for the Al-Sc alloy and at approximately 573K (300˚C) for the Al-Zr and Al-Sc-Zr alloys. The precipitation onset is lower than that observed in previous work with alloys containing lower supersaturations [16,29], which results from the slightly higher Si concentrations, the lower mean distance between Sc and/or Zr solute atoms, and the higher concentration of Sc and/or Zr that creates a larger driving force for precipitate phase formation. By observing the heat treatment steps where minimum lattice parameter values occurred, it is found that near-equilibrium solute concentrations were reached at 748K (475˚C) for Al-Sc and 823-848K (550-575˚C) for the Zr containing samples, above which precipitates begin to dissolve back into solution as the equilibrium solute concentration increased.

It is important to note that previous literature found the onset of precipitation in Al-Sc-Zr alloys to occur at the same heat treatment step as in Al-Sc alloys. One possible reason that the data in this study suggests otherwise could be that the motion of Sc atoms is impeded by the Zr atoms in solution. In previous works, microsegregation of Zr to dendrites and Sc to interdendritic regions resulted in a bimodal distribution of alloy compositions [16,29], which likely led to binary Al-Sc precipitation behavior in the interdendritic regions. Melt spinning solidification rates are recognized to be in the 10^5-10^7 °C/s range, which would lead to secondary dendrite arm spacing (SDAS) of around or below 1 micron. Although verification of the dendritic arm spacing has been shown to be possible in the literature using WDS, this is only done in cases where the SDAS is on the scale of 10's of microns. In this study, determination of dendritic segregation with

WDS was unsuccessful due to the WDS interaction volume being of comparable size to the assumed SDAS. TEM images could potentially show dendritic segregation of precipitates in the correct orientations, but no segregation was observed in the images taken for radius measurements. With no definitive observation to this effect, it still seems a reasonable assumption that the melt-spun ribbon in this study would likely be less affected by a bimodal distribution of compositions due to dendritic segregation.

In these experiments, it is believed that residual stresses developed during the rapid solidification and ball milling have minimal effect on the lattice parameter measurements. Literature shows that lattice parameter change with ball milling is negligible in aluminum powders for ball milling times significantly longer than in this study [35]. However, analyses performed in the course of these experiments (Figure 4.5) demonstrate that the lattice parameter almost immediately drops to and maintains a slightly lower value. This initial decrease is attributed to the relaxation of residual quenching stresses in the pure Al ribbon, as the stable lattice value reached after the initial decrease is 0.40498 nm, which nearly matches the accepted value for Al. This behavior is not surprising, given that pure Al is known to relieve the majority of quenching stresses and remove excess vacancies within hours or days while being stored at room temperature [36,37]. As other alloys in this study were shown to have nearly identical behavior, and because the alloys in question are still >99.3 at% purity Al and fully solutionized, it was assumed that they also underwent relaxation of residual stresses. Furthermore, because the processing parameters for all melt spinning and milling operations in this work were identical, any differences in residual stresses that may still be present due to processing can be

considered negligible between the ribbon that was analyzed in Section 4.3.2 and in this section. The results from the XRD lattice parameter determination can therefore be used to determine the solute concentration at any given step for the Al-Sc and Al-Zr alloys using the correlation between lattice parameter and solute concentration demonstrated in Figure 4.3. It is important to note that, for any material processed with different parameters, it may be necessary to recreate Figure 4.3 if differing residual stresses were present.

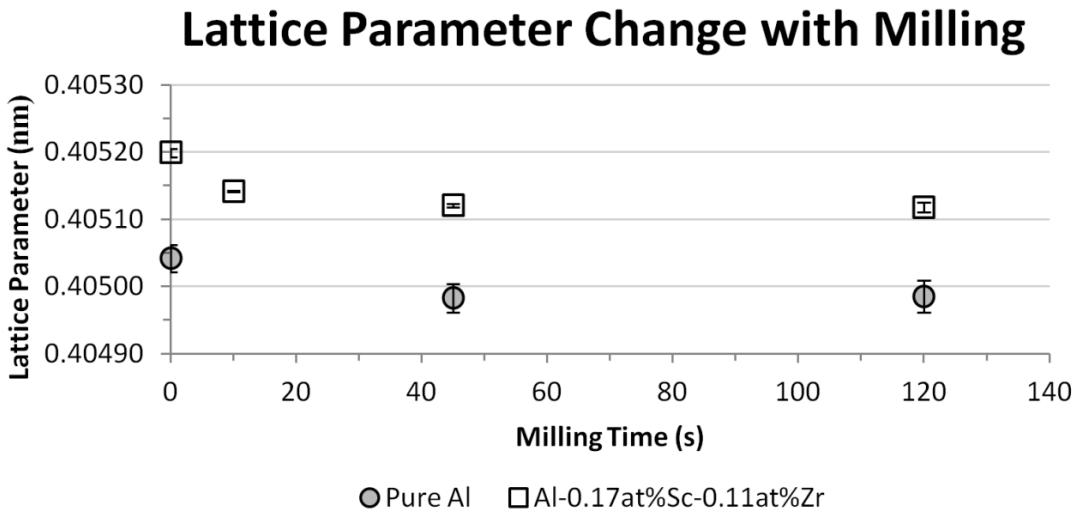

Figure 4.5: Change in lattice parameter of melt spun ribbons as they are subjected to short ball milling times (10-120 s). These results indicate an rapid drop in lattice parameter, attributed to the relaxation of residual stresses.

The solute concentration can then be used to calculate precipitate phase fractions, knowing the original concentration and assuming no other phases were formed as solute atoms left the solution. Unfortunately, the phase fraction of precipitates for the Al-Sc-Zr

alloy can only be roughly estimated in this manner with the use of the assumption that the Sc and Zr solute atoms came out of solution simultaneously in equal amounts. The contribution of each element to the combined lattice parameter change was calculated by observing the ratio of lattice change effects between the binary Al-Sc and Al-Zr alloys.

4.3.4 Transmission Electron Microscopy

At the 673, 748, and 823K (400, 475, and 550˚C) heat treatment steps, sample segments were removed and TEM specimens prepared to determine average precipitate radius. These heat treatment steps were chosen due to predictions of a Lifshitz-Slyozov-Wagner (LSW) kinetic model (Eqns 4.1-4.4) [38,39], evaluated successively at each heat treatment step for the binary alloys with the correct temperature and solute concentration as found by XRD, that the radii at these steps should be significantly distinguishable from each other.

$$\langle r(t)\rangle^3 - \langle r_0(t)\rangle^3 = kt \qquad \text{(Eqn. 4.1)} \qquad [38,39]$$

$$k = \frac{8c_\alpha(1-c_\alpha)\gamma D V_m}{9RT(c_\beta - c_\alpha)^2} \qquad \text{(Eqn. 4.2)} \qquad [38,39]$$

$$D = D_0 \exp\left(\frac{-Q}{RT}\right) \qquad \text{(Eqn. 4.3)} \qquad [38,39]$$

$$V_m = \frac{N_a a^3}{4} \qquad \text{(Eqn. 4.4)} \qquad [38,39]$$

The mean radius of precipitates at time, t, is denoted as $\langle r(t) \rangle$, and can be solved for assuming the initial mean precipitate radius, $\langle r_0(t) \rangle$, is known. The temperature-dependent constant, k, can be determined for each heat treatment step with kinetic and thermodynamic information of the alloy system. The solid solubility of Sc and/or Zr in Al, c_α, was determined using phase diagrams, and the composition of Al_3X precipitates was taken to be 0.25 atomic fraction X. The diffusivity, D, was determined with D_0 values of 2.65×10^{-4} and 7.28×10^{-2} m^2/s, and Q values of 168 and 242 kJ/mol for Sc and Zr, respectively [15,40–42]. The average atomic volume per mol, V_m, was determined with a = 0.4103 and 0.408 nm as the lattice parameters of Al_3Sc and Al_3Zr, respectively [27,43]. At each heat treatment step, t is reset to zero and growth continues with $\langle r_0(t) \rangle$ as the average radius achieved in the last step [44].

Figure 4.6 shows several representative TEM images, and Figure 4.7 describes the change in number averaged radius for each alloy, with error bars representing standard deviations of the non-normal size distributions. For the sake of transparency, a representative histogram showing the common distribution trend of being skewed toward smaller precipitates has been included as Figure 4.8. While it appears that TEM-observed radii in Al-Zr are larger than predicted by the LSW model, this is to be expected as larger precipitates are more easily observed and therefore likely over-represented. Other than this discrepancy, this analysis found the predicted radii of the LSW model to be in relative agreement with the TEM results.

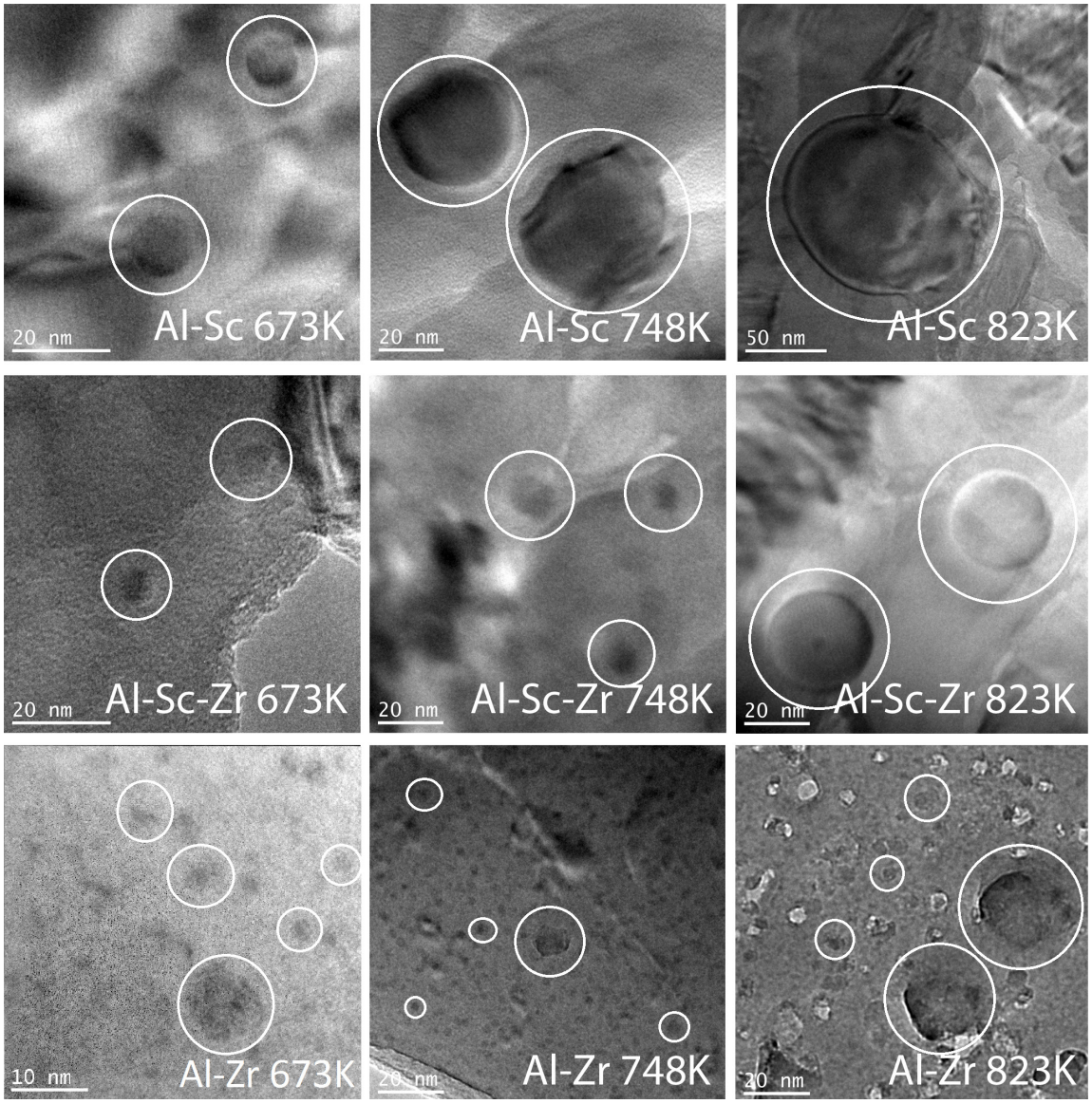

Figure 4.6: TEM images of representative precipitates over the course of multistep heat treatments in each alloy. Note the different scale for the Al-Sc alloy at 823K (550˚C).

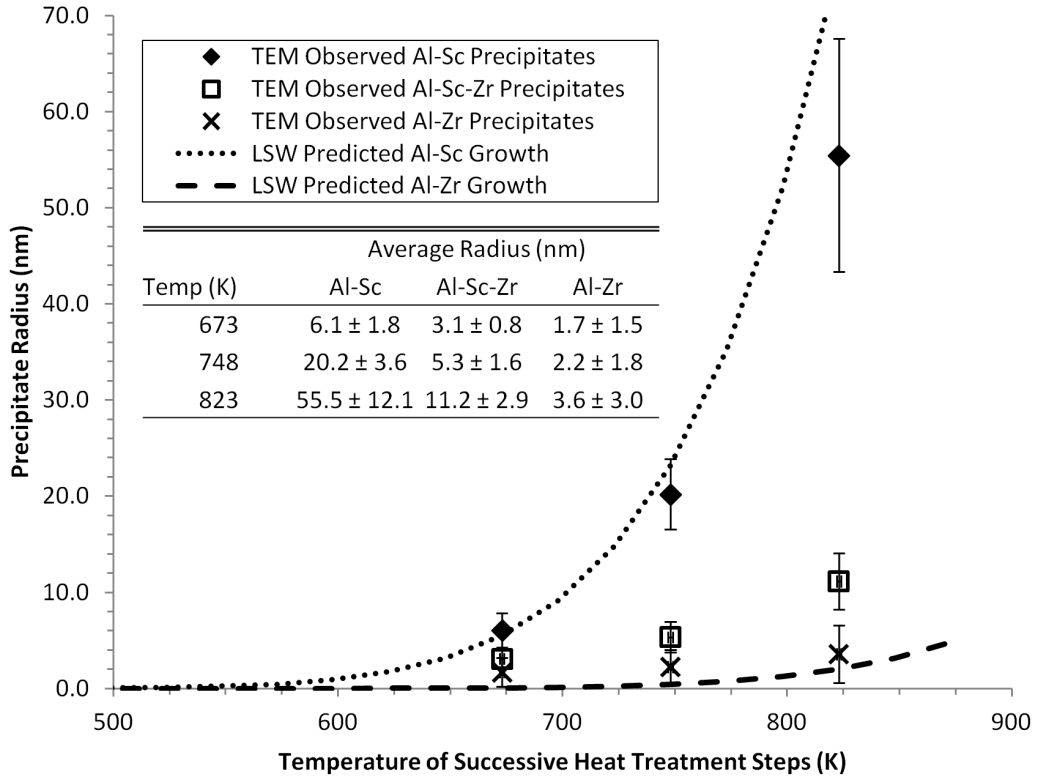

Figure 4.7: Increase in average precipitate radius over the course of a multistep heat treatment, as determined from TEM image analysis (symbols) and predicted by LSW theory (lines) for the binary systems.

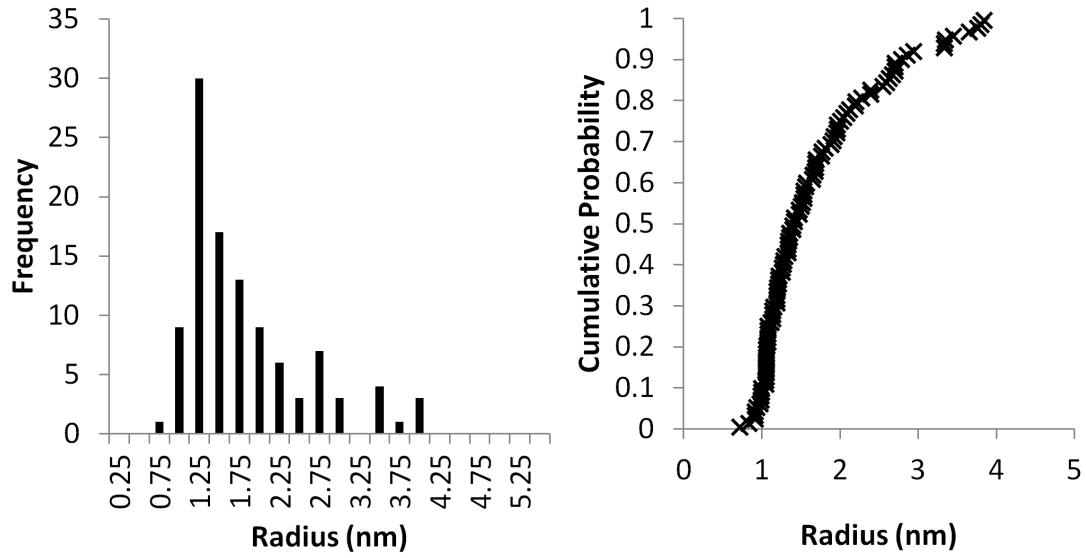

Figure 4.8: A histogram of precipitate radii in Al-Zr at 673K (400˚C), as observed by TEM. It should be noted that these precipitates are not normally distributed, and that precipitates at the smaller end of the distribution were observed more frequently.

As shown in Figure 4.7, The average precipitate radii of the Al-Sc alloy coarsens much more rapidly than the Al-Zr and Al-Sc-Zr alloys, with an increase in radius ~20 times greater than that of Al-Zr and ~6 times greater than that of Al-Sc-Zr between the last two TEM observations. The increased coarsening resistance of precipitates in the Al-Sc-Zr alloy is consistent with literature, and can be attributed to the existence of Zr-rich outer layers of the precipitates [16,29]. Because the LSW model is verified by this TEM analysis and literature [45], it can be used to predict the average precipitate radius at the end of each heat treatment step for the binary alloys. The average radii in the Al-Sc-Zr alloy throughout heat treatment can be extrapolated from the TEM images.

4.3.5 Prediction of Precipitate Contribution to Strength

With knowledge of the average precipitate radius and phase fractions at each aging step for each alloy, it is possible to estimate the strengthening effects of the two main mechanisms in this system: namely, order and Orowan strengthening [16–18].

Order strengthening is described in Section 2.2.2. The order strengthening effect does not vary with precipitate radius change, but increases with phase fraction. This means that the order strengthening effect increases during phase formation (both nucleation and growth) and reaches a plateau when the solute levels reach equilibrium [19,20].

The Orowan strengthening equation is described in Section 2.2.3. The Orowan strengthening effect increases with phase fraction but simultaneously decreases with growing precipitate radius. This results in an initial increase in strength as precipitate phase is formed, followed by an overaging effect as coarsening continues to increase the average precipitate size at later heat treatment steps even after all possible precipitate phase is formed [19,20].

Figure 4.9 shows predicted order and Orowan strengthening effects of each alloy calculated by inputting the measured precipitate radii and phase fractions for each heat treatment step into the equations from Sections 2.2.2 - 2.2.3. The mechanism with the lowest strengthening effect will be dominant, so it can be seen that the precipitate strengthening of each alloy is expected to have reached a peak when the dominant mechanism transitions from order strengthening to Orowan strengthening mechanisms.

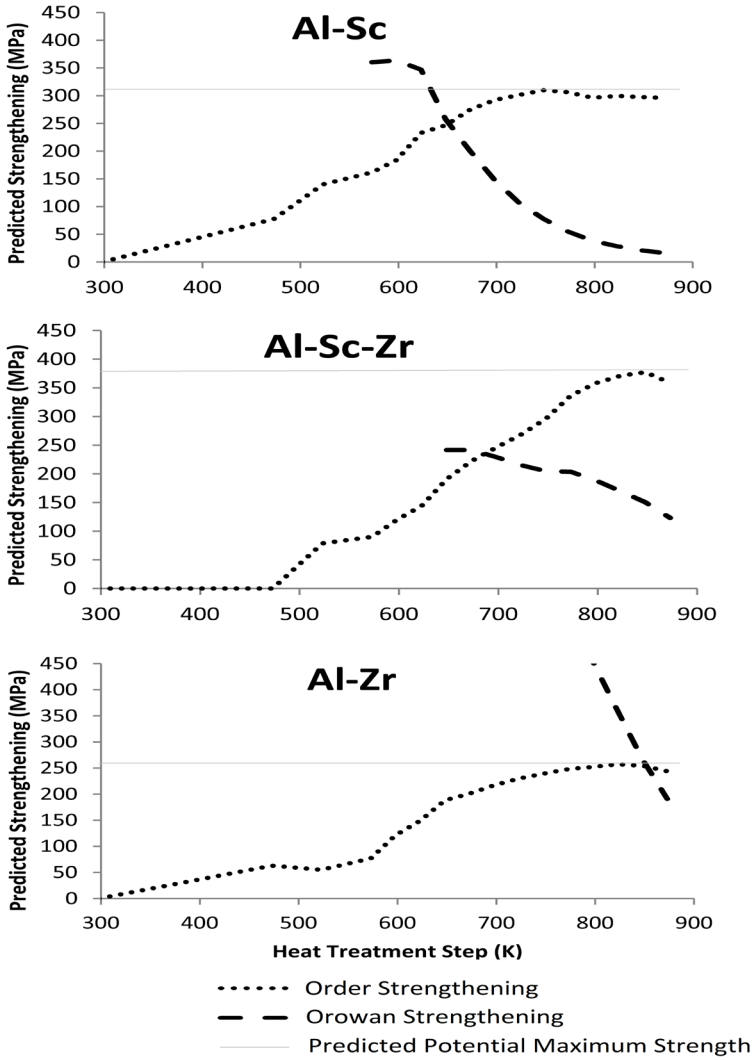

Figure 4.9: Predicted precipitate strengthening effects for each alloy throughout the heat treatment. The dominant strengthening mechanism is whichever has the lowest strengthening effect at a given heat treatment step. Therefore the peak observable strengthening is the intersection of the two mechanisms. This is shown to be lower than the maximum potential order strengthening effect for the two Sc containing alloys, which means these alloys should be able to achieve higher strengths if the heat treatment schedule is adjusted.

By these calculations it is predicted that each of the alloys will reach a peak strength of ~250 MPa. However, only the Al-Zr alloy existed in a state where order strengthening was able to reach its full potential, because in both Sc containing alloys the average precipitate radius exceeded the optimal 1-3 nm range before the supersaturated solute atoms were entirely converted into precipitate phase and the decreasing Orowan strengthening mechanism became dominant. Increasing the nucleation density and/or decreasing the coarsening effect through the use of longer heat treatments at the lower temperature steps should improve the predicted peak strengthening effect for both Al-Sc and Al-Sc-Zr to ~300 MPa and ~400 MPa, respectively, by allowing these alloys to be fully precipitated while the order strengthening mechanism is still dominant.

4.4 Conclusions

In this chapter, a method for determining the achievable supersaturation of precipitate strengthening alloys under specific solidification conditions was demonstrated through the use of XRD lattice parameter measurements. With this method it was found that Sc and Zr can be supersaturated in Al at concentrations of at least 0.55 at% Zr and 0.8 at% Sc with the rapid solidification setup described in Section 3.1. This supersaturation allows for an increase in achievable precipitation phase fraction over traditionally cast Al-Sc alloys, and in turn, enhanced strengthening. While precipitate strengthened melt spun ribbon is not immediately useful in an industrial setting, the ability to create and study such a material may facilitate the development of new uses.

Multi-step heat treatments of Al-0.4 at%Sc, Al-0.27 at%Zr and Al-0.4 at%Sc-0.27 at%Zr with subsequent XRD and TEM analyses indicate that these alloys begin precipitation at 473, 573, and 573K (200, 300, and 300˚C), respectively, and reach maximum precipitate phase fraction at 748, 823, and 848K (475, 550, and 575˚C), respectively. These analyses also indicate that precipitation in binary Al-Sc and Al-Zr alloys behaves as would be expected by the LSW model at elevated supersaturations, and that ternary Al-Sc-Zr demonstrates behavior between that of either of the binaries. This is interpreted to mean that a core-shell precipitate structure has been formed as in more dilute alloys with similar heat treatment regimens, and the largely Al_3Zr precipitate phase at the outer edge of the precipitate limits the ability of the Sc atoms to move between precipitates. However, there was no direct observable indication of interprecipitate segregation of Sc and Zr within the nanoscale precipitates that were observed during the TEM analysis. Future work should include an analysis of similar ribbons with atom probe tomography, which has been demonstrated to be sensitive enough to observe the segregation in other literature [16], or with a higher resolution STEM/TEM.

Calculations for the predicted precipitation strengthening for these alloys using observed average radii and phase fraction indicate that a greater strength could be obtained with the application of a more suitable heat treatment. Each alloy experienced precipitate coarsening that resulted in the Orowan strengthening mechanism becoming dominant over the more potent order strengthening mechanism, and this occurred before the precipitate phase could entirely form in the Sc containing alloys. By adding the kinetic information gleaned from this study to other sources describing similar heat treatment

schedules in literature [16,29], it should be possible to optimize the fitting of more advanced models, such as the Kampmann-Wagner Numerical (KWN) model, to predict heat treatments that would result in higher number densities of smaller precipitates in these alloys.

This work demonstrates that rapid solidification can be used to create supersaturated Al-(Sc,Zr) alloys with increased precipitation strengthening potential. Two notable downsides to this technique are: 1) melt spinning is not a common industrial process, and 2) the resulting ribbon is not immediately suitable for industrial use. The first downside can be easily overcome if there is an industrial application, as melt spinning can be suitably upscaled by increasing the crucible melt capacity, adding multiple spray nozzles, and incorporating active cooling into the copper wheel. Future work should include attempts to consolidate similar melt spun ribbons into a bulk form without melting in order to maintain the achieved supersaturations and address the second downside, with methods such as Additive Friction Stir processing (AFS).

Chapter 5: Effect of Additive Friction Stir Processing on Supersaturated Al-Sc

5.1 Abstract

In this chapter, supersaturated melt spun Al-Sc ribbons were mechanically mixed into the surface of a pure Al substrate using Additive Friction Stir processing (AFS) in an attempt to transfer the supersaturation and associated precipitation strengthening benefits from the ribbon into a more structurally viable form. While the resulting Sc-enriched surface layer did appear to retain ~0.06at%Sc, thermocouples observing the process recorded temperature spikes up to 816K (543°C), at which temperature the solvus composition for Al-Sc solubility would have been only ~0.07at%Sc [4]. It is unclear whether the final supersaturation in the AFS surface layer reached equilibrium during processing, or whether the limited kinetics of Sc in Al, combined with the limited time at peak temperature, halted matrix depletion before it was complete at lower temperatures. In either case, the resulting AFS surface layer was analyzed using several methods, including Vickers hardness, WDS, and backscattered electron images (BEI). The data gleaned from these methods was examined in several ways, offering insight into the

viability of AFS using Al-Sc ribbon to create a thermally stable strengthening layer and to be used as a screening tool for multiple Al-Sc alloys simultaneously.

5.2 Background

Al-Sc precipitation strengthened alloys generally have low Sc concentrations of 0.1at%Sc or less because of the limited solubility of Sc in Al [4]. These alloys draw their maximum strength from the growth of coherent $L1_2$ ordered precipitates in the 1-3nm range, which take advantage of the order strengthening mechanism [20]. These precipitates notably differ from current precipitate systems in that they are much more thermally stable due to lower relative diffusion rates of the atoms involved in Al ($D_{Sc\ in\ Al}^{400^{\circ}C} = 1.98 \times 10^{-17}\ m^2/s$ and $D_{Cu\ in\ Al}^{400^{\circ}C} = 1.54 \times 10^{-15}\ m^2/s$) [12,13]. Unfortunately, the limited solubility of Sc in Al limits the achievable strengthening effect, and the price of Sc is relatively expensive due to being sourced primarily as a byproduct in other mineral processing operations [1,2,6]. These factors limit the amount of use that this alloy system sees commercially at this time.

One potential method for increasing the strength of these alloys is to rapidly solidify the molten alloy with melt spinning methods to increase the quantity of Sc obtainable in solid solution. This could theoretically result in an increase in strength if the quantity of nanoscale precipitates could be increased without severely changing the average precipitate radius. However, in such a case, average distances between precipitates would be reduced, resulting in a greater ease of coarsening and a lower thermal stability. Other issues with melt spinning this alloy include the ever-present obstacle that melt spun

ribbons are not easily adaptable to useful structural applications, and that increasing the amount of Sc used in these alloys has the negative effect of increasing the cost further out of reach for common use. Finally, it must be acknowledged that increasing the amount of Sc in solution past the maximum equilibrium solubility is a temporary state; once the Sc has been precipitated out, the only way to return it to solution in Al is in the liquid state.

In an attempt to impart the benefits of melt spun ribbons into a more structurally applicable material, this chapter attempts to use Additive Friction Stir processing (Section 3.3) to create a surface layer on a pure aluminum substrate with enhanced Sc supersaturation that was previously only achievable in thin rapid solidification products. Such a method would allow targeted application of Sc to Al parts in order to avoid wasting Sc in nonessential areas and decrease the total amount of Sc required. This method also potentially allows for increased strengthening associated with higher than natural Sc solubility. The absence of melting during AFS inhibits the formation of micron-scale primary precipitates, which drastically improves chances at achieving improved surface layer strengthening. However, solid state coarsening will likely still occur during AFS due to the elevated temperatures seen in the process. Adequate active cooling may limit the amount of time any area of the sample spends at elevated temperatures enough to minimize this effect.

5.3 Experimental Design

According to previous work performed for the Chapter 4 experiments, rapid solidification through melt spinning is an effective method to achieve supersaturation of Sc and Zr in Al alloys. To this end, relevant master alloys were cut into small pieces (Section 3.11) and combined into 30g charges (Section 3.13) to reach the target composition of Al-0.5at%Sc. Each charge was then placed in a custom quartz crucible with internal yttria coating and a 0.7 mm orifice (Section 3.1.1). These crucibles were then placed into the meltspinner, where each charge was individually melted and sprayed against a spinning copper wheel to create rapidly solidified ribbon (Section 3.2-3.3). For these experiments, the melt spinning parameters were: a holding temperature of 1373K (1100˚C), holding time of 2 minutes, wheel speed of 1500rpm, and a chamber backfilled with ~400 Torr of ultra high purity (99.999% purity) argon.

After allowing the ribbons approximately 20-30 mins to cool to room temperature within the argon flooded chamber, the remaining vacuum was dumped and the samples were removed. As described in Section 3.2, the ribbons were then broken up into small flakes using a SPEX 8000-D ball mill and compacted at room temperatures into loose billets of appropriate shape and dimensions for use as a feedstock material for the AFS process. All processing of the ribbons was performed close to room temperature, with close attention paid to avoiding reaching temperatures that would result in Al_3Sc precipitate nucleation and growth. The flakes were fed 0.5g at a time into a custom-made die and compacted in steps until a final weight of 2g was achieved for each sample. Because of the low processing temperatures, special care was required for handling these loosely compacted

samples, as they would easily crumble if dropped or impacted. These final feedstock pieces were then shipped to Aeroprobe to be used in Additive Friction Stir processing (AFS). A subsample of the ribbon was also compacted into a shape conducive to XRD lattice parameter analysis and used to successfully verify that all Sc within the ribbon remained in solution (Section 3.6 and Chapter 4).

Upon arrival at Aeroprobe, the billets were used as a consumable tool in the AFS process, mechanically mixing the supersaturated material into the surface of 1 cm thick, 99.99% Al plates (as described in Section 3.3). Two AFS paths, which affected surface areas of approximately 2 cm in width and 15 cm in length, were applied to each Al substrate. During AFS processing of one sample, thermocouples inserted into holes in the plate collected temperature data at several points along the path. The Al plates were then returned to Michigan Technological University for analysis of the AFS paths.

To allow for analysis of the microstructure and hardness at different depths and distances from path center, multiple cross sections were cut along the AFS paths using a horizontal bandsaw with active cooling (Section 3.11.2). These sections were then simultaneously subjected to a stepped heat treatment in a box furnace (Section 3.4.1) with 3 hour holds at incrementing temperature steps of 25K from 523 to 773K (250 to 500˚C). At each step one of the samples was removed and quenched for analysis to get an accurate assessment of changes to the hardness and microstructure over the course of the treatment. To this end, each of the samples was mounted in epoxy and polished (Section 3.12). Vickers

hardness tests using a load of 10g and a hold time of 15s were then performed on the sample in a grid as described in Section 3.7.

Because the hardness indentation grids spanned from high Sc concentration to pure Al unpredictably as distance from the AFS surface increased, it was necessary to accurately assess the Sc concentration at the location of each hardness test using Wavelength Dispersive Spectrometry (WDS) as described in Section 3.9.3. A WDS analysis point was taken within 50 microns of each Vickers indentation point, at approximately the same distance from the AFS surface as the indent to minimize error due to the concentration gradient (Figure 5.1). While in the SEM, backscatter electron images of the sample were also taken to achieve an idea of the concentration gradient profile (Section 3.92). Other potentially useful analyses, such as conductivity testing, TEM, or APT, were unfeasible for this experiment due to the unpredictable variability of Sc concentration throughout the AFS path effect.

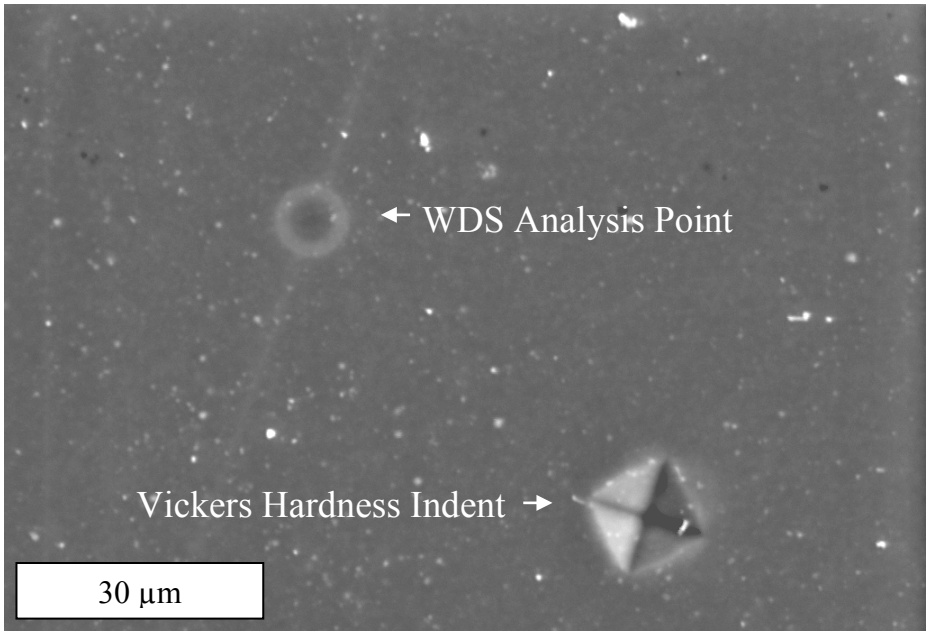

Figure 5.1: This SEI image shows the relative locations of the WDS and hardness indentations, as labeled. These marks were kept with 50 microns at each testing location to decrease negative effects of the concentration gradient.

5.4 Results and Discussion

Having collected hardness and WDS data pairs from a wide variety of compositions and heat treatment stages, it is possible to display the data in several useful arrangements. For instance, it is possible to observe the magnitude and spread of enhanced Sc concentrations across the AFS path cross section, along with a second plot demonstrating the effect that such a concentration profile has on the hardness of the alloy. This approach allows observation of the AFS processing itself. Figure 5.2 indicates the physical locations for hardness/WDS testing in the samples, and Figure 5.3 shows a representative backscatter electron image (BEI) of an AFS path cross section for comparison. This BEI

shows the generally chaotic nature of the Sc distribution within the affected AFS path, as well as the fact that the mechanical mixing did not completely join the layers together. While there does not appear to be a gradual Sc gradient as was initially hoped for, there still exist a wide variety of Sc concentrations to analyze, as indicated by varying shades of grey in the BEI.

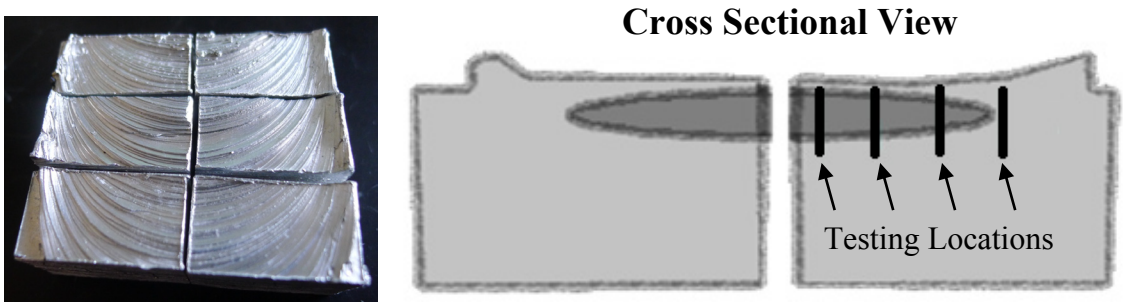

Figure 5.2: In the left image, a photograph of the samples cut from an AFS path is shown. The right image consists of a schematic cross section of the path, as obtained if the samples in the left image were tilted backwards from their current orientation. This schematic shows the Sc rich region, shaded in darker grey, and the locations of hardness and WDS testing for this experiment.

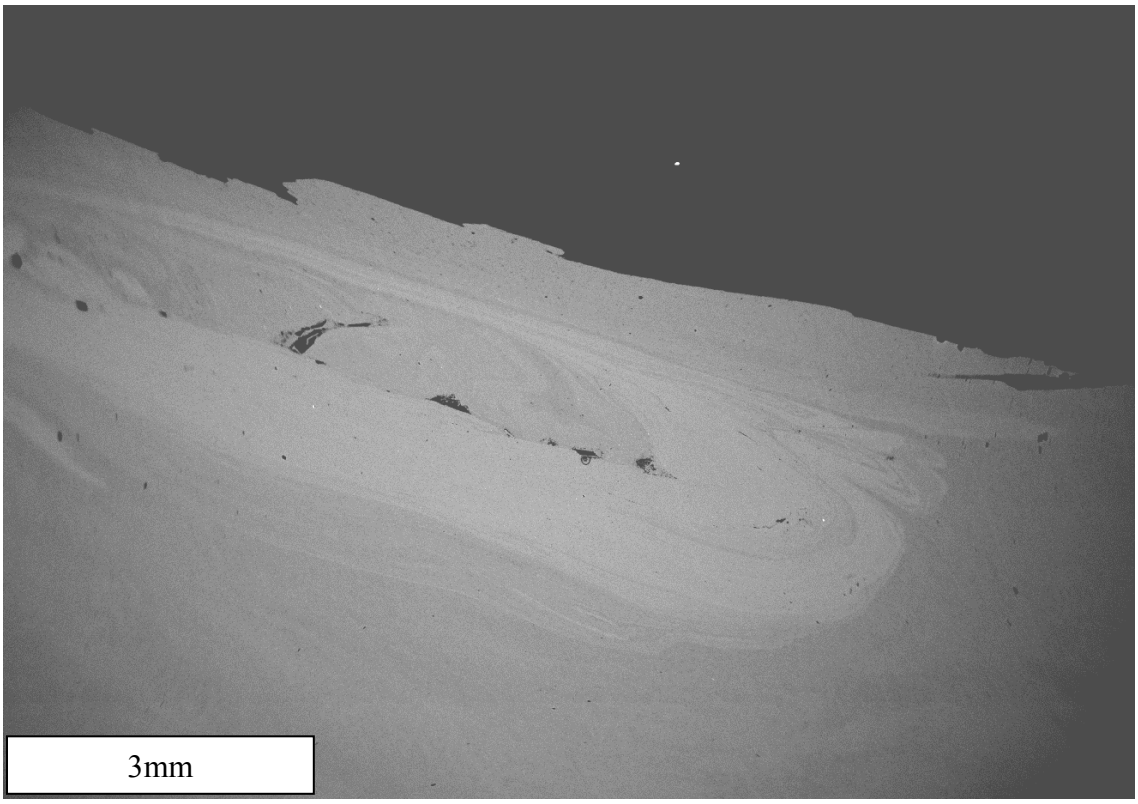

Figure 5.3: This Backscatter Electron Image (BEI) shows the Sc concentration distribution in a cross section of the AFS path. Brighter areas contain greater amounts of Sc, as they have higher atomic mass than Al.

Figure 5.4 shows the WDS and hardness results (converted into MPa and then displayed as approximate yield strength by dividing by 3) for the Al-Sc alloy after enduring stepped heat treatments up to 573K (300˚C). In these 3 dimensional plots, with the X and Y axes describing the physical testing locations on the sample, it is validated that there is a correlation between increasing the Sc concentration and increasing the strength. The considerable noise in these analyses is due to small sample sizes, as the concentration gradient made statistically significant sampling for each concentration difficult.

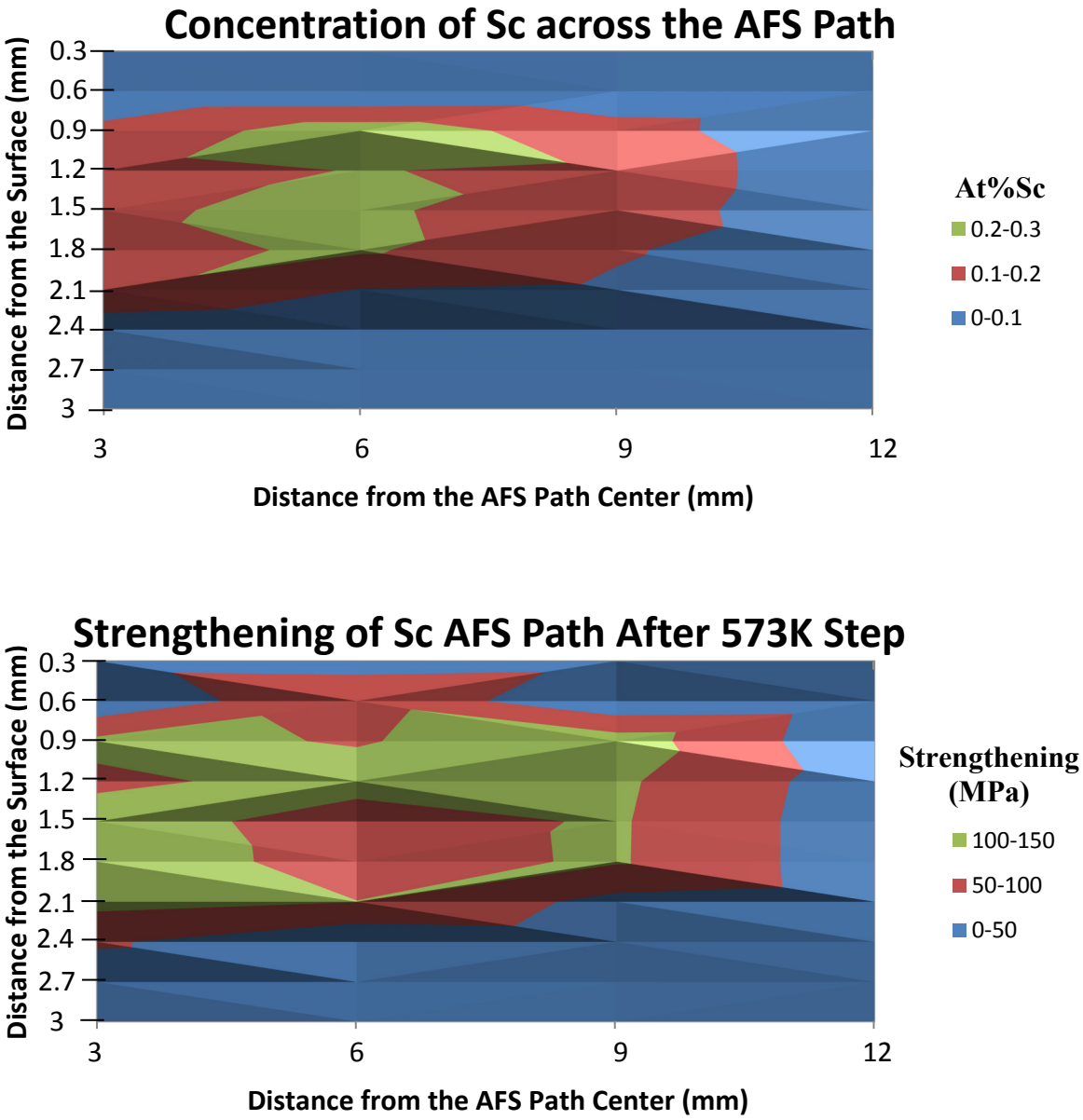

Figure 5.4: These images demonstrate how the concentration and strength (as determined with Vickers hardness testing after stepped heat treatment to 573K) vary with physical location in a cross section of the AFS path. The left of each image is in the center of the path, as shown in Figure 5.2.

Another method of looking at this data is to ignore testing location data and look instead at the paired hardness and compositions of a single heat treatment step or by holding the composition steady. Looking at only the data pairs of a single heat treatment step can aid in alloy development by demonstrating how small changes in Sc concentration can affect the strength of an alloy after a given heat treatment. In simple alloy systems this may be of negligible importance due to the ease of prediction of the results with strengthening mechanism equations, but this can be a real asset in more complicated systems. An example of this approach is shown as Figure 5.5, comparing the strengthening of different Sc concentrations in the as-received sample as well as in a sample that had been processed through the 573K (300˚C) step of the stepped heat treatment.

Figure 5.5 demonstrates difference in strengthening that is brought about by progressing through the stepped heat treatment steps. With this comparison (and the comparison of results of other steps to the as-received sample), it becomes clear that the variation of strengthening for a given concentration in the samples increases significantly after the heat treatments are performed. This is intuitive, as the strengthening effect of Sc was significantly less pronounced in the as-received state before precipitation; After precipitation occurred, areas that were slightly mislabeled would strengthen considerably more/less and become apparent.

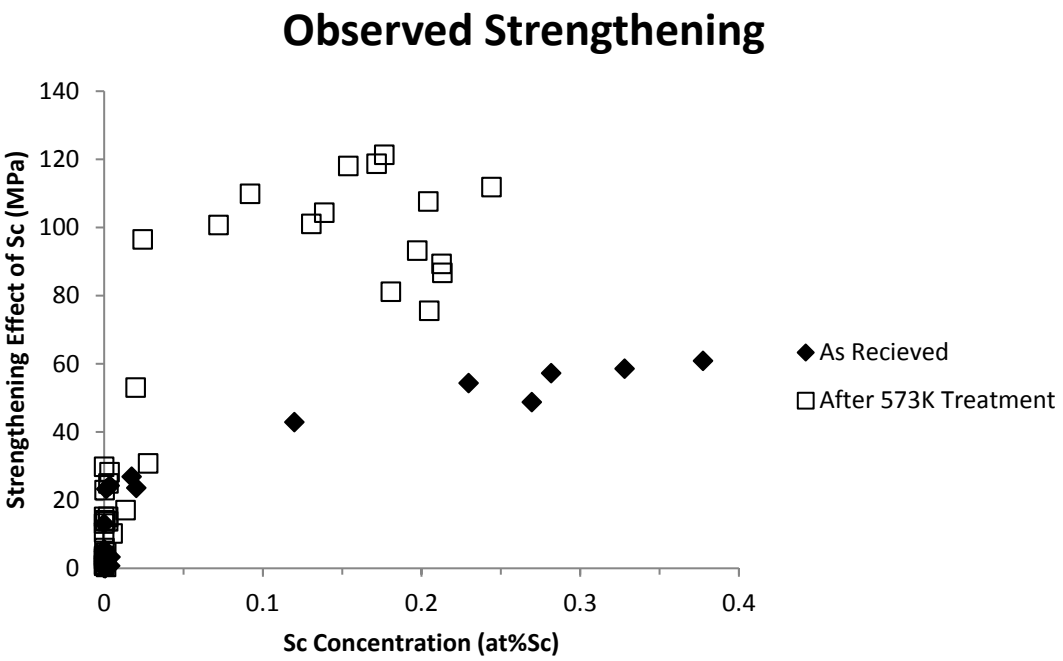

Figure 5.5: This graph shows the relationships between Sc concentration and the strengthening effect at two different stages of the stepped heat treatment (as-received and after the 573k Step).

Holding the composition steady at a value within the observed range demonstrates how the hardness would be expected to change in a homogenous sample of the chosen composition when exposed to a similar heat treatment. This prediction has been observed to agree with simulations and with data from literature for lower Sc concentrations, but the observed strength falls short of literature and simulation values for the data pairs indicating higher Sc concentration, as demonstrated in Figure 5.6. This observed under-strengthening is likely because the high temperatures (Figure 5.7) and lattice distortion seen during the AFS process were enough to nucleate/grow precipitates and deplete the rapid-solidification-obtained supersaturation down to near equilibrium concentrations.

The deviation from expected strength at higher Sc concentrations than Al-0.06at%Sc appears to indicate that the actual Sc saturation concentrations after the AFS process are little more than 0.06at%Sc. The unaccounted-for Sc is likely permanently locked in precipitates too large to meaningfully contribute to the strength, as these alloys contain too much Sc to allow the full solutionizing of Sc in the solid state.

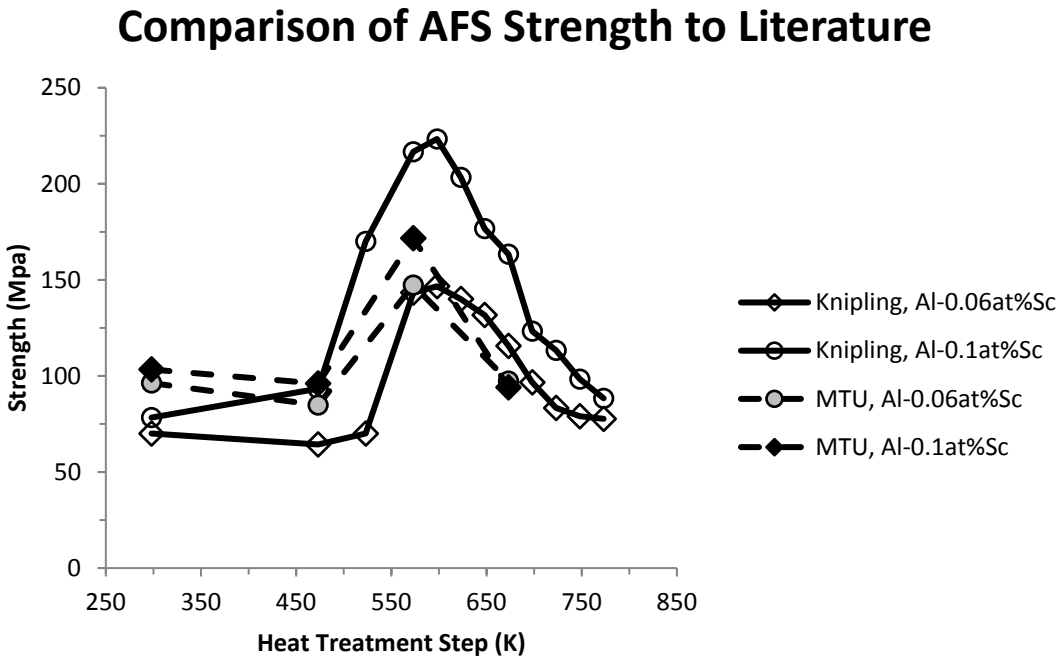

Figure 5.6: This image compares the results of these AFS experiments with experiments performed in literature using identical Sc concentrations and stepped heat treatments on bulk alloys. While the Al-0.06at%Sc samples (both Knipling's and those of this experiment) were similar in strengthening effects, the 0.1at%Sc results for this experiment fell short of the literature values.

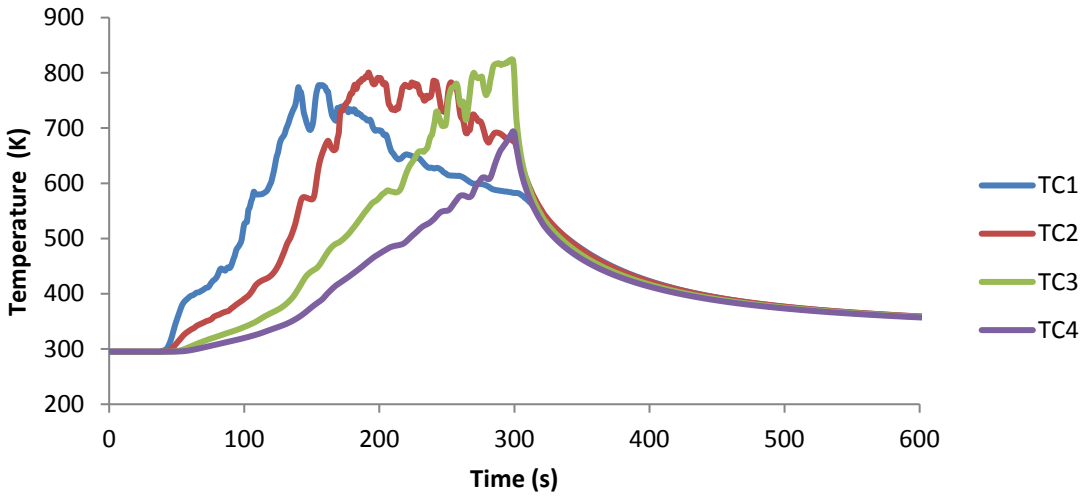

Figure 5.7: This graph shows the thermal profiles recorded by four thermocouples placed within the 99.99% Al substrate directly beneath the AFS path. The temperatures recorded, reaching peaks over 800K (523˚C), are high enough to cause considerable unwanted precipitate growth even over the short time scales.

The temperatures shown in Figure 5.7, as collected from thermocouples inside the Al substrate, are sufficient to grow/coarsen Al_3Sc precipitate phase. It was known that elevated temperatures would be reached during the processing, but the extent of the temperature required was not originally known. At the peak observed temperature of 816K (543°C), the solvus concentration for Sc solubility in Al is reported as approximately 0.067at%Sc, so it is currently unclear whether the retained supersaturation was a result of near equilibrium phase fractions at peak temperature or of incomplete matrix depletion at lower temperatures due to kinetics. While success in keeping the temperature lower than this was not achieved in the course of these experiments, there is

no indication that this is the minimum possible temperature at which this process can be performed. With knowledge that some amount of supersaturation can be maintained through the AFS process, and the reasonable assumption that the processing temperature can be reduced, future work should be performed to attempt this with more aggressive active cooling of the substrate.

5.6 Conclusion

In this chapter, a method for creating a thermally stable Sc-rich layer on the surface of an Al substrate was described, and the resulting experiments were analyzed. The Sc distribution along the Additive Friction Stir (AFS) path itself was slightly unpredictable in nature, which is believed to be due to inconsistencies in feedstock billet density, etc. Any industrialization of this prototype process should be able to create a more uniform Sc distribution. For the purposes of this analysis, focus was placed on analysis of the strengthening effect of Sc concentrations where available in the AFS path as opposed to the geometry and consistency of the path. Several different methods of representing the data were discussed, along with discussions of the scenarios that each method would benefit.

In low concentration areas of the sample (≤Al-0.06at%Sc), the analysis methods outlined in this work give an accurate assessment of the aging behavior of precipitates. While this analysis method offers a wealth of information about the AFS process and about a range of compositions of Al-Sc alloys, it is clear that the process fails to achieve the full potential of strengthening for Al-Sc alloys in areas with higher concentration. This is

believed to be due to precipitate nucleation and growth during processing, which was briefly observed to reach temperatures upwards of 800K (523˚C). This precipitation behavior lowered the Sc saturation concentration from that initially achieved with rapid solidification to near equilibrium levels. Therefore in areas of high Sc concentration, the majority of Sc has negligible contributions to strengthening because it is tied up in precipitates that are far larger than the optimal 1-3nm radius size. In alloys such as this, where the Sc matrix concentration is considerably higher than the solvus concentration and Sc was only coaxed into solid solution through the use of rapid solidification, overaged Al_3Sc precipitates will have no opportunity to be homogenized. Any attempt to gain higher strengths for this material will require a complete melting and repetition of this process, which will in turn add unwanted impurities to the melt.

While much of the extended supersaturation from the melt spun feedstock did not survive the transfer into the bulk Al substrate, it is promising that any supersaturation survived at all. With further studies into this process, it is feasible that improvements in processing parameters and active cooling could increase the Sc solution concentrations which are transferred to the substrate (still in solution), which would in turn allow for an increase in achievable strengthening effect for this method.

Chapter 6: Designing Heat Treatments for Al-Sc Alloys with the Kampmann and Wagner Numerical Model

6.1 Abstract

In this chapter, an adaptation of the Kampmann and Wagner Numerical model was developed as a Matlab program to predict precipitation and growth of Al_3Sc precipitate phase given varying starting concentration, heat treatment steps, etc. This model was then further developed to predict the strengthening effects that would be present in an alloy with the calculated average precipitate number density, radius, etc. Calibration of this model was achieved with Bayesian Optimization thanks to a collaboration with researchers at Deakin University, and the model was then verified against experimentally gathered hardness data as well as literature. An analysis of the large amount of data outputs from this code allowed for the development of long heat treatments, which were validated experimentally and proved to result in higher final strengths than previously observed. Bayesian Optimization was also used to predict optimal heat treatment temperatures in the case of limited heat treatment times.

6.2 Predictive Model Design and Function

6.2.1 Purpose of this Modeling

Al-Sc and Al-Zr precipitation strengthening alloys have been proven in literature to have excellent coarsening resistance and conductivity when compared to more traditional precipitation strengthening alloys, due in large part to the low diffusion rates and low solubility limits of these elements in aluminum, respectively [7][29][46]. However, due to the scarcity and expense of these elements, little work has as yet been done to determine optimal heat treatments for different compositions. This research is intended to accurately predict the precipitate nucleation and growth of Al_3X precipitates in an attempt to estimate optimal heat treatment schedules for peak strengthening.

6.2.2 Basic Structure and Theory of this Modeling

To accomplish this goal, an adaptation of Kampmann and Wagner's numerical precipitation model (heretofore referred to as the KWN model) has been developed to closely approximate experimental conditions reported for work done in house as well as found in literature [16]. The KWN model tracks precipitate nucleation, growth, coarsening, and dissolution over a series of discrete timesteps by iteratively solving classical nucleation theory and Gibbs-Thomson relationship equations. Precipitates formed are grouped into bins of similar radii and are allowed to grow or dissolve as is determined by their size in the equations at each timestep [47][48][49].

The model, in the form of a Matlab program, can be separated into several distinct sections, namely (A) initial material and process specific inputs, (B) an outer loop that iterates for each heat treatment temperature, (C) an inner loop that iterates through the time of each heat treatment step and calculates precipitate nucleation behavior at each timestep, and (D) the innermost loop that adjusts the precipitate radii formed in previous timesteps according to the Gibbs-Thomson relationship. After all nucleations and precipitate growth/dissolutions are calculated for a given timestep, the solute concentration is adjusted to reflect all solute atoms lost to or gained from precipitates.

A) Inputs

In the first section, all of the process and material specific inputs are defined, and constants related to these values are calculated. Process specific inputs include the number, temperature, and length of heat treatment steps, as well as the initial solute concentration of the alloy in question. Material specific inputs include the diffusion coefficient of the solute atoms in the matrix (D_0), the vacancy formation and migration energies of the solute atoms (E_f^{v-X} and E_m^v), lattice parameters of the matrix and precipitate phase (a_m and a_p), Poisson's ratio of the matrix and precipitate phase (v_m and v_p), and shear modulus of the matrix and the precipitate phase (G_m^{shear} and G_p^{shear}).

B) Temperature Loop

Following the input section, a loop is entered to calculate temperature dependent values for the first heat treatment step. This loop repeats whenever the simulated time reaches

the end of the current heat treatment step and the temperature is raised or lowered to the next listed heat treatment temperature.

The first main set of equations analyzed at the onset of each new temperature concern the calculation of the solvus line defining the solubility of the solute atoms in the matrix. As the temperature increases, so does the solubility, and this can be the cause of a significant amount of precipitate dissolution at the beginning of a relatively high heat treatment step. The composition of the solvus line was found at each temperature using Gibbs free energy curve data found in literature[4].

The second main temperature dependent aspect of the program concerns the calculation of the diffusivity, as seen in Eqn 6.1 [34], where D_0 is the diffusion coefficient, f is the dimensionless correlation factor (0.7815 for FCC materials), E_f^{v-X} is the vacancy formation energy near an impurity atom X, and E_m^v is the impurity migration energy mediated by a vacancy[50]. As the temperature increases, the diffusion rates of solute atoms increase, quickening the kinetics of nucleation and growth.

$$D = D_0 f exp\left(\frac{-E_f^{v-X} - E_m^v}{k_B T}\right) \qquad \text{Eqn 6.1}$$

C) Timestep Loop

Within the outer temperature loop, there is a large loop that iterates for each timestep. This loop holds all of the equations that are dependent on time and solute concentration,

including all of the nucleation and growth equations. At each timestep, the critical radius and nucleation rate are calculated based on the solute concentration at the beginning of the step. Another loop (discussed in the next section) is then entered to grow/dissolve precipitates made in previous steps, and then the solute concentration is updated taking into account all solute loss or gain from the precipitates. At the end of each timestep, the average precipitate radius and corresponding strength prediction is recorded.

In order to determine the critical radius, it is important to know the changes in Gibbs free energy associated with creating new precipitate volume (ΔG_v) as well as creating more matrix-precipitate interfacial area (ΔG_s). Equations 6.2 and 6.3 demonstrate the main equations used to determine these values, with $\Delta G_{Al_3X}^{formation}$ being the Gibbs energy of formation of Al_3X, $G_{matrix}^{Al_3X}$ being the intercept at 25%X of a line tangential to the matrix phase Gibbs energy curve at the current matrix composition [51], ε is the misfit strain between the two phases, $G_{m\ or\ p}^{shear}$ is the shear modulus of the noted phase (m=matrix, p=precipitate), and $v_{m\ or\ p}$ is the Poisson's ratio of the noted phase.[48]

$$\Delta G_v = \frac{\Delta G_{Al_3X}^{formation} - G_{matrix}^{Al_3X}}{V_{mol}} \qquad \text{Eqn 6.2}$$

$$\Delta G_s = \frac{3\varepsilon^2 G_p^{shear}(1+v_p)}{(1-2v_p)}\left[1 - \frac{\left(1+\frac{3G_m^{shear}(1+v_m)(1-v_m)}{(1-2v_m)}\right)^{-1}(1-2v_p)}{G_p^{shear}(1+v_p)(1+v_m)} - \frac{G_m^{shear}(1+v_m)(1-2v_p)}{G_p^{shear}(1+v_p)(1-2v_m)}\right] \qquad \text{Eqn 6.3}$$

Because the $L1_2$ precipitates in these systems are relevant for strengthening at just 1-2nm, it is important to note that the interfacial energy of the precipitate changes based on the

precipitate radius. This is because at its smallest radii only the most favorable (lowest energy) interfacial planes are used due to the small number of unit cells involved. As the precipitate grows and incorporates more unit cells it is able to more closely approximate a sphere; this rounding out results in the use of less favorable interfacial planes and an increase in interfacial energy. While differences in interfacial energy for Al_3Sc precipitates have been clearly observed, no clear analysis on the transition has been undertaken. Instead, it has been suggested in literature that a linear increase from the smallest to the largest interfacial energy over the course of the first several nanometers in radius (as demonstrated in Eqn 6.4) is sufficient to approximate nucleation and growth trends [49]. In this model, precipitates with radii smaller than 5nm were made to have size dependent interfacial energies, while larger precipitates will have the maximum interfacial energy as observed in literature.

$$\gamma = \gamma_{slope\ constant} r_{less\ than\ 5\ nm} + \gamma_{initial} \qquad \text{Eqn 6.4}$$

This further complicates matters as the calculation for the critical radius of nucleation depends on the interfacial energy (Eqn 6.5). Solving for these equations if the critical radius is less than 5 nm yields Eqn 6.6.

$$r^* = \frac{-2\gamma}{\Delta G_v + \Delta G_s} \qquad \text{Eqn 6.5}$$

$$r^*_{less\ than\ 5\ nm} = \frac{-2\gamma_{initial}}{\Delta G_v + \Delta G_s + 2\gamma_{slope\ constant}} \qquad \text{Eqn 6.6}$$

The nucleation rate, I, is calculated through the use of equations 6.7-6.11, where V_a is the average volume of an atom in the matrix, c is the atomic fraction of solute atoms in the matrix, Z is the Zeldovich factor, β^* is the atomic impingement rate, τ is the incubation time for nucleation, and N_v is the number of nucleation sites per cubic meter (assumed to be the number of solute atoms per cubic meter for homogenous nucleation) [47].

$$V_a = 4ca_p^3 + (1-4c)a_m^3 \qquad \text{Eqn 6.7}$$

$$Z = \frac{V_a \Delta G_v^2}{8\pi\sqrt{kT\gamma^3_{critical\,radius}}} \qquad \text{Eqn 6.8}$$

$$\beta^* = \frac{16\pi cD\gamma^2_{critical\,radius}}{\Delta G_v^2 a_p^4} \qquad \text{Eqn 6.9}$$

$$\tau = \frac{8kTa^4_{p\,critical\,radius}}{V_a^2 \Delta G_v^2 Dc} \qquad \text{Eqn 6.10}$$

$$I = N_v Z\beta^* exp\left[\frac{-4\pi\gamma r^{*2}}{3kT}\right] \exp\left[\frac{-\tau}{t}\right] \qquad \text{Eqn 6.11}$$

At this point in the loop, another loop (the Historical Timestep Loop described more completely in section D) iterates to grow/dissolve precipitates formed at previous timesteps. After the completion of said loop, the number of solute atoms in precipitates is subtracted from the initial number of solute atoms in the alloy, and the new matrix composition is calculated. The average radius and number of precipitates is also calculated at this point to be used in calculating the precipitate strengthening.

For $L1_2$ precipitates such as those found in Al-Sc and Al-Zr alloys, the predominant strengthening mechanism at small precipitate size (<3nm) is order strengthening, which is

described in Eqn 6.12. As the average precipitate radius increases over a certain threshold, Orowan strengthening (Eqn 6.13) gains dominance and and the strength of each precipitate begins to decrease. By analyzing each of these equations at the end of every timestep, it is possible to create a predictive aging curve describing likely strengthening behavior. In these equations, M is the Taylor mean orientation factor, γ_{APB} is the precipitate antiphase boundary energy, b is the Burgers vector of the matrix, f is the phase fraction of precipitates, $\bar{R}$ is the average precipitate radius, and λ_{e-e} is the edge-to-edge interprecipitate spacing [16][19][20].

$$\sigma_{ord} = 0.44MG_p^{shear}\frac{\gamma_{APB}}{b}f^{1/2} \qquad \text{Eqn 6.12}$$

$$\sigma_{or} = \frac{0.4MG_m^{shear}b*\ln\left(\frac{2\bar{R}}{b}\right)}{\pi\lambda_{e-e}\sqrt{1-v_m}} \qquad \text{Eqn 6.13}$$

D) Historical Timestep Loop

Within the loop for each timestep, an innermost loop is nested to keep track of any precipitate growth or dissolution that occurs due to solute concentration changes and the Gibbs-Thomson relationship. Because it is known how many precipitates of what size were nucleated at each timestep, each historic timestep is iterated to adjust the radius and solute atom content of precipitates formed at that step. The calculations compete with each other for resources (solute atoms), and, as the matrix is depleted of excess solute atoms, a near equilibrium concentration is reached. At this concentration, solute atoms are entering precipitates from the matrix at approximately the same rate as they are leaving them. However, the solute gain/loss ratio of larger precipitates is larger than that

of smaller precipitates due to interfacial energy. This results in the larger precipitates slowly increasing in size as the smaller ones dissolve back into the matrix.

Precipitate growth in this model is governed by Eqn 6.14, where c_r^m is the equilibrium concentration in the matrix immediately adjacent to a precipitate and c_e^p is the equilibrium concentration of the precipitate. The Gibbs-Thomson equation works on the principle that the equilibrium composition in the matrix immediately adjacent to a precipitate (c_r^m) is effected by the interfacial energy of the precipitate. This effect is described by Eqn 6.15, where c_∞^m is the equilibrium composition at a planar interface[52].

$$\frac{dR}{dt} = \frac{D}{R}\frac{c - c_r^m}{c_e^p - c_r^m} \qquad \text{Eqn 6.14}$$

$$c_r^m = c_\infty^m exp\left(\frac{2\gamma V_m}{R_{gas\ constant} TR}\right) \qquad \text{Eqn 6.15}$$

E) Outputs

Because of the flexibility afforded by simulating with Matlab, all inputs, variables, and counters used and/or generated throughout a simulation can be output into Excel. Potentially useful outputs for understanding the precipitation behavior include but are not limited to: time, temperature, matrix concentration, nucleation rate, precipitate number density, average radius, and the various relevant strengthening mechanisms. The shear amount of information known about each simulation becomes difficult to display in a scientific work such as this, so not all outputs that are discussed in this work will be accompanied by a figure.

6.2.3 Special Considerations

This model also takes into account several special considerations due to the circumstances being modeled. For example, in the Al-Sc system the critical radius is often calculated as being smaller than one unit cell of the precipitate. Since the matrix and precipitate unit cells (FCC Al and $L1_2$ Al_3Sc) only differ in the substitution of a single Sc atom, there is no differentiation between a single Al_3Sc unit cell and a unit cell of the matrix with a substitutional Sc atom. Therefore the critical radius was limited to never describe a precipitate smaller than two unit cells.

Another consideration taken into account is that silicon content can increase the kinetics of certain systems, including the Al-Sc system. Si atoms have relatively more favorable bonding with vacancies than Sc atoms. Because Si atoms also tend to cluster with Sc atoms in the Al matrix, the Sc atoms benefit from an easier access to vacancies resulting in an apparent decrease in migration energy (and in turn an increased diffusion rate). This can have a significant effect on the precipitation behavior [34].

Another thing that can be adjusted is the initial incubation state. Classical nucleation theory includes an incubation time term, which describes the period of time required to rearrange homogenously distributed solute atoms into solute clusters [47]. In this model it is possible to start the first timestep with the incubation time partially completed, indicating that some clustering has already begun due to room temperature diffusion or diffusion during initial cooling.

6.2.4 Future KWN Modeling Work

A version of the model which looks at alloys with more than two component elements is currently in progress in this research. Although it is not currently finished, Appendix A.3 contains intact portions of the expanded model code, with annotations describing the general approach.

6.2.5 KWN Modeling Summary

With the proper application of known kinetics, thermodynamics, and strengthening equations, it is possible to create a model to approximately simulate strengthening by precipitation in alloys computationally. The model will require correlation to real experimental data in order to give meaningful results due to the complexity of the simulation, but there are ample inputs that can be adjusted to finetune the result.

6.2.6 Bayesian Optimization

Fitting and optimization of the KWN model described in this chapter were performed with Bayesian Optimization through a collaboration with Deakin University. Assuming the process being optimized can be defined by an unknown, continuous objective function, the Bayesian Optimization process uses initially limited data points from the process to adjust an approximating surrogate function. As the shape of the surrogate function is defined, an acquisition function determines what parameter settings the next test should use to have the greatest chance of reaching a greater value than previous points. In order to suggest useful points, such an acquisition function considers areas of

the surrogate function which are very uncertain (exploration), as well as areas where the objective function is thought to be high (exploitation).

The primary form for the surrogate function is that of the Gaussian process. A Gaussian process (GP) is similar to a standard function, except that each point along the function is replaced by Gaussian distribution information for that point (the mean and covariance of that point). A simple example of how GP is used to describe Bayesian Optimization surrogate functions is shown in Figure 6.1. With experimental knowledge of several points along the function, sections of the function near to those points have relatively small ranges of probable values, whereas areas that are far from previously sampled points will have more variance and therefore potentially higher sampled values. It is also important to note that areas with high variance are not alone in the potential to have local maxima; locations where the variance is small and the means are expected to be high frequently exist as maxima are narrowed in on (exploitation).

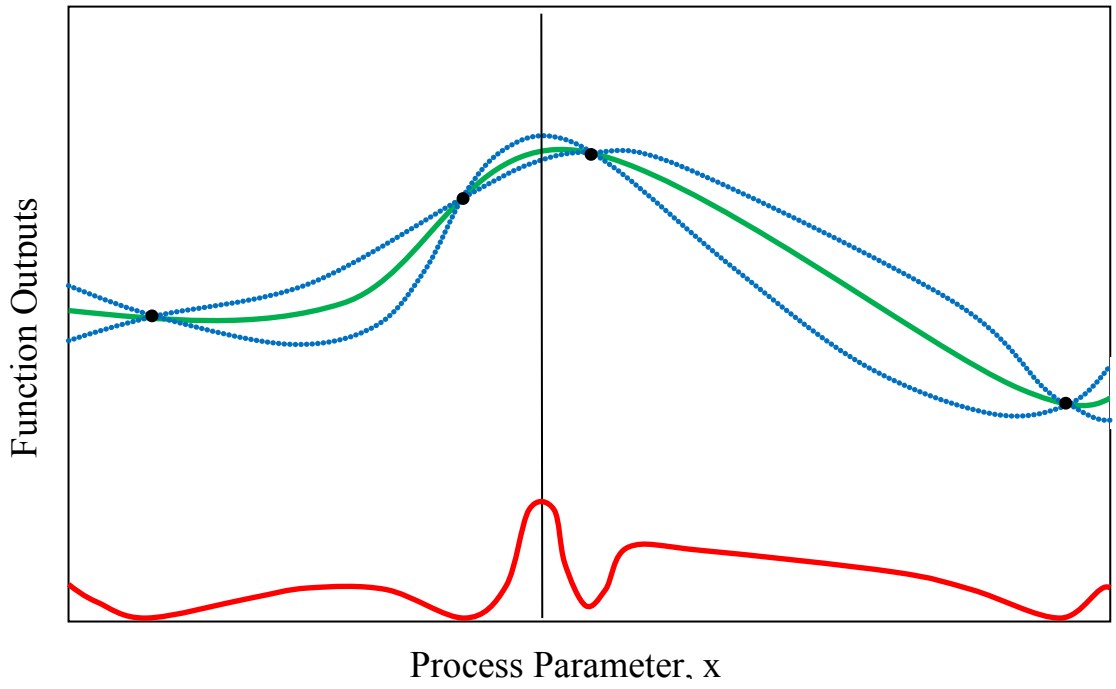

Figure 6.1: This image is a representation of a simplified (1 dimensional) Gaussian Process, where several points are defined due to experimental testing of the relevant process. The blue and green lines represent the uncertainty and predicted mean values of the objective function, respectively. The red line represents the acquisition function, and the vertical black line denotes where the next experimental point is requested.

In this work, Bayesian Optimization was first used to minimize the root-mean-square error between precipitate strengthening observed experimentally for specific 2-step heat treatments and precipitate strengthening predicted using the KWN model. To achieve a better fit, precipitate-matrix interfacial energy values at nucleation and at r=5nm were adjusted. Such interfacial values have been determined multiple times in literature, but

there is little agreement other than an acknowledgement that the interfacial energy for Al_3Sc decreases at very small precipitate size due to preferential formation of interfaces along the lowest energy planes (100). The 2-step heat treatments were chosen at the low end of temperatures where Sc is mobile in Al, in an attempt to make the heat treating predictions more accurate. Once the KWN model was properly fitted and verified, Bayesian Optimization was used to maximize the strengthening results over heat treatments of a limited time by changing the heat treatment temperature and time within the simulations. These simulation results were then experimentally tested.

6.3 Experimental Verification Setup

In order to calibrate and verify the accuracy of the simulation, it was necessary to perform occasional experimental trials mimicking the heat treatments that were simulated in the model. For these trials, sample charges weighing 600g in total were cut (Section 3.11) and assembled (Section 3.13) in the proper proportions to hit the target compositions as shown in Table 6.1. These charges were then cast into a permanent 4-bar mold using an onsite vacuum induction melter (VIM) as described in Section 3.14. During the pour, the sample was held at 1173K (900˚C) for 10 minutes under a 684 Torr atmosphere of ultra high purity argon. After casting, holes were drilled into the base of representative bars to create chips for compositional verification using ICP-OES (Section 3.5). For each alloy, a slice of approximately 1 cm thickness was then removed from the center of a bar using a cutoff wheel and mounted in QuickSet epoxy. The samples were

mounted to assist in the initial polishing, but also to create a larger surface to allow for adequate gripping during hardness testing. These mounted samples were then ground and polished to a 0.04 micron colloidal silica finish (Section 3.12). Once mounted, the samples were tested for hardness and conductivity to capture baseline conditions (Sections 3.7 and 3.8 respectively).

Table 6.1: Expected and Observed Alloy Compositions

	Target Composition (at%)		**ICP-OES Determined (at%)**	
Alloy	**Sc**	**Si**	**Sc**	**Si**
Al-0.04at%Sc	0.04		0.041	
Al-0.07at%Sc	0.07		0.068	

In order to perform heat treatment on the samples, the epoxy had to be removed before each treatment (and reapplied before the next hardness testing session) as discussed in Section 3.12. The samples were broken out of the epoxy mounts by crushing the epoxy in a bench-mounted vice, taking care not to squeeze the epoxy in such a direction as to deform the aluminum sample in the process. Once the sample was broken free, it was heat treated (Section 3.4) to match the relevant simulation parameters. After the proper time at temperature, the samples were taken out and immediately quenched to lock in their structure.

Due to the large number of heat treatments required in this study, a method was developed to minimize the need for grinding/polishing on samples that had already been initially polished. The key to this method was to limit the flow of epoxy under the sample while it was a liquid, by covering the bottom of the mounting cup with packaging tape (adhesive facing up) before inserting the sample, polished-side down. Once solidified, the tape and any remaining tape residue would be removed from the epoxy mounted sample, leaving the previously polished surface exposed. In this way, the sample can be alternated between epoxy mounted and un-mounted between multistep heat treatments steps.

6.4 Results and Discussion

6.4.1 Initial Calibration of the Model

In order to provide initial datasets for calibration of the model with Bayesian optimization, several two-step heat treatments were performed of Al-0.04at%Sc and Al-0.07at%Sc, varying both the time and temperature held at each step as described in Table 6.2. Upon running a Bayesian optimization routine to determine the best possible fit through the adjustment of surface energy variables, ideal values were found to be isurfen=0.096 and fsurfen=0.158 with a EM=0.63. These values are very similar to values retrieved from literature.

Table 6.2: Heat Treatment Parameters of Calibration Experiments

Sample	Alloy	Heat Treatment Step 1 (T_1)		Heat Treatment Step 2 (T_2)	
		Temperature (K)	Time (s)	Temperature (K)	Time (s)
1A	**Al-0.04at%Sc**	548	10800	598	10800
2A	**Al-0.04at%Sc**	548	10800	623	10800
3A	**Al-0.04at%Sc**	518	14400	608	14400
4A	**Al-0.04at%Sc**	521	14091	603	13971
1B	**Al-0.07at%Sc**	548	10800	598	10800
2B	**Al-0.07at%Sc**	548	10800	623	10800
3B	**Al-0.07at%Sc**	531	14400	623	7200
4B	**Al-0.07at%Sc**	525	14308	583	9171

A comparison of the observed vs model-predicted results for these heat treatments can be viewed in Figures 6.2 and 6.3. The optimized parameters appear to result in an acceptable fit to the experimental data. The fit to the experimental data is not perfect, as several of the results slightly overpredict or underpredict the experimentally observed strengthening effects (made most noticeable in Sample 3A). However, the lack of a preferential bias in either direction lends credibility to the assumption that experimental error is likely a contributing factor.

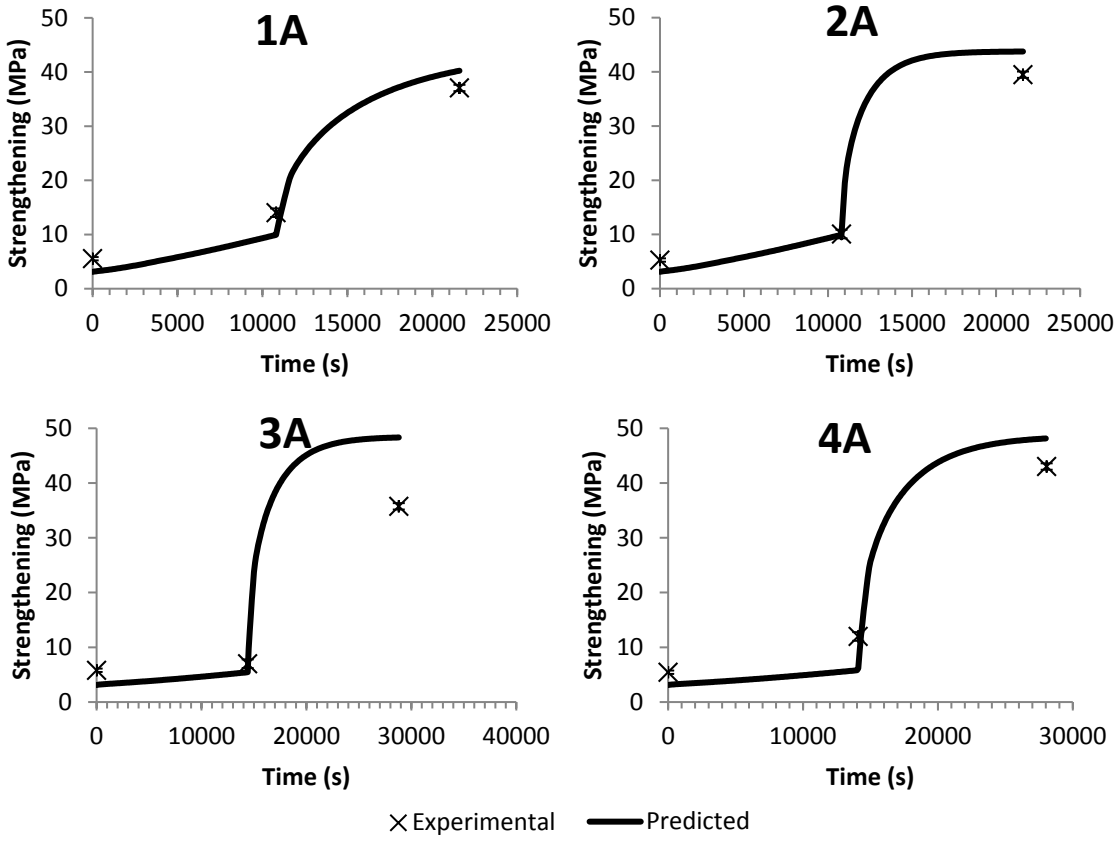

Figure 6.2: These graphs demonstrate the experimental results of several two-step heat treatments for Al-0.04at%Sc, as described in Table 6.2. The black line represents the predicted strengthening of the fitted model.

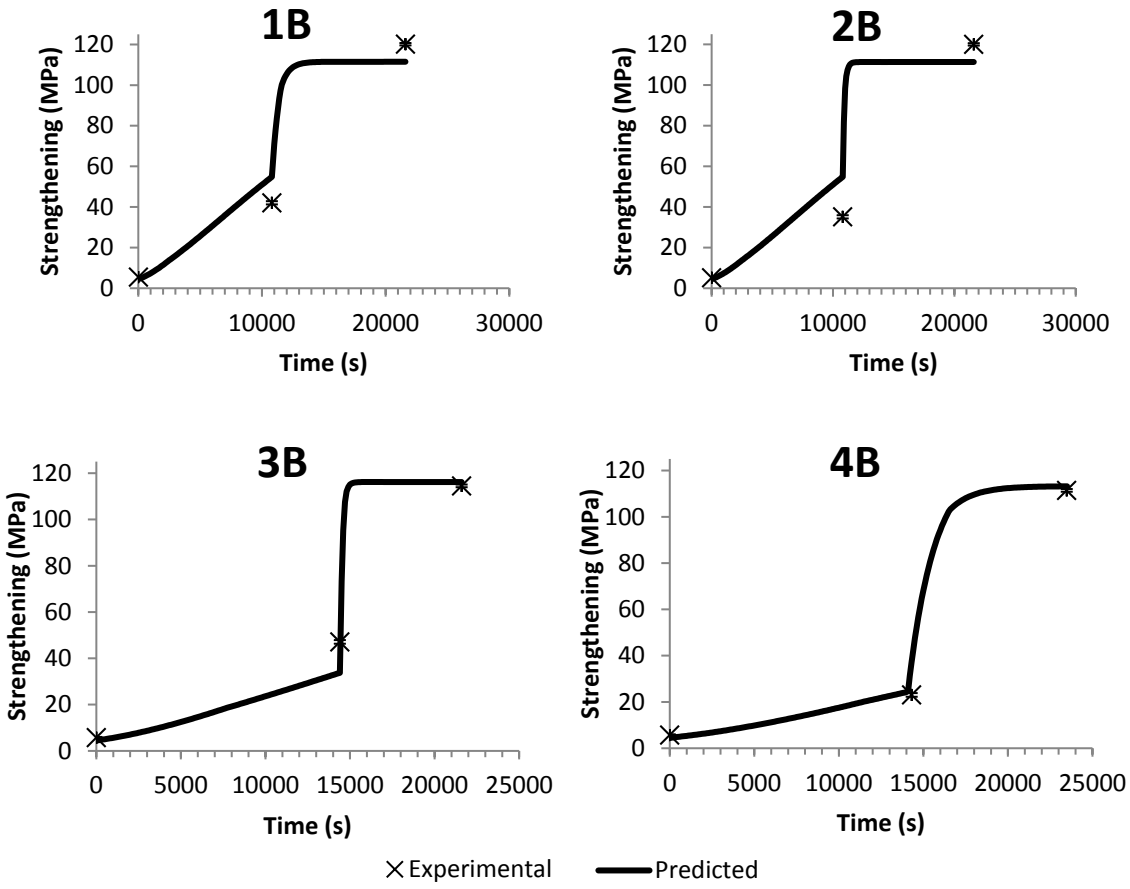

Figure 6.3: These graphs demonstrate the experimental results of several two-step heat treatments for Al-0.07at%Sc, as described in Table 6.2. The black line represents the predicted strengthening of the fitted model.

6.4.2 Testing Model against Multistep Heat Treatments

To further stress test the fitted calibration settings, experimental hardness results for multi-step heat treatments (described in Table 6.3) of the two Al-Sc alloys were compared to model predictions and are shown in Figure 6.4. These comparisons demonstrate a generally acceptable model fit, especially at the nucleating and aging

temperatures that this work is most concerned with, namely 523-573K (250-300˚C). These plots do indicate the existence of a slight underprediction of peak strengthening and a delay in coarsening at elevated temperatures, which is thought to be due to dendritic inhomogeneity in the alloy, which would create distinct regions where the average radius/strengthening effect behavior differ.

Table 6.3: Multistep Heat Treatment Temperatures and Times

Treatment Step	**1**	**2**	**3**	**4**	**5**	**6**	**7**	**8**	**9**	**10**	**11**
Temperature (K)	473	523	573	598	623	648	673	698	723	748	773
Step Time (Hr)	3	3	3	3	3	3	3	3	3	3	3
Total Time (Hr)	3	6	9	12	15	18	21	24	27	30	33

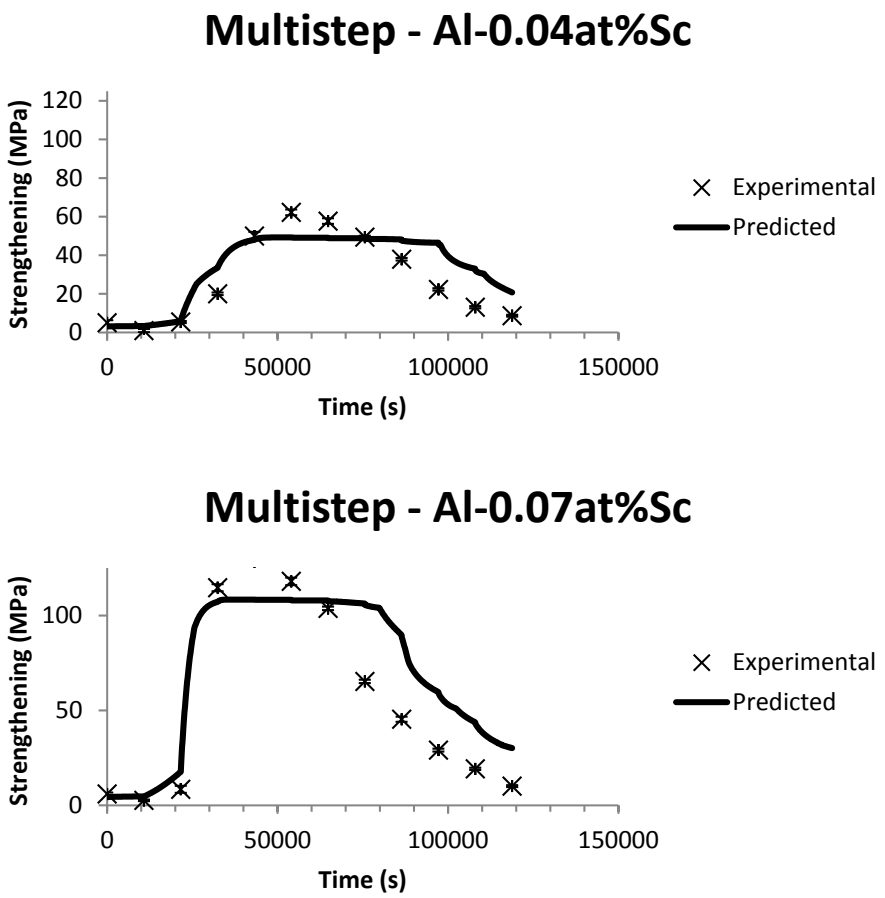

Figure 6.4: These graphs compare the experimentally observed and model predicted strengthening effects of Al-0.04at%Sc and Al-0.07at%Sc, through the course of a multistep heat treatment. The fit is better during earlier, low temperature heat treatment steps than during later ones, where a notable delay in aging is observed.

6.4.3 Analysis of Simulation Trends

For each simulation discussed in Section 6.3.2, there is an apparent plateau in strengthening observed in the second step, approximately 50 MPa for Al-0.04at%Sc and 120 MPa for Al-0.07at%Sc. By plotting relevant model variables for each simulation

(such as for sample 2A, shown in Figure 6.5), the cause of the plateau can be determined. In all of these simulations (1A-4B), a similar chain of events preceded the strengthening plateau:

1. During the first heat treatment step (T_1), nucleation rate and precipitate growth rate maintained a relatively constant order of magnitude. The matrix concentration declined only slightly due to these effects.
2. Immediately at the onset of the second step (T_2), the nucleation rate dropped several orders of magnitude, and the rate of precipitate growth increased significantly.
3. As the pre-existing precipitates grew throughout the second step, the matrix became depleted and approached the equilibrium solubility at T_2.
4. As the matrix approached equilibrium, the nucleation rate and precipitate growth rate decreased until nearly negligible.
5. As the precipitates were no longer changing significantly, all predicted strengthening mechanisms plateaued.

From the preceding events, it can be concluded that the range of T_1 temperatures used in these samples is sufficient mainly for nucleating Al_3Sc precipitates in supersaturated solutions while limiting precipitate growth. The range of T_2 temperatures is sufficient for growing Al_3Sc precipitates in supersaturated solutions, while limiting significant nucleation and limiting coarsening once the supersaturation is depleted.

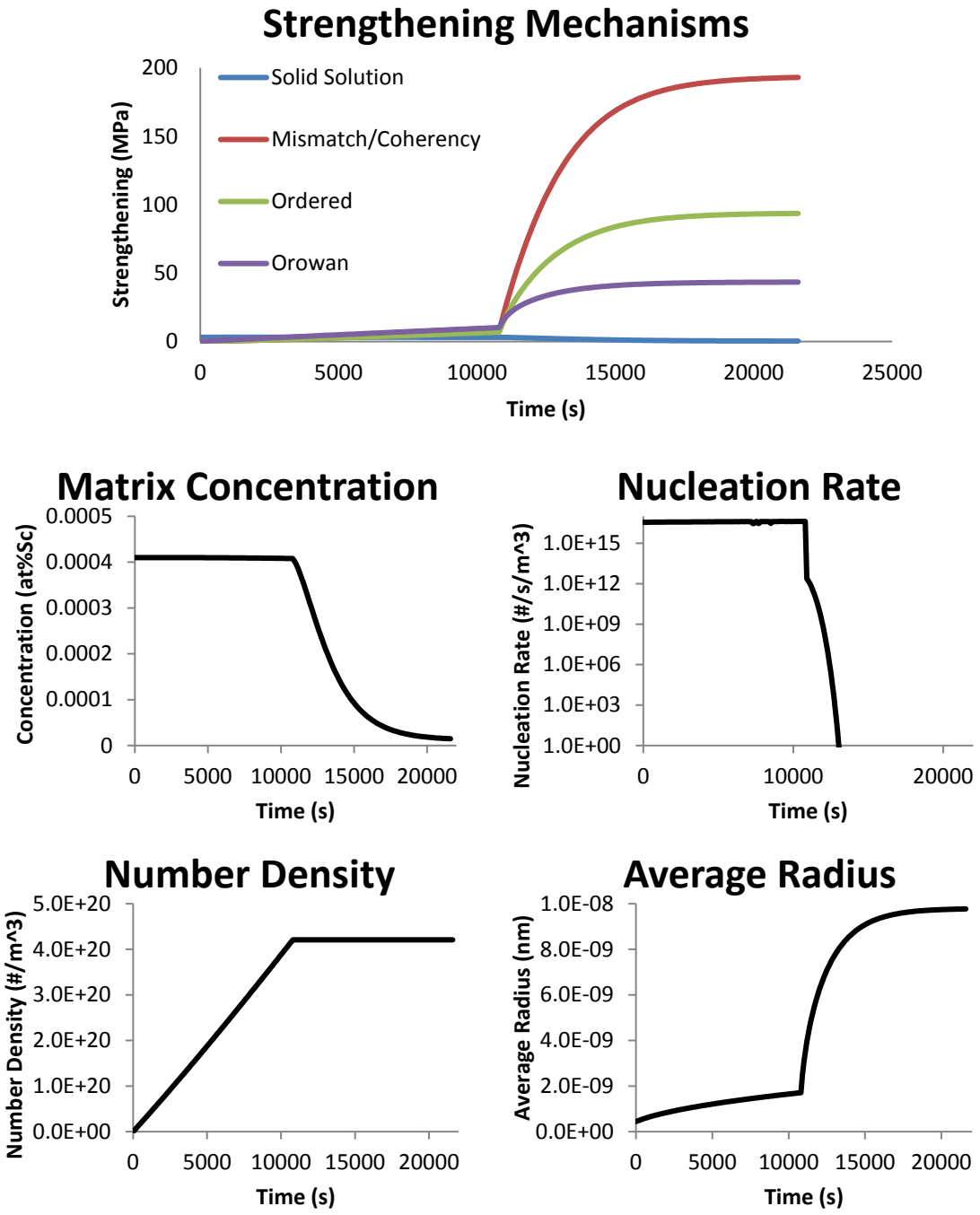

Figure 6.5: These graphs represent simulation outputs for Sample 2a, which is described in Table 6.2. Graphs such as these can be used to determine the cause of simulation strengthening trends, and assist in intelligent design of heat treatments.

It should also be noted that the average radius reached in sample 2A well exceeded the optimal target of 1-3nm, resulting in the unfortunate dominance of the Orowan strengthening mechanism. This was the case in all simulations (1A-4B), as well as the multi-step heat treatments. Throughout these tests, the difference in strengthening effect between predicted Orowan and Ordered mechanisms was consistently lower at the conclusion of the Al-0.07at%Sc simulations than in the Al-0.04at%Sc (~10 MPa versus ~50 MPa). This phenomenon can be linked directly to the consistently higher average precipitate radius predicted for Al-0.04at%Sc than for B, which can in turn be linked to a consistently smaller precipitate number density at the end of T_1 within these simulations. Adjustments of the heat treatments which successfully increase the number density of precipitates in a given alloy should in turn increase the strength.

Figure 6.6 shows simulation results for aging Al-0.4at%Sc for $1x10^6$ seconds at 523K (250˚C). Long heat treatment simulations were also run for Al-0.7at%Sc and at 548 and 573K (275 and 300˚C). These simulations suggest that holding at T_1 for significantly longer times than in 1a-4b results in enough depletion in the matrix to effectively negate the nucleation rate. It was also noted that changing the alloy composition and T_1 temperature affected the total possible number of precipitates, which should in turn affect the possible precipitate radius and strengthening.

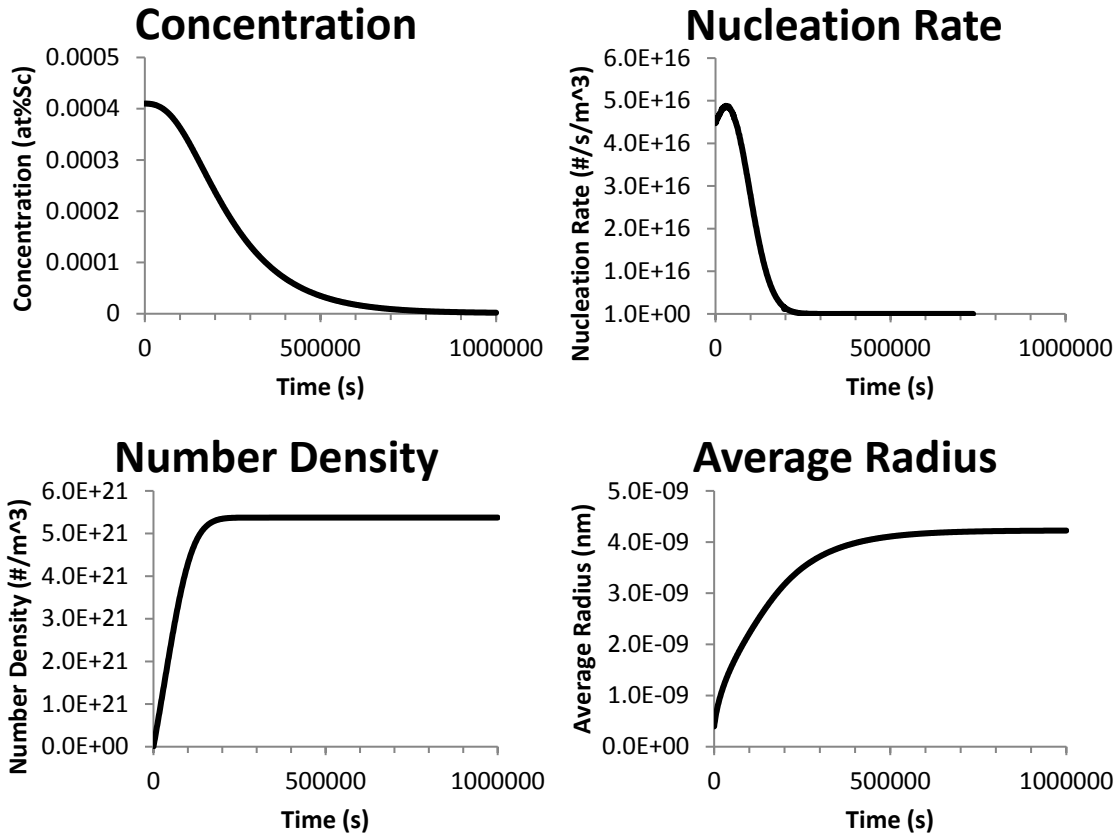

Figure 6.6: These graphs demonstrate simulation results for aging Al-0.4at%Sc for $1x10^6$ seconds at 523K (250˚C). Note that nucleation effectively halts as time progresses due to the depletion of the matrix.

Adjustments to the two step heat treatments to increase the final number density of precipitates in both alloys using knowledge of precipitate behavior gained from these simulations, primarily that temperatures of 523-548K (250-275˚C) are ideal for nucleating precipitates in supersaturated alloys without significant amounts of precipitate growth and that temperatures of 573-598K (300-325˚C) allow for rapid growth of precipitates with significantly lower nucleation rates. With the assumptions that the number of precipitates does not change after T_1 with a proper T_2 selection (as supported

by simulations), and that all remaining matrix supersaturation is depleted during T_2 through the growth of pre-existing precipitates, Eqns 6.16 and 6.17 predict what the final average radius would be if at any given time during T_1 the sample was switched to T_2. Figure 6.7 shows how the predicted average radius after sufficient T_2 varies by changing the time and temperature of the T_1 heat treatment step for Al-0.04at%Sc and Al-0.07at%Sc with T_1 varying between 523-573K (250-300˚C). As an example of how to read these graphs: heat treating Al-0.04at%Sc at T_1=548K for 10,000 seconds and then switching to T_2=573K until full matrix depletion should result in a final average radius of 10nm.

Eqn. 6.16

$$\left(\frac{\#Sc\ atoms}{precipitate}\right)_{after\ T_2} = \left(\frac{\#Sc\ atoms}{precipitate}\right)_{t,T_1} + \frac{\left(\frac{\#Sc\ solute\ atoms}{volume}\right)_{t,T_1} - \left(\frac{\#Sc\ solute\ atoms}{volume}\right)_{eq}}{\left(\frac{\#precipitates}{volume}\right)_{t,T_1}}$$

Eqn. 6.17

$$\hat{R}_{after\ T_2} = \left(\hat{R}_{t,T_1} + \frac{3}{4\pi} * \frac{a_{Al_3Sc}^3}{(\#Sc\ atoms)_{unit\ cell}} * \frac{\left(\frac{\#Sc\ solute\ atoms}{volume}\right)_{t,T_1} - \left(\frac{\#Sc\ solute\ atoms}{volume}\right)_{eq}}{\left(\frac{\#precipitates}{volume}\right)_{t,T_1}}\right)^{1/3}$$

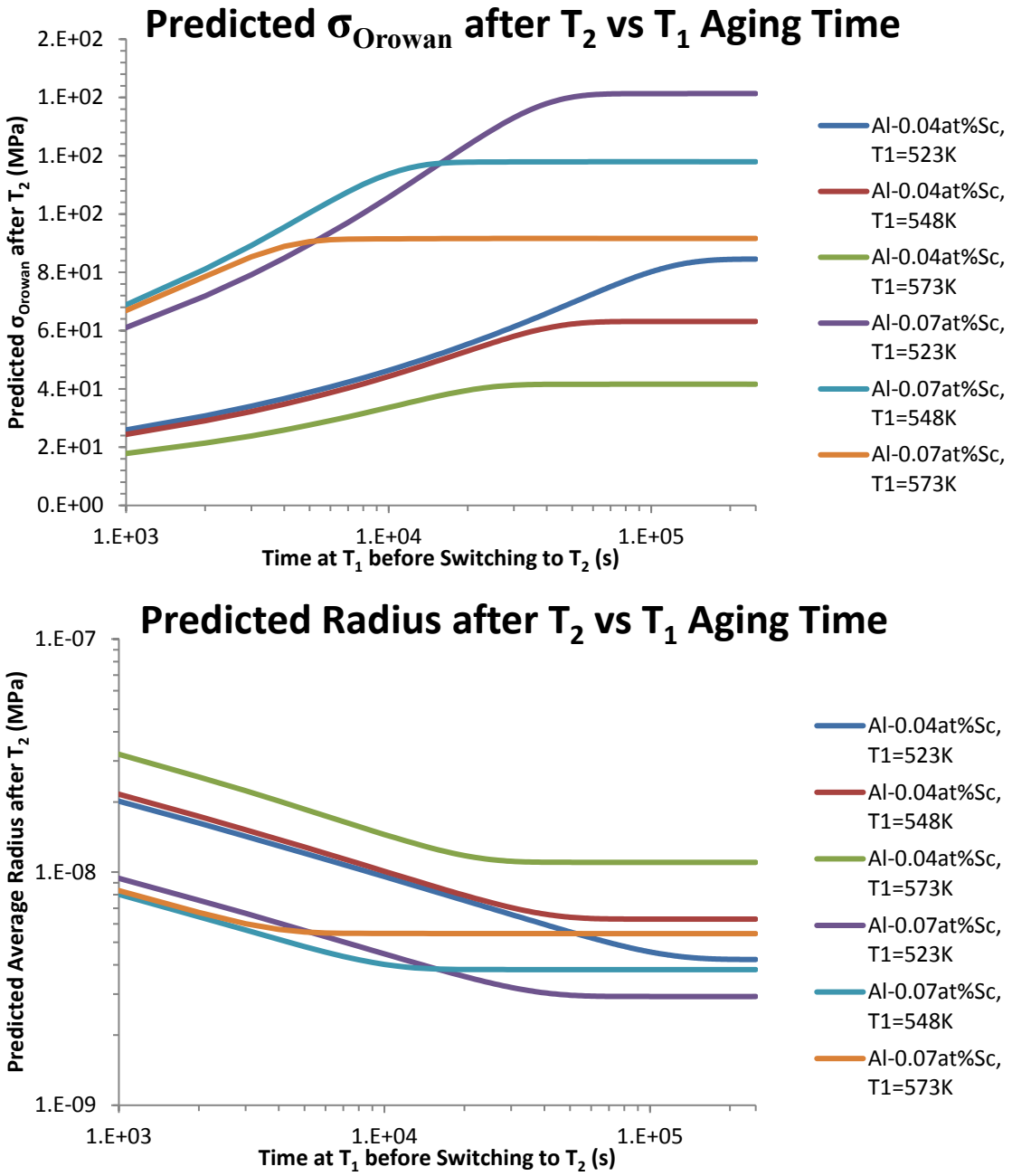

Figure 6.7: These graphs demonstrate how varying the time and temperature of the T1 step affect the predicted precipitate size and Orowan strengthening after heat treating at a sufficient T_2 step to completely deplete excess solute atoms in the matrix.

There are several notable trends in Figure 6.6 and 6.7, as discussed below:

- All long T_1 heat treatments eventually reach an equilibrium where nucleation stops. At this point, no amount of additional heat treating can continue to decrease the final radius, because the final average radius depends on the Sc atom to precipitate ratio. Ideal heat treatments should reach this equilibrium before moving to T_2.

- When heat treated at the same T_1 until matrix depletion, Al-0.04at%Sc will always result in larger average precipitates than Al-0.07at%Sc, as fewer precipitates can nucleate in alloys with lower concentration. Ideal heat treatments of alloys with varying Sc content should be scaled to take this into account.

- Heat treating at the lowest T_1 of 523K (250˚C) requires more time than 548 or 573K (275 or 300˚C), but it yields the highest strength. This is because, while nucleation rates are similar between the three temperatures, considerably more precipitate growth occurs in the higher two temperatures. This results in larger precipitates at the end of T_1 and in the more rapid depletion of the matrix. This rapid depletion quickens the decline of the nucleation rate, limiting the final number of precipitates. Ideal heat treatments should be performed at 523K (250˚C) for sufficiently long times.

- Between these two alloys, only Al-0.07at%Sc at 523K (250˚C) achieved the target average radius and therefore the maximum potential strengthening associated with the Ordered strengthening mechanism. Ideal Al-Sc alloys for heat treating should be of a similar or higher Sc concentration to Al-0.07at%Sc, and therefore be able to achieve the maximum potential strengthening.

To verify these results, several long T_1 simulations and experimental heat treatments were performed as seen in Figure 6.8. Hardness testing was performed on the experimental samples and resulted in calculated precipitate strengthening approximately equal to the predicted strengthening of the model. This supports the hypothesis that increasing the number density of precipitates with a significantly longer T1 step results in a decrease in average precipitate radius upon the depletion of the matrix. These results also demonstrate that a substantial heat treatment time savings can be achieved through the use of a second heat treatment step at a slightly higher temperature, in this case 573K (300˚C), to allow for the rapid depletion of the matrix without significant coarsening.

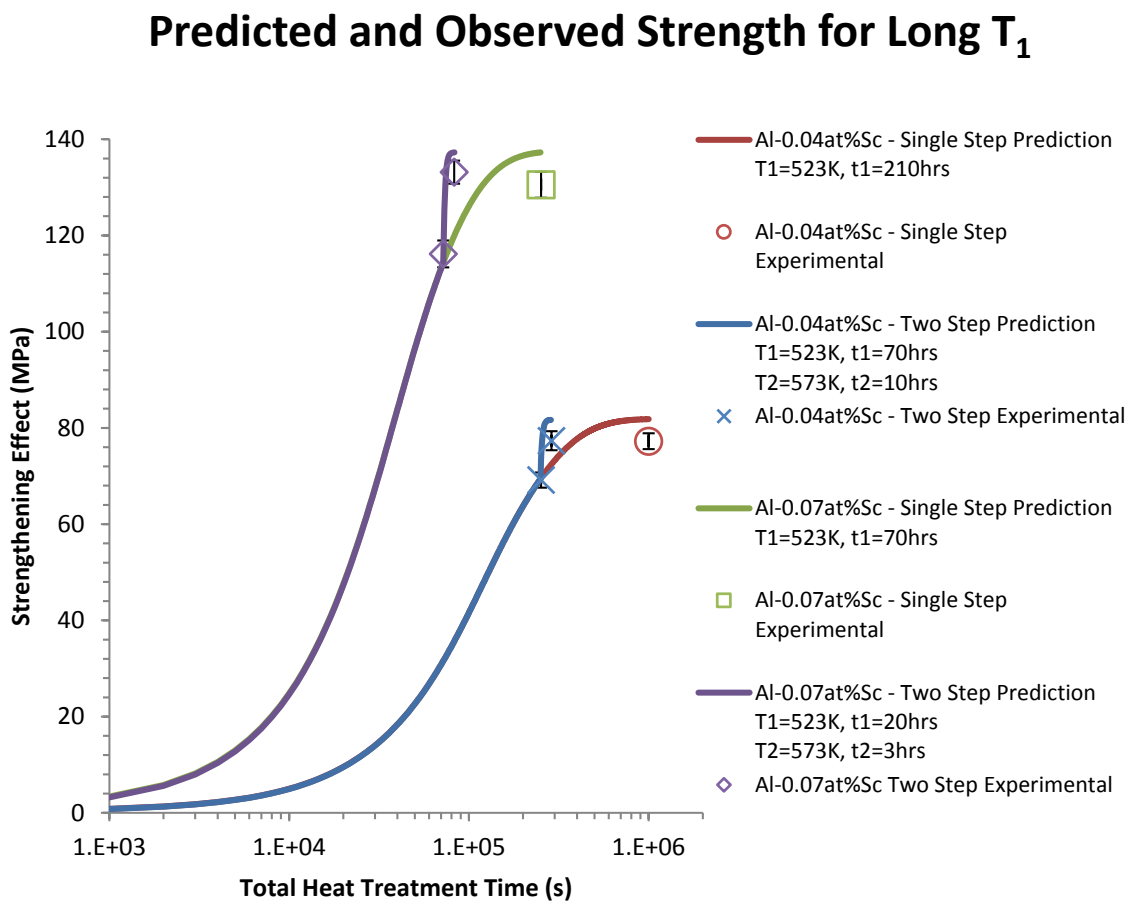

Figure 6.8: These graphs compare the observed strengthening effects (via Vickers hardness tests) and the corresponding model predicted Orowan strengthening effects for several heat treatments.

6.4.4 Predicting and Verifying Optimized Heat Treatments

In situations where heat treatments spanning several days are not feasible, and a target heat treatment time is imposed, it is useful to be able to predict the optimal heat treatment for that time. With that goal in mind, Bayesian Optimization processes were again employed, this time to adjust the heat treatment step times and temperatures and achieve the maximum strengthening effect possible. Table 6.4 demonstrates the results of one

such optimization, and Figure 6.9 shows a plotted comparison of the corresponding simulations and experimental verification data.

Table 6.4: Example Bayesian Optimization Limits and Optimized Results

	Upper Time Limit (s)		Optimized Time (s)		Optimized Temp (K)	
Alloy	**T_1**	**T_2**	**T_1**	**T_2**	**T_1**	**T_2**
Al-0.04at%Sc	10800	14400	14400	14354	259	344
Al-0.07at%Sc	10800	14400	14400	11634	255	305

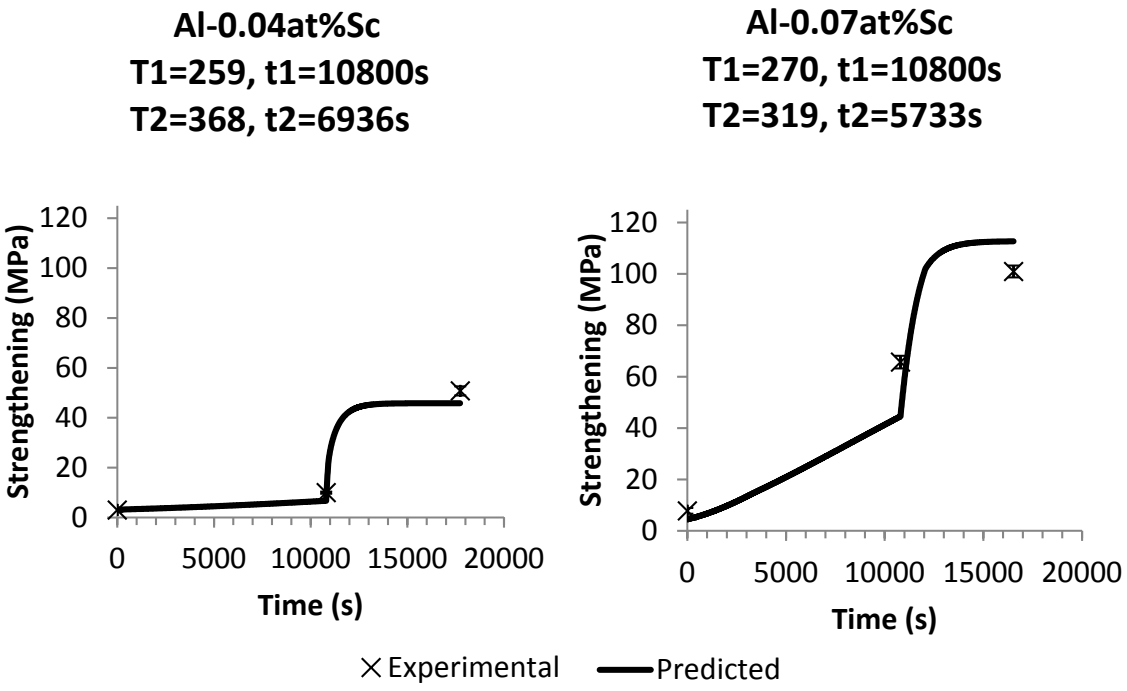

Figure 6.9: This plot compares the predicted and experimental results for heat treatments that were optimized using Bayesian Optimization to achieve the greatest strength given a restricted amount of time. In this case, t_1 and t_2 were limited to 3hrs each. In both cases, optimal strengthening at T_2 occurred before 3hrs.

6.5 Conclusions

In this study, a model was developed to predict the strength of Al-Sc alloys after multiple successive heat treatment steps. The use and theory of this model is described in Section 6.4.2, and the Matlab code itself is annotated and included in Appendix A.2. Using Bayesian Optimization of the relevant precipitate-matrix interfacial energy values in order to adjust model predictions to more closely match experimental results, the surface energy values for Al_3Sc at the onset of nucleation and during coarsening were predicted to be 0.096 and 0.158 J/m^2 respectively. These values are similar to the initial values that were found in literature (0.094 And 0.165 J/m^2). The model fits experimental data relatively well, although in multi-step heat treatments some bias towards underpredicting peak strength and delaying coarsening at high temperatures was observed. However, at the heat treatment temperatures relevant to this chapter, 523-573K, (250-300˚C) the fit is sufficient.

Through analysis of model simulations, some guidelines for obtaining the maximum achievable strengthening in these alloys were found:

1. In Al-Sc alloys that don't achieve Order strengthening dominance, the greatest strength can be achieved by minimizing the final average radius. This can be achieved by holding initially at a heat treatment temperature with ample nucleation activity and minimal growth activity (eg. 523K) until the nucleation rate becomes negligible due to decreasing supersaturation. At this point, the

maximum number of precipitates possible has been reached, and continuing heat treatment at that temperature, or at a reasonable higher temperature (eg. 573K) will result in the minimal average radius.

2. Ideally, two heat treatment steps should be used for Al-Sc alloys, as full depletion of the matrix after the initial nucleation treatment at proper nucleation temperatures can be prohibitively time consuming. Adding a short, higher temperature second step can significantly decrease the total time required.

3. Sc concentrations greater than Al-0.07at%Sc are suggested in order to achieve the full potential of the Sc additions. Increasing solute concentration was shown with simulations to decrease the final achievable average size of precipitates by allowing a greater comparative number density of precipitates to be nucleated. An alloy with Al-0.04at%Sc is predicted to be unable to achieve precipitates small enough to allow for Ordered strengthening dominance, while Al-0.07at%Sc was predicted to be able to form small enough precipitates only in a minority of circumstances (eg., T_1=523K, t_1=10hrs).

In recognition that long, low temperature heat treatments are not always possible in an industrial setting, Bayesian Optimization of the model was used to determine ideal strengthening time and temperature parameters given upper time limits. For the demonstrated examples, the maximum achievable strength was considerably lower than

what would be possible with the long, low temperature heat treatments, but the computer-optimized temperature parameters succeeded in predicting a slightly stronger final strength than could be achieved with more traditional, rounded temperature values. This demonstrated approach could be repurposed for other time limitations, etc, if required. However, designing heat treatments by determining the time required to nucleate the maximum number of precipitates through simulation generally results in greater strengthening.

Chapter 7: Effect of Zr Additions on Thermal Stability of Al-Cu precipitates in As-Cast and Cold Worked Samples

7.1 Abstract

Commonly used Al precipitation strengthening alloys based on the Al-Cu system offer a significant amount of strengthening to the base Al strength, presuming proper aging to achieve optimal precipitate size and number densities. However, if these aged alloys encounter elevated temperatures higher than ~473K (~200˚C), their strengthening effect is diminished due to unwanted precipitate growth (coarsening), and can only be returned with heat treatments to completely solutionize the Cu and then reestablish the ideal precipitate morphology. Al-Zr alloys coarsen at higher temperatures than Al-Cu, but are comparatively limited in strength due to a limited solubility of Zr in FCC Al [7]. This chapter describes experiments in which Al-Cu-Zr alloys were heat treated in an attempt to increase the coarsening resistance of the Al-Cu precipitate phases. Hardness testing and TEM results are discussed, in which it is found that coarsening differences do occur, although no significant change in strengthening is observed.

7.2 Experimental Design

7.2.1 Reasoning of Experiments

Al_3Zr precipitates are coarsening resistant up to temperatures greater than 673K (400˚C), although the low solubility of Zr in Al limits the effectiveness of Al_3Zr precipitates as a primary strengthening method [16,29]. The primary goal of these experiments was to assess if Zr additions to Al-Cu alloys could increase the thermal stability of Al-Cu precipitation strengthening. To this effect, two sets of experiments were run, each comparing Al-Cu and Al-Cu-Zr alloys: 1) an isothermal heat treatment at 473K (200˚C), quenching and taking hardness measurements periodically throughout the hold, and 2) a multi-step heat treatment that increased in temperature from 443K (170˚C) to 643K (370˚C) with 5 hour holds at each temperature, quenching and taking hardness measurements between each step.

As the goal of these experiments was to observe the effect of Al_3Zr precipitates, it was necessary to nucleate and grow these precipitates with an initial heat treatment procedure before holding at 443K (170˚C). Relevant phase diagrams were consulted to determine appropriate heat treatments for these alloys with the end goal of having the majority of Zr solute atoms precipitated out of solution into coherent Al_3Zr precipitates while retaining the Cu solute atoms in solution in the matrix. The concentration levels of Zr and Cu are low enough in these alloys that the respective binary phase diagrams can approximate the trends expected in the ternary alloy. These phase diagrams (Figure 7.1), along with the listed points that immediately follow this paragraph, describe the heat treatment steps that were decided on and the reasoning behind their selection.

1) The initial required step is a step to nucleate Al_3Zr precipitates. Literature review indicates that precipitation strengthening occurs in Al-Zr alloys at and above temperatures ~648K (375˚C) [16,29]. Because the second required step must be at a temperature high enough that unwanted coarsening of these precipitates will occur (discussed in next list item), the ideal initial temperature was taken to be at the low end of the range, 648K (375˚C), to reduce the final size of the Al_3Zr precipitates.

2) During the initial step, the temperature was sufficiently high enough to fully precipitate and anneal Al-Cu precipitates. The second required step was designed to re-solutionize the Cu solute atoms, so that preferred microstructural arrangements and strengthening could be achieved at a later step. To avoid excessive overaging of the Al_3Zr precipitates, it was desired to keep this step as low in temperature as possible while still achieving solutionization of Cu. With this in mind, 773K (500˚C) was chosen.

3) Once the initial heat treatment steps were completed and the microstructure was as desired, the aging and overaging steps were performed as discussed in Section 7.2.2. Aging steps should be below 473K (200˚C) and closely approximate the artificial aging treatments of binary Al-Cu alloys.

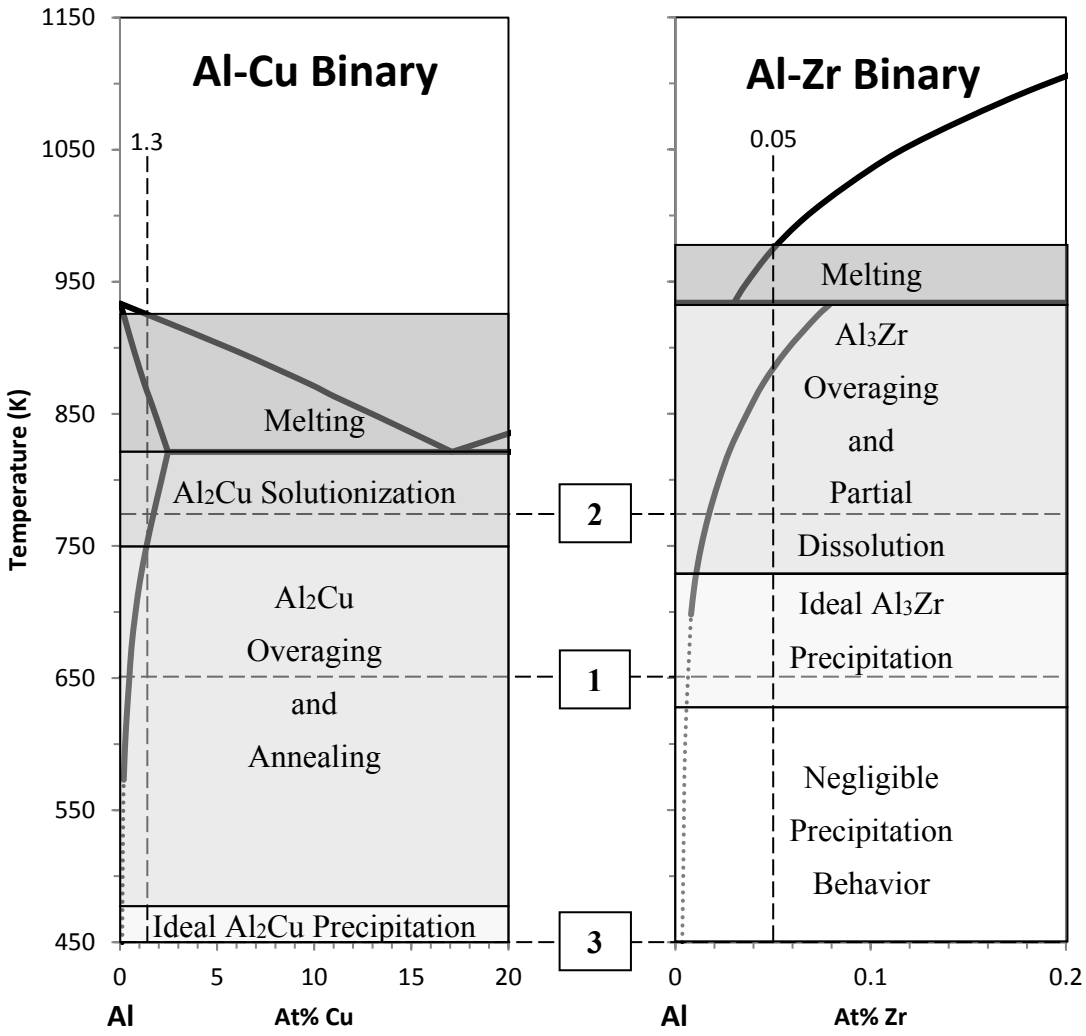

Figure 7.1: These phase diagrams demonstrate the delicacy of choosing optimal heat treatments for Al-Cu-Zr alloys. Because these alloys have low Zr content, the binary diagrams are close approximations to the ternary reality to determine trends. Vertical dashed lines on these diagrams denote the main alloy used in this study. The horizontal dashed lines (1, 2, and 3) indicate the order/temperature of heat treatment steps required to nucleate and grow Al_3Zr precipitates before aging. The list preceding this image in Section 7.2.1 describes these steps more fully.

Looking at the phase diagrams in Figure 7.1, several other notable conclusions can be drawn. For one, the high liquidus temperature range of the Al-Zr phase diagram makes it necessary to reach much higher temperatures with the melting of Zr bearing alloys in order to fully dissolve Al_3Zr precipitates into the liquid. This effect is even more pronounced when adding Zr from master alloys with higher comparative Zr contents, as the large Zr precipitates sink and can create areas of the melt with higher liquidus temperatures.

Another notable conclusion is that it is impossible to solutionize the Zr once these alloys are created. Any attempt to bring the alloy above the solvus temperature for Zr would result in partial melting of the Al matrix. Therefore, proper care must be taken with these alloys, as they are less forgiving to botched heat treating than current precipitation strengthening alloys.

Finally, it can be noted that at the Al-Cu solutionizing temperature of 773K (500˚C) the Al_3Zr precipitates can be expected to partially dissolve into the solid solution. This is not ideal, but it cannot reasonably be avoided. The Al-Cu solutionizing temperature can in fact be lowered to a temperature which would preserve the Al_3Zr precipitates better, but the only way to achieve this without adding other additions is to decrease the alloy Cu concentration and in turn the potential for Al-Cu strengthening (see the solvus line for the Al-Cu binary in Figure 7.1).

7.2.2 Experimental Setup

Samples discussed in this chapter were all originally cast in the vacuum induction melter (Section 3.14). In preparation for this process, master alloys were cut up using a horizontal band saw (Section 3.11.2) and weighed out in the proper amounts to make 600g charges of the compositions listed in Table 7.1, as is described in Section 3.13. After solidification, a hole was drilled in each casting to create chips, and the chips were analyzed with ICP-OES to verify the sample chemistry (Section 3.5). Samples with a thickness of ~1 cm were sectioned from the center of one bar for each casting using an abrasive cutoff disc (Section 3.11.3), and mounted in epoxy. The mounted samples were then ground and polished to a final finishing step of 0.04 micron colloidal silica (Section 3.12).

Table 7.1: Expected and Observed Alloy Compositions

	Al-1.3at%Cu		**Al-1.3at%Cu-0.05at%Zr**		**Al-1.3at%Cu-0.25at%Zr**	
Element	**Expected**	**ICP**	**Expected**	**ICP**	**Expected**	**ICP**
Cu (at%)	1.30	1.30	1.30	1.42	1.30	1.31
Zr (at%)	-	-	0.05	0.05	0.25	0.27

Initial hardness testing was performed on each sample to achieve a baseline, and then the epoxy was broken off in preparation for heat treating (Section 3.12.1). Heat treating was performed on the samples in a Thermolyne box furnace with a Furnatrol 53600 Controller according to the schedules depicted in Table 7.2. Between each heat treatment

step the samples were quenched in water as they were removed (Section 3.4), and epoxy was then re-applied to the samples in such a way that minimal polishing was required to achieve a polished surface (Section 3.12.1). This process was then repeated, starting at the beginning of this paragraph, until all desired heat treatments were accomplished.

Table 7.2: Heat Treatment Schedules for Al-Cu-Zr Experiments

Experiment 1 Aging at 473K				**Experiment 2 Stepped Aging**		
Step	**Time (hr)**	**Temp (K)**		**Step**	**Time (hr)**	**Temp (K)**
1)	3	623	**←Nucleate Al_3Zr→**	**1)**	3	648
2)	3	798	**←Solutionize Cu→**	**2)**	1	773
3)	6	473	**← Age →**	**3)**	5	443
4)	12 (18 total)	473	↓	**4)**	5	493
5)	18 (36 total)	473	**← Over-age →**	**5)**	5	543
6)	24 (60 total)	473	↓	**6)**	5	593
7)	30 (90 total)	473		**7)**	5	643
8)	36 (126 total)	473				
9)	42 (168 total)	473				
10)	48 (216 total)	473				

7.3 Results and Discussion

7.3.1 Experimental Results and Discussion

Hardness testing results from between each heat treatment step of the two experiments (described previously in Table 7.2) can be seen in Figures 7.2 and 7.3 respectively. From

these results it can be seen that Zr bearing Al-Cu alloys invariably maintain a higher strengthening increment. This strengthening increment appears to be thermally stable at elevated temperatures that would normally coarsen and over-age Al-Cu (primarily Al_2Cu) precipitates. This in itself is promising, especially as the alloy containing only 0.05at%Zr is shown to have a similar strengthening effect as the alloy containing 0.2at%Zr, implying that small additions of Zr are equally as effective as larger ones. However, the results do not indicate any noticeable increase in thermal stability of the total overall strength that would be expected to accompany any improvement in coarsening resistance of the Al-Cu precipitate phases.

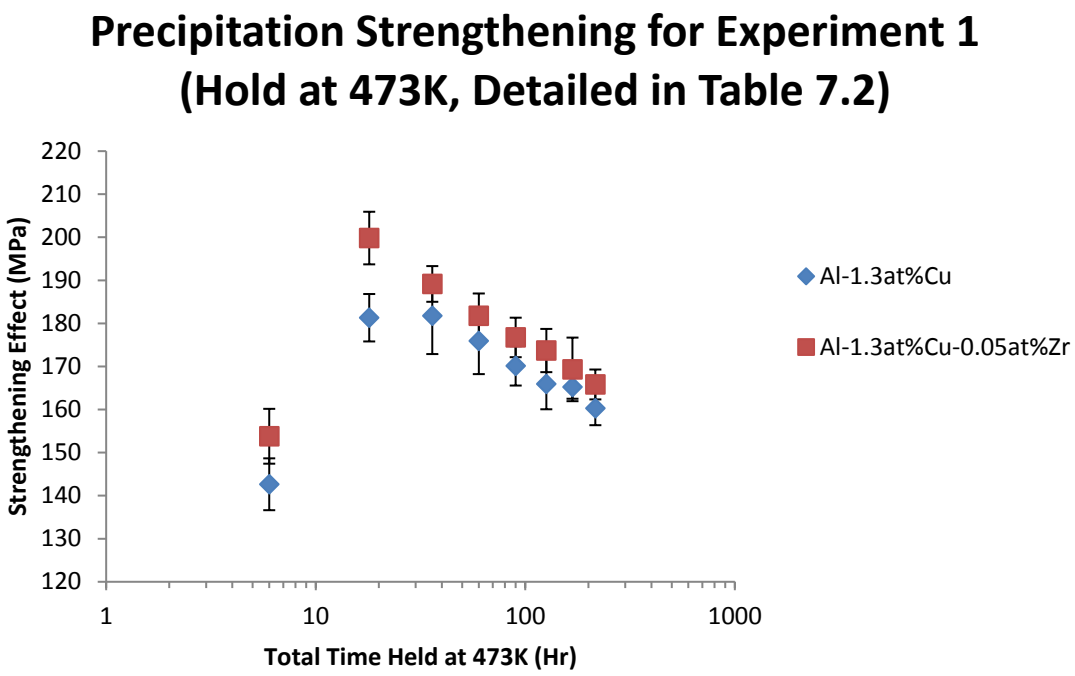

Figure 7.2: This graph shows the overaging of two Al-Cu alloys at 473K, one alloy with Zr additions and one without. In this experiment, the Zr containing alloy had a slightly higher strengthening increment than the Al-Cu binary. Error bars represent +/- 2 std error.

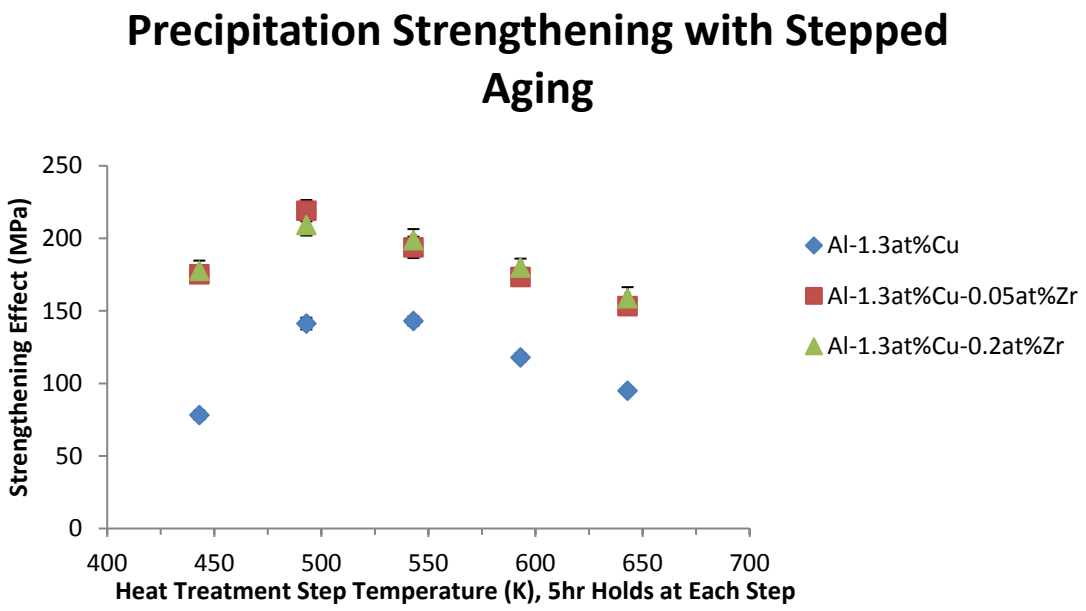

Figure 7.3: This image shows the overaging of Al-1.3at%Cu as consecutively higher 5hr heat treatments are performed, compared with overaging in the same alloy with two different levels of Zr additions. While there is little statistical difference between the two Zr bearing alloys, a significant strengthening increment can be seen in both of them when compared to the Al-Cu binary. Error bars represent +/- 2 std error.

It should be noted that the difference between Al-1.3at%Cu and Al-1.3at%Cu-0.05at%Zr is greater in Experiment 2 than in Experiment 1. This is thought to be due to the lower Al_3Zr nucleation temperature and the higher Cu solutionizing time/temperature associated with Experiment 1, both of which would result in suboptimal Al_3Zr precipitation (limited number density, coarsening to the point of annealing, and phase dissolution due to higher solvus line compositions as shown previously in Figure 7.1).

Without consulting TEM images of the sample microstructure, the false assumption could be reached that the Zr additions do not significantly affect the Al-Cu precipitation behavior, and that the thermally stable strengthening increment is entirely due to the formation of coherent Al_3Zr precipitates. However, TEM images of the samples taken after completion of Experiment 2 (Table 7.2) show that Al-Cu precipitates found in the Al-1.3at%Cu sample have measured lengths ~3x longer than the precipitates found in both of the Al-1.3at%Cu-(0.05, 0.2)at%Zr samples, suggesting that the addition of Zr does indeed limit the growth of Al-Cu precipitates significantly. Relevant representative images are shown in Figure 7.4, and a comparison of observed precipitate lengths and aspect ratios between the three alloys used in Experiment 2 can be seen in Figure 7.5. It is shown that Al-Cu aspect ratio distributions are consistent between Al-Cu and Al-Cu-Zr alloys, and that average Al-Cu length is similar in both observed Al-Cu-Zr alloys.

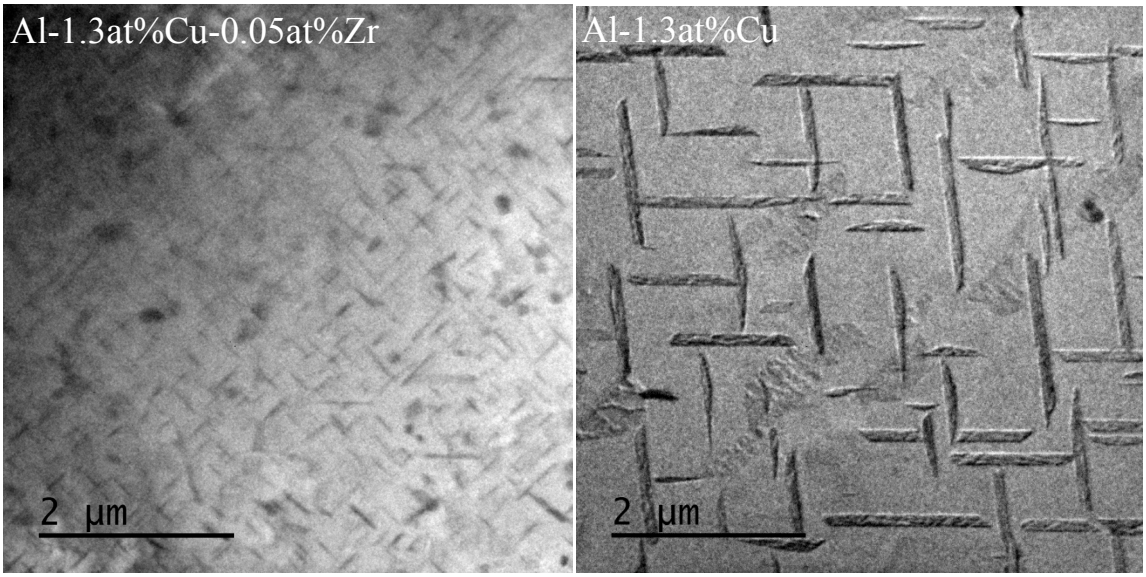

Figure 7.4: These TEM images demonstrate the difference in Al-Cu precipitate growth between an Al-Cu alloy with and without Zr additions.

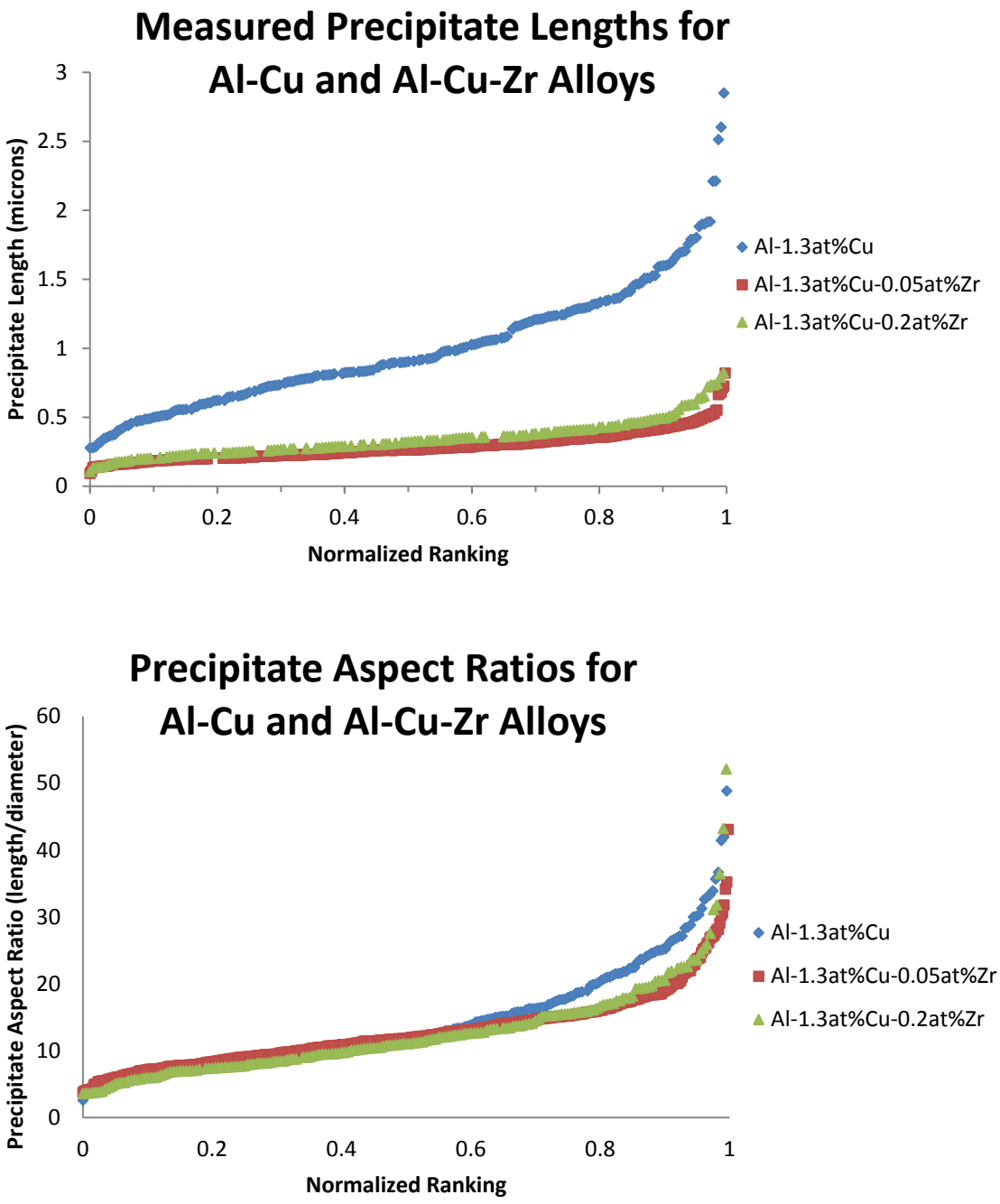

Figure 7.5: These graphs show the observed lengths and length-width aspect ratios of Al-Cu (primarily Al_2Cu) precipitates in the three different alloys. These measurements were made on TEM images of the alloys after completion of the 643K (370˚C) stepped heat treatment described in Section 7.2.

Upon closer inspection of the TEM images for the stepped heat treatment Al-Cu-Zr alloys, precipitates other than the elongated Al-Cu precipitate phase become apparent, as seen in Figure 7.6. These more rounded precipitates contain not only Al and Zr, as would be the case with simple Al_3Zr precipitate phase, but significant quantities of Cu as well, when compared to the matrix.

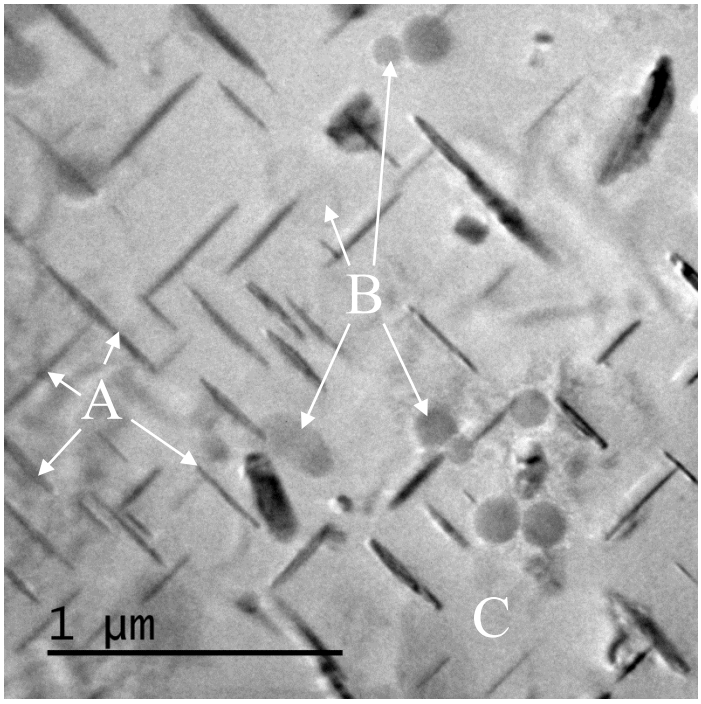

Figure 7.6: This TEM image of the Al-1.3at%Cu-0.05at%Zr sample shows the three different phases observed during TEM of the Al-Cu-Zr alloys: A) elongated Al-Cu precipitates, B) rounded Al-Cu-Zr precipitates, and C) the Al matrix phase. Several locations where Al-Cu precipitates and Al-Cu-Zr precipitates intersect are visible within this image as well.

The formation of these Al-Cu-Zr precipitates likely occurred during the initial Al_3Zr formation heat treatment step, due to the presence of significant Cu solute concentration. While many Al-Cu-Zr intermetallic phases are known to exist [53], none are expected to be present in alloys with such a high Al concentration. However, while holding the samples at 773K (500˚C), the majority of the Al_3Zr precipitate growth occurred in an environment with much higher Cu matrix concentration, due to the solutionization of Cu. It is feasible that the higher levels of Cu concentration were retained within the Al_3Zr precipitate phase even while Al-Cu precipitation depleted the matrix in the surrounding matrix.

It is also interesting to note that the Al-Cu and Al-Cu-Zr precipitates intercept each other in several instances within Figure 7.6. These instances are representative of all such behavior observed in other Al-Cu-Zr TEM images, in that the elongated Al-Cu precipitates tend to terminate in or on an Al-Cu-Zr precipitate when they intercept. This behavior is indicative of the nucleation of Al-Cu precipitates on Al-Cu-Zr precipitates, which has been previously reported in the literature [54]. Nucleation on the Al-Cu-Zr precipitates could potentially be due to the nature of the Al-Cu-Zr precipitates, as discussed in the last paragraph as being simply Al_3Zr precipitate phase with an excess of trapped Cu atoms from aging at 773K (500˚C). This phenomenon contributes to lower average sizes of Al-Cu precipitates in the Zr bearing alloys by increasing the number density of precipitates.

Comparison of TEM EDS scans for the three phases indicated in Figure 7.6 can be found in Figure 7.7. Because these scans are on TEM samples, it should be acknowledged that ratios between Al and Cu/Zr counts are relatively meaningless without knowledge of the quantity of matrix phase that the beam passes through. However, the ratio between Cu and Zr counts is meaningful assuming that there is only one type of precipitate phase being hit by the beam. Therefore, the difference in Cu:Zr intensity between the Al-Cu and Al-Cu-Zr precipitates in Figure 7.7 clearly indicates the two precipitate phases are of different compositional makeup. It should also be noted that the Zr content in the scan for the Al-Cu precipitate is not universal; some of the Al-Cu precipitates observed showed no noticeable Zr content, although that could potentially be due to inaccuracies in measuring low concentration elements in relatively thin precipitates.

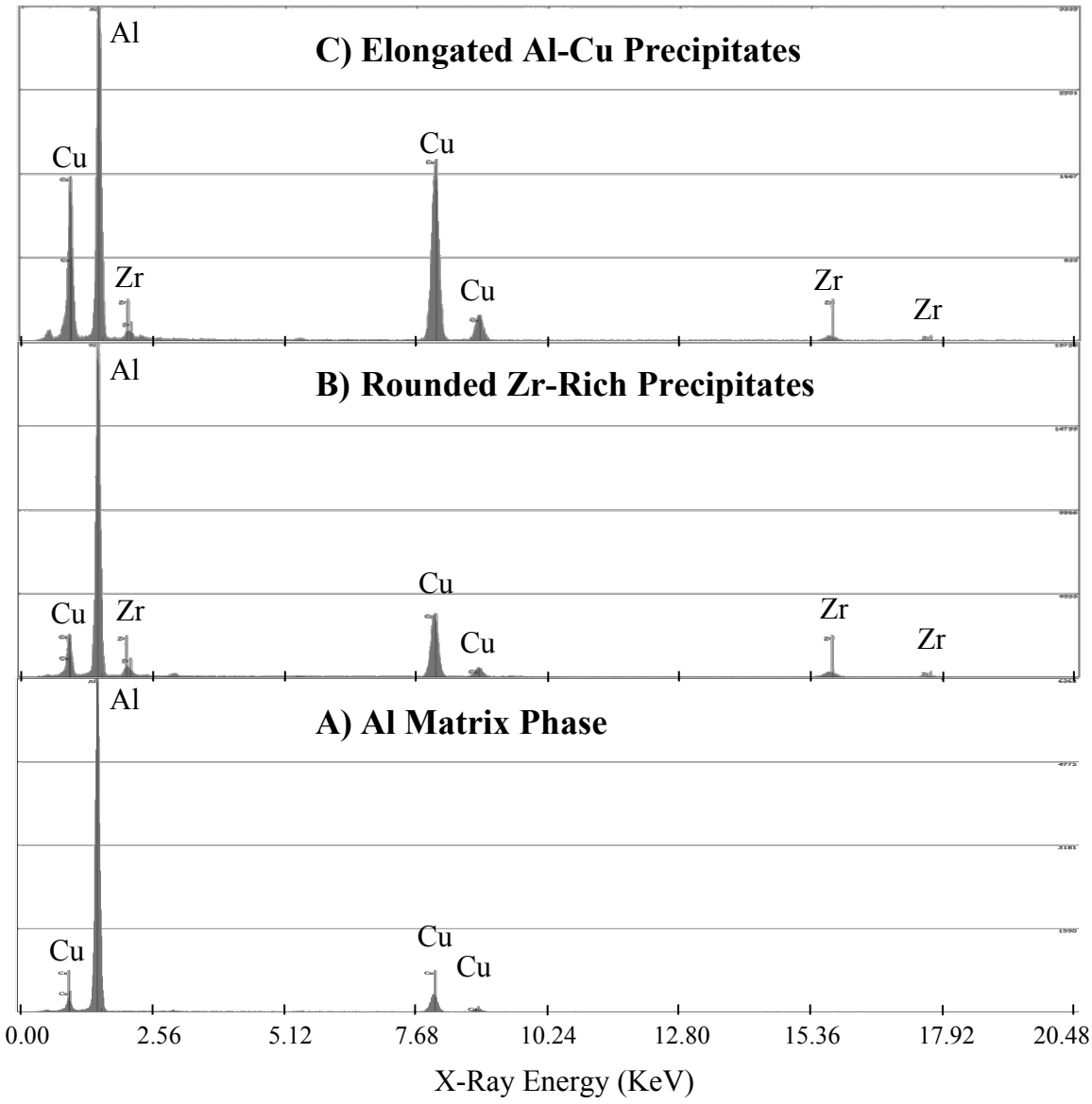

Figure 7.7: During TEM analysis of Al-1.3at%Cu-0.05at%Zr samples aged according to the schedule for Experiment 2 (Table 7.2), these EDS scans were obtained of the three main phases that were observed. Microstructural images of these phases, labeled as A, B, and C, are clearly pointed out in Figure 7.6.

7.4 Conclusions

In this chapter, experiments were run to determine whether Zr additions to Al-Cu binary alloys could increase the thermal stability of the relevant Al-Cu precipitates. While no significant change in the rate at which strengthening decreased during overaging was observed, TEM images taken of the samples at the end of a series of increasing heat treatment steps showed that alloys with Zr additions had final average Al-Cu precipitate lengths of approximately 1/3 that of the binary Al-Cu alloy. Also present in TEM images of the Al-Cu-Zr alloy were rounded precipitates that were found to contain both Zr and Cu atoms. These rounded precipitates, thought to be Al_3Zr precipitates with retained Cu atoms from aging at 773K (500˚C), appear to behave as nucleation sites for the Al-Cu precipitates, which increased the nucleation density and limited average growth of the Al-Cu precipitates. Some of the Al-Cu phase precipitates were also found to contain small amounts of Zr as well, although this was not widespread. One potential consequence of the rounded precipitates containing significant Cu content (as opposed to being simple stoichiometric Al_3Zr) is that the potential volume fraction of elongated Al-Cu precipitate would be reduced.

One possible reason that the binary alloy did not appear to overage faster in accordance with its faster precipitate growth compared to the Al-Cu-Zr alloys is that a large portion of the strengthening with precipitates of this size is due to solid solution strengthening, which behaves similarly in both alloys. While this effect is calculated as the dominant strengthening effect in the alloy given information drawn from the TEM images, the strengthening effect of the precipitates should still be a significant factor, and differences

in the coarsening behavior should be reflected in the total strength. This tends to indicate that there may be another competing effect at play in regards to strengthening. This could also imply that the coarsening rate is not significantly different with the addition of Zr, but that there were simply higher initial precipitate nucleation events in the Al-Cu-Zr alloys due to the presence of Zr, and therefore the average precipitate size was smaller in Zr bearing alloys by the time precipitate growth transitioned from being mainly matrix depletion driven to being coarsening driven. Future experiments will attempt to more thoroughly document the Al-Cu precipitate growth during overaging in an attempt to understand this phenomenon more fully. These experiments will also include long isochronal aging of Al-Cu-Zr alloys with properly set up Al_3Zr precipitates.

Chapter 8: Summary

Comprising Sections 8.1-8.4, this chapter begins with a collection of the relevant conclusions sections for each of the experimental chapters (Chapters 4, 5, 6, and 7). Section 8.5 then ties the conclusions together into an overarching summary of findings of this report.

8.1 Summary - Precipitate Evolution and Strengthening in Rapidly Solidified Supersaturated Al-Sc and Al-Zr Alloys

In Chapter 4, a method for determining the achievable supersaturation of precipitate strengthening alloys under specific solidification conditions was demonstrated through the use of XRD lattice parameter measurements. With this method it was found that Sc and Zr can be supersaturated in Al at concentrations of at least 0.55 at% Zr and 0.8 at% Sc with the rapid solidification setup described in Section 3.1. This supersaturation allows for an increase in achievable precipitation phase fraction over traditionally cast Al-Sc alloys, and in turn, enhanced strengthening. While precipitate strengthened melt spun ribbon is not immediately useful in an industrial setting, the ability to create and study such a material may facilitate the development of new uses.

Multi-step heat treatments of Al-0.4 at%Sc, Al-0.27 at%Zr and Al-0.4 at%Sc-0.27 at%Zr with subsequent XRD and TEM analyses indicate that these alloys begin precipitation at 473, 573, and 573K (200, 300, and 300˚C), respectively, and reach maximum precipitate phase fraction at 748, 823, and 848K (475, 550, and 575˚C), respectively. These analyses also indicate that precipitation in binary Al-Sc and Al-Zr alloys behaves as would be expected by the LSW model at elevated supersaturations, and that ternary Al-Sc-Zr demonstrates behavior between that of either of the binaries. This is interpreted to mean that a core-shell precipitate structure has been formed as in more dilute alloys with similar heat treatment regimens, and the largely Al_3Zr precipitate phase at the outer edge of the precipitate limits the ability of the Sc atoms to move between precipitates. However, there was no direct observable indication of interprecipitate segregation of Sc and Zr within the nanoscale precipitates that were observed during the TEM analysis. Future work should include an analysis of similar ribbons with atom probe tomography, which has been demonstrated to be sensitive enough to observe the segregation in other literature [16], or with a higher resolution STEM/TEM.

Calculations for the predicted precipitation strengthening for these alloys using observed average radii and phase fraction indicate that a greater strength could be obtained with the application of a more suitable heat treatment. Each alloy experienced precipitate coarsening that resulted in the Orowan strengthening mechanism becoming dominant over the more potent order strengthening mechanism, and this occurred before the precipitate phase could entirely form in the Sc containing alloys. By adding the kinetic information gleaned from this study to other sources describing similar heat treatment

schedules in literature [16,29], it should be possible to optimize the fitting of more advanced models, such as the Kampmann-Wagner Numerical (KWN) model, to predict heat treatments that would result in higher number densities of smaller precipitates in these alloys.

This work demonstrates that rapid solidification can be used to create supersaturated Al-(Sc.Zr) alloys with increased precipitation strengthening potential. Two notable downsides to this technique are: 1) melt spinning is not a common industrial process, and 2) the resulting ribbon is not immediately suitable for industrial use. The first downside can be easily overcome if there is an industrial application, as melt spinning can be suitably upscaled by increasing the crucible melt capacity, adding multiple spray nozzles, and incorporating active cooling into the copper wheel. Future work should include attempts to consolidate similar melt spun ribbons into a bulk form without melting in order to maintain the achieved supersaturations and address the second downside, with methods such as Additive Friction Stir processing (AFS).

8.2 Summary - Effect of Additive Friction Stir Processing on Supersaturated Al-Sc

In Chapter 5, a method for creating a thermally stable Sc-rich layer on the surface of an Al substrate through the use of rapidly solidified, supersaturated Al-Sc ribbon was described, and the resulting experiments were analyzed. The Sc distribution along the Additive Friction Stir (AFS) path itself was slightly unpredictable in nature, which is

believed to be due to inconsistencies in feedstock billet density, etc. Any industrialization of this prototype process should be able to create a more uniform Sc distribution. For the purposes of this analysis, focus was placed on analysis of the strengthening effect of Sc concentrations where available in the AFS path as opposed to the geometry and consistency of the path. Several different methods of representing the data were discussed, along with discussions of the scenarios that each method would benefit.

In low concentration areas of the sample (≤Al-0.06at%Sc), the analysis methods outlined in this work give an accurate assessment of the aging behavior of precipitates. While this analysis method offers a wealth of information about the AFS process and about a range of compositions of Al-Sc alloys, it is clear that the process fails to achieve the full potential of strengthening for Al-Sc alloys in areas with higher concentration. This is believed to be due to precipitate nucleation and growth during processing, which was briefly observed to reach temperatures upwards of 800K (523˚C). This precipitation behavior lowered the Sc saturation concentration from that initially achieved with rapid solidification to near equilibrium levels. Therefore in areas of high Sc concentration, the majority of Sc has negligible contributions to strengthening because it is tied up in precipitates that are far larger than the optimal 1-3nm radius size. In alloys such as this, where the Sc matrix concentration is considerably higher than the solvus concentration and Sc was only coaxed into solid solution through the use of rapid solidification, overaged Al_3Sc precipitates will have no opportunity to be homogenized. Any attempt to gain higher strengths for this material will require a complete melting and repetition of this process, which will in turn add unwanted impurities to the melt.

While much of the extended supersaturation from the melt spun feedstock did not survive the transfer into the bulk Al substrate, it is very promising that any supersaturation survived at all. With further studies into this process, it is feasible that improvements in processing parameters and active cooling could increase the Sc solution concentrations which are transferred to the substrate (still in solution), which would in turn allow for an increase in achievable strengthening effect for this method.

8.3 Summary - Designing Al-Sc Alloy Heat Treatment Schedules with the Kampmann and Wagner Numerical Model

In Chapter 6, a model was developed to predict the strength of Al-Sc alloys after multiple successive heat treatment steps. The use and theory of this model is described in Section 6.4.2, and the Matlab code itself is annotated and included in Appendix A.2. Using Bayesian Optimization of the relevant precipitate-matrix interfacial energy values in order to adjust model predictions to more closely match experimental results, the surface energy values for Al_3Sc at the onset of nucleation and during coarsening were predicted to be 0.096 and 0.158 J/m^2 respectively. These values are similar to the initial values that were found in literature (0.094 And 0.165 J/m^2). The model fits experimental data relatively well, although in multi-step heat treatments some bias towards underpredicting peak strength and delaying coarsening at high temperatures was observed. However, at the heat treatment temperatures relevant to this chapter, 523-573K, the fit is sufficient.

Through analysis of model simulations, some guidelines for obtaining the maximum strengthening achievable in these alloys were found:

1. In Al-Sc alloys that don't achieve Order strengthening dominance, the greatest strength can be achieved by minimizing the final average radius. This can be achieved by holding initially at a heat treatment temperature with ample nucleation activity and minimal growth activity (e.g., 523K) until the nucleation rate becomes negligible due to decreasing supersaturation. At this point, the maximum number of precipitates possible has been reached, and continuing heat treatment at that temperature, or at a reasonable higher temperature (e.g., 573K) will result in the minimal average radius.

2. Ideally, two heat treatment steps should be used for Al-Sc alloys, as full depletion of the matrix after the initial nucleation treatment at proper nucleation temperatures can be prohibitively time consuming. Adding a short, higher temperature second step can significantly decrease the total time required.

3. Sc concentrations greater than Al-0.07at%Sc are suggested in order to achieve the full potential of the Sc additions. Increasing solute concentration was shown with simulations to decrease the final achievable average size of precipitates by allowing a greater comparative number density of precipitates to be nucleated. An alloy with Al-0.04at%Sc is predicted to be unable to achieve precipitates small

enough to allow for Ordered strengthening dominance, while Al-0.07at%Sc was predicted to be able to form small enough precipitates only in a minority of circumstances (eg., T_1=523K, t_1=10hrs).

In recognition that long, low temperature heat treatments are not always possible in an industrial setting, Bayesian Optimization of the model was used to determine ideal strengthening time and temperature parameters given upper time limits. For the demonstrated examples, the maximum achievable strength was considerably lower than what would be possible with the long, low temperature heat treatments, but the computer-optimized temperature parameters succeeded in predicting a slightly stronger final strength than could be achieved with more traditional, rounded temperature values. This demonstrated approach could be repurposed for other time limitations, etc., if required. However, designing heat treatments by determining the time required to nucleate the maximum number of precipitates through simulation generally results in greater strengthening.

8.4 Overarching Summary and Conclusions for Chapters 4-6

Throughout the course of this work, emphasis has remained on increasing the strengthening of Al-Sc/Zr alloys or conversely in increasing the thermal stability of other alloy Al precipitation alloys with the help of Sc/Zr. While some experiments were more successful than others, they all contributed valuable information and contributed to the larger picture.

In this work, it was verified that melt spinning could increase the supersaturation of Sc and Zr, and maximum achievable supersaturation levels were determined using XRD. For the melt spinner at Michigan Technological University, the achievable levels were found to be 0.8at%Sc and 0.55at%Zr. With that knowledge, fully saturated ribbon was produced and TEM analysis confirmed that, even with the artificially high solute content, precipitation behavior continues predictably.

As melt spun ribbon does not lend itself to structural applications well, the benefits of increasing supersaturation and the associated precipitate strengthening with melt spinning are negligible if there is no way to change the final form. However, any consolidation methods that require melting or high homologous temperatures are certain to deplete the matrix of the supersaturation. A collaboration with Aeroprobe Corporation resulted in access to a method of mechanically mixing two alloys without melting, known as Additive Friction Stir processing (AFS). Using this method to mechanically mix the high supersaturation Al-Sc ribbon into the surface of a pure Al substrate, a Sc enriched layer was formed, penetrating approximately 2.5 mm into the sample.

Analysis of this layer was performed, using WDS and Vickers hardness testing to determine the concentration and strengthening of the sample at a given point, and after different heat treatment steps. It was found from these tests that some supersaturation of Sc had persisted into the bulk material, as areas with low concentration (Al-0.06at%Sc for example) behave as would be expected. However, at higher concentrations the

strengthening plateaus, leading to the assumption that a portion of the Sc that is being recorded by WDS is in fact already tied up in precipitates. It is unclear whether the Sc that remains in solution was left because it was close to the equilibrium solvus at the processing temperatures for AFS, or because the slow kinetics of Sc in Al did not allow time for a full dissolution of the matrix at lower temperatures. Future work should look into this.

Another approach to improving the strength of these alloys attempted to optimize the heat treatment for Al-Sc to achieve the full strengthening potential associated with order strengthening, which is only dominant when the precipitates are below ~3nm in radius. To understand the precipitation behavior more completely and be able to predict optimal heat treatments, the Kampmann and Wagner Numerical model (KWN) was coupled with precipitate strengthening equations. This model was then calibrated to experimental data through the use of Bayesian Optimization (BO), and a series of predictions and experimental verifications were performed to test the accuracy of predictions.

It was determined that in general the greatest strength can be produced from much longer heat treatments than have been performed previously. These long heat treatments should allow the maximum number of precipitates to nucleate at the lower of two heat treatment steps before moving the sample to the second heat treatment step. The optimal temperatures for each heat treatment will vary, but in the case of this research, 523K (250˚C) was an adequate temperature for the first heat treatment step, and 573K (300˚C)

worked well for the second. Experimental verification of the long heat treatments showed an increase in strength in the sample, although it was slightly less than predicted.

Bayesian Optimization (BO) was also shown to be of great benefit, between assisting in calibrating the model to experimental results and predicting optimal temperatures for time-limited heat treatments. BO would also be beneficial if used to predict the optimal heat treatment temperature for use with the long, low temperature heat treatments.

8.5 Summary - Effect of Zr Additions on Thermal Stability of Al-Cu precipitates in As-Cast and Cold Worked Samples

In Chapter 7, experiments were run to determine whether Zr additions to Al-Cu binary alloys could increase the thermal stability of the relevant Al-Cu precipitates. While no significant change in the rate at which strengthening decreased during overaging was observed, TEM images taken of the samples at the end of a series of increasing heat treatment steps showed that alloys with Zr additions had final average Al-Cu precipitate lengths of approximately 1/3 that of the binary Al-Cu alloy. Also present in TEM images of the Al-Cu-Zr alloy were rounded precipitates that were found to contain both Zr and Cu atoms. These rounded precipitates, thought to be Al_3Zr precipitates with retained Cu atoms from aging at 773K (500˚C), appear to behave as nucleation sites for the Al-Cu precipitates, which increased the nucleation density and limited average growth of the Al-Cu precipitates. Some of the Al-Cu precipitates were also found to contain small amounts of Zr as well, although this was not widespread. One potential consequence of the

rounded precipitates containing significant Cu content (as opposed to being simple stoichiometric Al_3Zr) is that the potential volume fraction of elongated Al-Cu precipitate would be reduced.

One possible reason that the binary alloy did not appear to overage faster in accordance with its faster precipitate growth compared to the Al-Cu-Zr alloys is that a large portion of the strengthening with precipitates of this size is due to solid solution strengthening, which behaves similarly in both alloys. While this effect is calculated as the dominant strengthening effect in the alloy given information drawn from the TEM images, the strengthening effect of the precipitates should still be a significant factor, and differences in the coarsening behavior should be reflected in the total strength. This tends to indicate that there may be another competing effect at play in regards to strengthening. This could also imply that the coarsening rate is not significantly different with the addition of Zr, but that there were simply higher initial precipitate nucleation events in the Al-Cu-Zr alloys due to the presence of Zr, and therefore the average precipitate size was smaller in Zr bearing alloys by the time precipitate growth transitioned from being mainly matrix depletion driven to being coarsening driven. Future experiments will attempt to more thoroughly document the Al-Cu precipitate growth during overaging in an attempt to understand this phenomenon more fully. These experiments will also include long isochronal aging of Al-Cu-Zr alloys with properly set up Al_3Zr precipitates.

References

1. J. Royset, Met. Sci Tech **25**, 11 (2007).
2. Z. Ahmad, JOM **55**, 35 (2003).
3. L. S. Toropova, D. G. Eskin, M. L. Kharakterova, and T. V. Dobatkina, *Advanced Aluminum Alloys Conta* (Routledge, Amsterdam, The Netherlands, 1998).
4. J. L. Murray, J. Phase Equilibria **19**, 380 (1998).
5. H. Okamoto, J Phase Equilib **23**, 455 (2002).
6. *Mineral Commodity Summaries 2015* (U.S. Geological Survey, Reston, VA, 2015), p. 199.
7. K. E. Knipling, D. C. Dunand, and D. N. Seidman, Z. Für Met. **97**, 246 (2006).
8. S. I. Fujikawa, JJapan Inst Light Met. **46**, 22 (1996).
9. Y. B. Kang, A. D. Pelton, P. Chartrand, and C. D. Fuerst, CALPHAD Comput Coupling Phase Diagr. Thermochem **32**, 413 (2008).
10. S. Fujikawa, K. Hirano, and Y. Fukushima, Metall. Trans. A **9**, 1811 (n.d.).
11. S. I. Fujikawa and K. Hirano, Defect Diffus. Forum **66–69**, 447 (1991).
12. S. J. Rothman, N. L. Peterson, L. J. Nowicki, and L. C. Robinson, Phys. Status Solidi B **63**, K29 (1974).
13. S. I. Fujikawa, Defect Diffus. Forum **143–147**, 115 (1997).
14. D. Bergner and N. Van Chi, Wiss. Z. Padagogischen Hochsch. **25**, 15 (1977).
15. E. Clouet, L. Laé, T. Épicier, W. Lefebvre, M. Nastar, and A. Deschamps, Nat. Mater. **5**, 482 (2006).
16. K. E. Knipling, R. A. Karnesky, C. P. Lee, D. C. Dunand, and D. N. Seidman, Acta Mater. **58**, 5184 (2010).
17. C. B. Fuller, D. N. Seidman, and D. C. Dunand, Acta Mater. **51**, 4803 (2003).
18. D. N. Seidman, E. A. Marquis, and D. C. Dunand, Acta Mater. **50**, 4021 (2002).
19. A. J. Ardell, Metall. Trans. A **16**, 2131 (1985).
20. T. Courtney, *Mechanical Behavior of Materials*, 2 edition (Waveland Pr Inc, Boston, 2005).
21. E. Nembach, Phys. Status Solidi A **78**, 571 (1983).
22. *Mechanical Metallurgy: Principles and Application*, 1st edition (Prentice-Hall, Inc., Englewood Cliffs, N.J, 1983).
23. C. L. Fu, J. Mater. Res. **5**, 971 (1990).
24. C. L. Fu and M. H. Yoo, Mater. Chem. Phys. **32**, 25 (1992).
25. H. J. Frost and M. F. Ashby, *Deformation-Mechanism Maps: The Plasticity and Creep of Metals and Ceramics*, 1st edition (Pergamon Press, Oxford Oxfordshire ; New York, 1982).
26. E. P. George, J. A. Horton, W. D. Porter, and J. H. Schneibel, J. Mater. Res. **5**, 1639 (1990).
27. E. P. George, D. P. Pope, C. L. Fu, and J. H. Schneibel, Trans. Iron Steel Inst. Jpn. **31**, 1063 (1991).
28. K. Fukunaga, T. Shouji, and Y. Miura, Mater. Sci. Eng. A **239–240**, 202 (1997).
29. K. E. Knipling, D. N. Seidman, and D. C. Dunand, Acta Mater. **59**, 943 (2011).

30. S. Ceresara, M. Conserva, and P. Fiorini, Mater. Sci. Eng. **9**, 19 (1972).
31. S. K. Mukherjee, J. Mater. Sci. Lett. **19**, 1107 (2000).
32. B. D. Cullity and S. R. Stock, *Elements of X-Ray Diffraction*, 3 edition (Pearson, Upper Saddle River, NJ, 2001).
33. O. Beeri, D. C. Dunand, and D. N. Seidman, Mater. Sci. Eng. A **527**, 3501 (2010).
34. C. Booth-Morrison, Z. Mao, M. Diaz, D. C. Dunand, C. Wolverton, and D. N. Seidman, Acta Mater. **60**, 4740 (2012).
35. H.-S. Kim, B. Madavali, S.-J. Hong, and T.-S. Kim, Int. J. Appl. Ceram. Technol. (2015).
36. M. A. Korhonen, C. A. Paszkiet, R. D. Black, and C.-Y. Li, Scr. Metall. Mater. **24**, 2297 (1990).
37. J. G. M. van Berkum, R. Delhez, T. H. de Keijser, E. J. Mittemeijer, and P. van Mourik, Scr. Metall. Mater. **25**, 2255 (1991).
38. I. M. Lifshitz and V. V. Slyozov, J. Phys. Chem. Solids **19**, 35 (1961).
39. H. A. Calderon, P. W. Voorhees, J. L. Murray, and G. Kostorz, Acta Metall. Mater. **42**, 991 (1994).
40. S. I. Fujikawa, (1997).
41. K. Hirano and S. I. Fujikawa, J. Nucl. Mater. **69**, 564 (1978).
42. M. A. Kerkove, T. D. Wood, P. G. Sanders, S. L. Kampe, and D. Swenson, Metall. Mater. Trans. A **45**, 3800 (2014).
43. E. Nes, Acta Metall. **20**, 499 (1972).
44. E. A. Marquis and D. N. Seidman, Acta Mater. **49**, 1909 (2001).
45. G. M. Novotny and A. J. Ardell, Mater. Sci. Eng. A **318**, 144 (2001).
46. (n.d.).
47. R. Wagner, R. Kampmann, and P. Voorhees, in *Phase Transform. Mater.*, edited by G. Kostorz (Wiley-VCH Verlag GmbH & Co. KGaA, 2001), pp. 309–480.
48. J. D. Robson, Acta Mater. **52**, 4669 (2004).
49. J. D. Robson, M. J. Jones, and P. B. Prangnell, Acta Mater. **51**, 1453 (2003).
50. *A First-Principles Methodology for Diffusion Coefficients in Metals and Dilute Alloys* (ProQuest, 2008).
51. Scribd (n.d.).
52. M. Perez, Scr. Mater. **52**, 709 (2005).
53. M. S. I. T. Msit®, in *Light Met. Syst. Part 2*, edited by G. Effenberg and S. Ilyenko (Springer Berlin Heidelberg, 2005), pp. 1–17.
54. M. Kanno and B.-L. Ou, Mater. Trans. JIM **32**, 445 (1991).

Appendix A: Codes

A.1: LabView Code for Automated VIM Control

This appendix documents the Labview program that was developed to control the automatic pouring apparatus attached to the Vacuum Induction Melter (VIM) in order to increase the repeatability of casting operations. The stepper motor that this code controls runs off of serial commands fed through a RS-232 port, and could originally be sent these commands manually through a supplied user interface. This method proved unnecessarily complicated for new users, especially as the Autopour was intended to improve the ease of pouring samples. This program was therefore developed to take user inputs, convert them into inputs the stepper motor could understand (# steps /minute, etc), and then send derivative serial commands to the stepper motor.

Images A1.1-A1.4 show the user interface and the underlying code. The general flow of the code is as follows:

1. Gather Inputs using the UI:
    a. Acceleration, Deceleration, Return Acceleration, Return Deceleration
    b. Velocity 1, Velocity 2, Return Velocity,
    c. Total Travel, Travel before Vel1->Vel2
2. Convert inputs to be relevant to the stepper motor:
    a. $\text{Degrees}_{\text{crucible}} / 360_{\text{degrees per revolution}} * (7.33 * 50)_{\text{gear ratios}}$

3. Concatenate Double (converted inputs) and String (predefined) variables into a String formatted correctly to be sent as a serial command.
    a. Example: Acceleration =10 degrees/s^2 * 360 * 7.33 * 50 = 10.18
    b. “AC” + “10.18” => “AC10.18”
4. Send serial commands to the stepper motor using the VISA VI
    a. A list of commands can be found in the Host Command Reference
        i. http://www.applied-motion.com/sites/default/files/hardware-manuals/HostCommandReference_920-0002K.pdf

Figure A1.1: User interface for Autopour VI - input sliders and operation buttons/toggles.

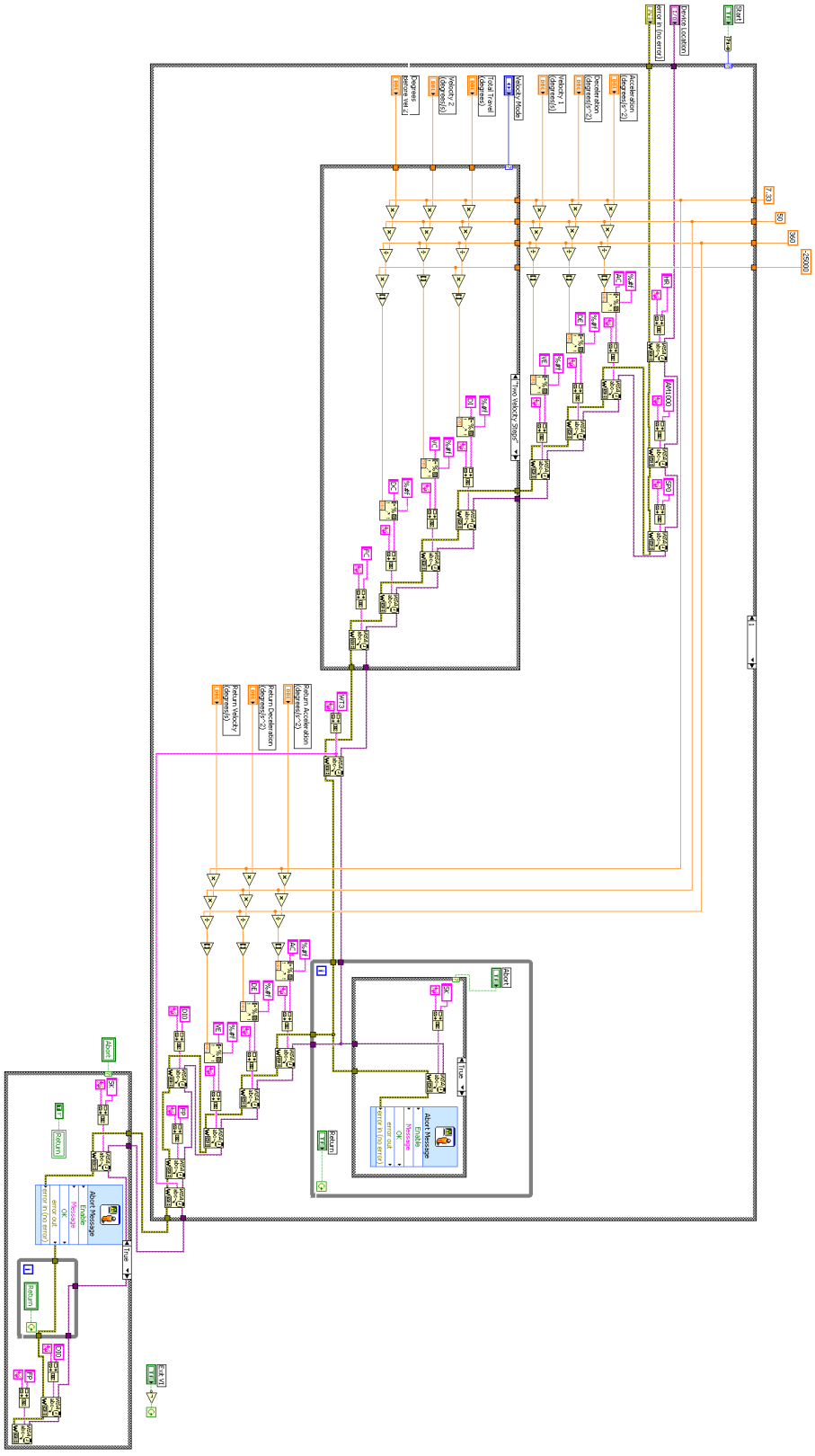

Figure A1.2: Entirety of Autopour VI, demonstrating the flow of commands.

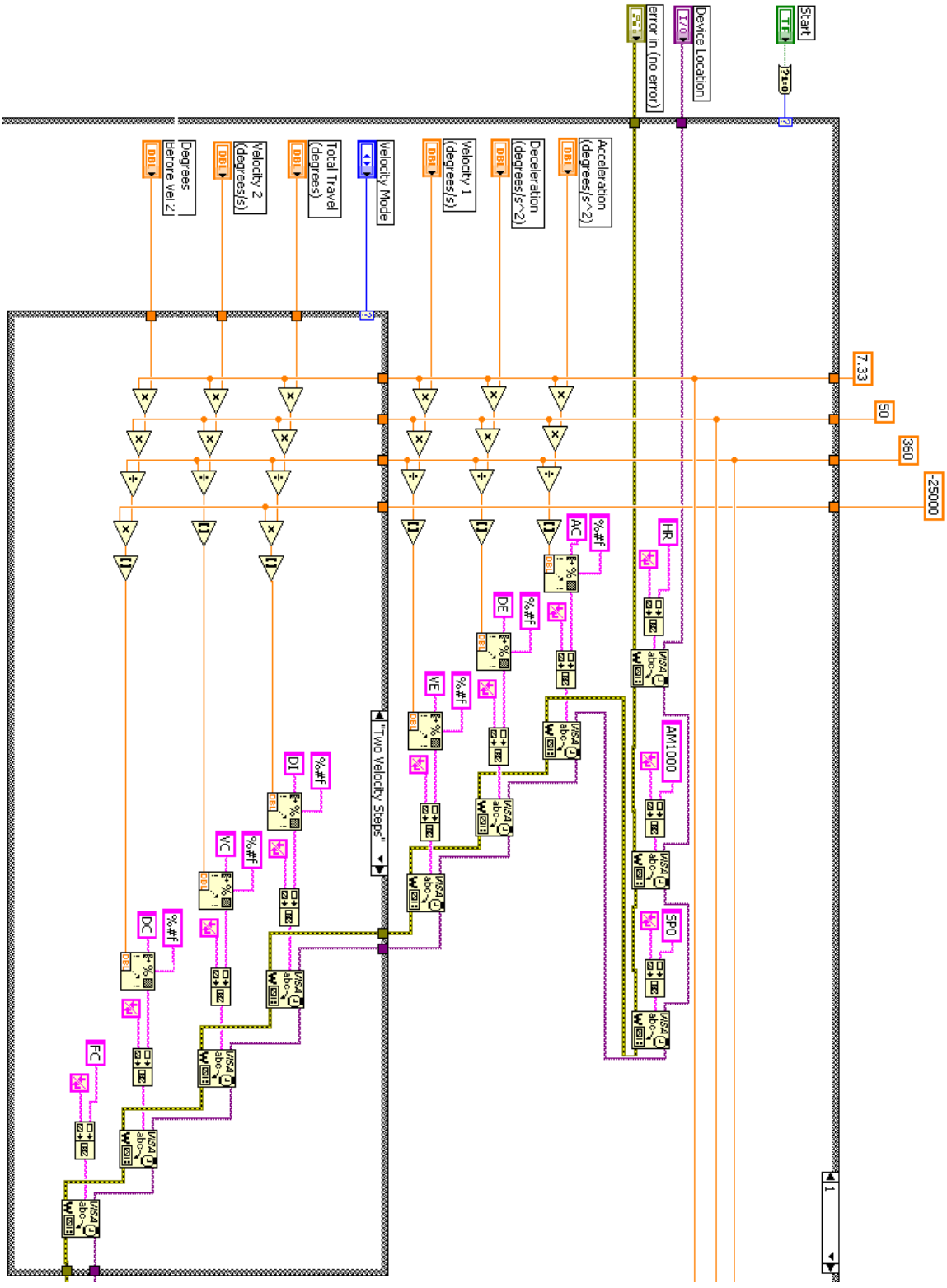

Figure A1.3: Upper left corner of VI - inputs, concatenation and serial command writing.

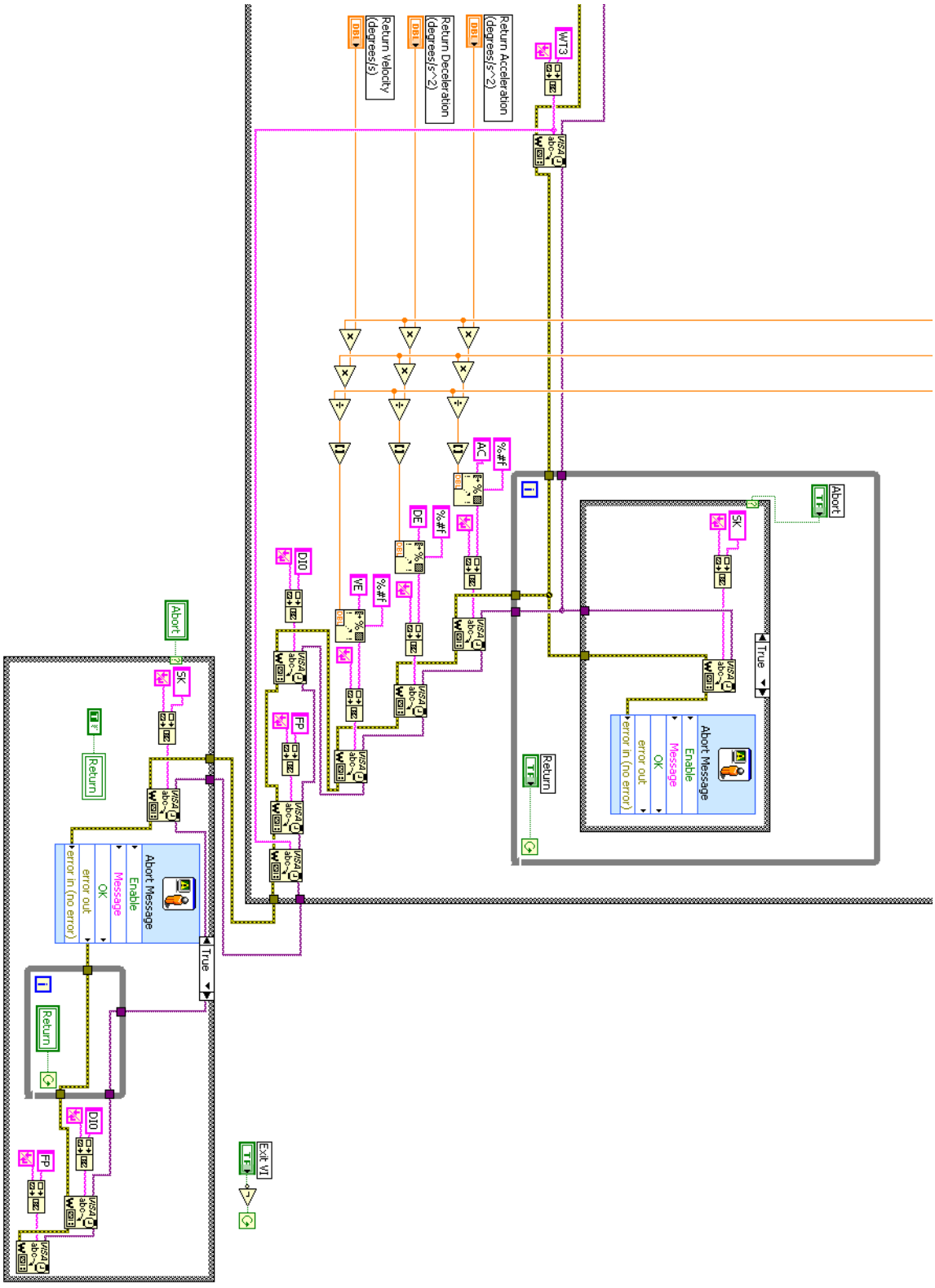

Figure A1.4: Lower right corner of VI - abort loops and the return toggle code

A.2: Al-Sc Precipitation and Growth Model

The following code is a Matlab program largely based on the KWN model, adapted for the purposes of determining strengthening evolution during aging to determine optimal heat treatments. A description of the reasoning behind this code and of the operation and usefulness can be found in Chapter 6.

```
%Kyle Deane
%Al-Sc alloy precipitate growth prediction

clear,clc


%initializing variables

Binprecippercum=zeros(1,10000000);
Binmatpercum=zeros(1,10000000);
xmatrix=zeros(1,10000000);
rcritnuc=zeros(1,10000000);
totaltime=zeros(1,10000000);
cooksteptime=zeros(1,10000000);
nucrate=zeros(1,10000000);
numprecippercum=zeros(1,10000000);
aveBperprecip=zeros(1,10000000);
averad=zeros(1,10000000);
steprad=zeros(1,10000000);
phasefraction=zeros(1,10000000);
precipedgespacing=zeros(1,10000000);
solidsolution=zeros(1,10000000);
ordered=zeros(1,10000000);
orowan=zeros(1,10000000);
mismatch=zeros(1,10000000);
coherency=zeros(1,10000000);
mismatchandcoherency=zeros(1,10000000);
strength=zeros(1,10000000);
dominantmechanism=zeros(1,10000000);
```

```
Z=zeros(1,10000000);
Bstar=zeros(1,10000000);
dGv=zeros(1,10000000);
numberofnucleations=zeros(1,10000000);


%Set initial counters


totalbinnumber=1;
cookstepcount=1;
totaltime(totalbinnumber)=0;


%Definition of modeling parameters

minunitcells=2; %minimum number of unit cells for a
precip
                %to be considered a precip
unitless
dx=0.000000000000001; %change in composition used in
Gibbs
        %energy equations to determine solvus
composition       unitless


%Definition of universal constants

gas=8.314;
avo=6.0221413e23; %avogadro's number
boltz=gas/avo; %boltzmann's constant


%definition of heat treatment process parameters

filename='Al-Sc Multistep Heat Treatments.xlsx';
sheet = 'Al-0.04at%Sc';
excelshortener=10;
timestep=1;

xmatrix(totalbinnumber)=0.0004; %initial matrix
composition,
                                %in fraction solute
unitless
```

```
cooktemp=[25,200,250,300,325,350,375,400,425,450,475,50
0];
    %Set temps for each heat treat step
C
cooktime=[1,10800,10800,10800,10800,10800,10800,10800,1
0800,10800,10800,10800];
    %Set times for heat treat steps
s
cooksteps=12; %number of heat treat steps considered,
taken
    %from cooktemp and cooktime arrays
unitless
taufract(1)=1; %initial fraction of incubation time
completed.
    %0 means fully homogenous, 1 means solute atoms are
fully
    %clustered and nucleation can start immediately
unitless


%Definition of material constants

Dcoeff=0.000531;
Ef=1.05; %vacancy formation energy next to Sc atoms
eV/vacancy
Em=0.63; %migration energy of Sc in Al with Si present,
         %would be 0.45 with Si, 0.74 without Si
eV/atom
f=0.7815; %dimensionless correlation factor (0.7815 for
FCC)    unitless
GoBb=3347; %see next line
J/mol
GoBm=-0.02; %components of calculated gibbs free energy
    %for pure B, assuming gibbs free energy of pure A
is 0.
    %Usage as:    GoB=GoBb+GoBm*tempk
J/mol/K
dGfpb=-34791;%see next line
J/mol
dGfpm=2.789; %components of calculated gibbs free
energy
    %for the formation of precipitate phase.
```

```
    %Usage as:    dGfp=dGfpb+dGfpm*tempk
J/mol/K
Aob=-74918;%see next line
J/mol
Aom=-11.021; %components of the coefficient for
calculating
    %excess Gibbs free energy for the solution phase.
    %Usage in FCC as:  xAxB(Ao); Ao=Aob+Aom*tempk
J/mol/K
ap=0.0000000004103; %lattice parameter for the
precipitate      m
totalatomsap=4; %number of atoms per unit cell of
precipitate   unitless
xp=0.25; %precipitate composition in fraction solute
unitless
am=0.00000000040496; %lattice parameter for matrix
phase        m
totalatomsam=4; %number of atoms per unit cell of
matrix        unitless
v=0.345; %poisson's ratio for FCC aluminum
unitless
orientationfactor=3.06;%Taylor mean orientation factor,
M       unitless
burgers=0.000000000286;%magnitude of the Burgers vector
m
apbenergy=0.5;%antiphase boundary energy for (111)
plane        J/m^2
gm=25400000000; %shear modulus of matrix (pure Al)
Pa
gp=68000000000; %shear modulus of precipitate
Pa
isurfen=0.096; %initial/nucleation surface energy
J/m^2
fsurfen=0.158; %final/coarsening surface energy
J/m^2
radsurfenchange=0.000000005; %radius of precipitate
above       m
        %which fsurfen becomes the surface energy


%Variables calculated from inputs

wconst=5*burgers;
```

```
misfit=(ap-am)/am; %difference in lattice parameters
between
        %matrix and precipitate
unitless
molvol=(avo*(ap^3))/totalatomsap; %molar volume of
atoms in
        %the precipitate phase
m^3/mol
dm=(gm*(1+v))/(1-2*v); %constants for use in dGs
equation
dp=(gp*(1+v))/(1-2*v); %constants for use in dGs
equation
dissolutionsize=ap*(minunitcells*3/(4*pi))^(1/3);
%radius
        %below which precipitates aren't really
precipitates    m^3
msurfen=(fsurfen-isurfen)/radsurfenchange; %slope of a
linear
        %correlation between radius and surface energy
at
        %precipitate radii below radsurfenchange


%Nucleation sites

nvinitial=xmatrix(totalbinnumber)*totalatomsam/(am^3);
        %determines the number of nucleation sites per
m^3,
        %assuming complete initial supersaturation and
that
        %each solute atom is a nucleation site
#/m^3
Binmatpercum(totalbinnumber)=nvinitial;


%Constants to minimize # of operations in nested loops
to increase speed

xarconst=2*molvol/(gas);
Binprecippercumconst=4/3*pi*totalatomsap*xp/((ap)^3);
    %these first two constants are in the most nested
loop and cut runtime
    %by ~66% when implemented
```

```
averadconst=3*ap^3/(4*pi*totalatomsap*xp);

solidsolutionconst=orientationfactor*(3/8)^(2/3)*((1+v)
/(1-
v))^(4/3)*(wconst/burgers)^(1/3)*gm*abs(misfit)^(4/3);
orderedconst=0.44*orientationfactor*apbenergy/burgers;
mismatchconst=orientationfactor*0.0078*(gp-gm)^(3/2);
coherencyconst=orientationfactor*2*gm*((ap-
am)/am)^(3/2);
orowanconst=0.4*orientationfactor*gm*burgers;
    %these last 5 constants took off another ~5% of the
remainder... not
    %much, but then they were less nested so it makes
sense

%Loop for each new heat treatment step

while cookstepcount<=cooksteps

    cooksteptime(totalbinnumber)=0;


    %temperature dependent calculated variables

    tempk=cooktemp(cookstepcount)+273; %converts
current temp to Kelvin
    %Diff=Dcoeff*exp(-Ea/(gas*tempk)); %calculated
diffusion rate
    Diff=Dcoeff*f*exp((-(Ef+Em)*1.60217646*10^(-
19))/(boltz*tempk));
        %calculated diffusion rate
    GoB=GoBb+GoBm*tempk; %calculated gibbs free energy
of
        %pure B, assuming gibbs free energy of pure A
is 0
    GoA=0; %gibbs free energy of pure A, set to 0
    dGfp=dGfpb+dGfpm*tempk; %gibbs free energy of the
        %precipitate phase
    xsolvuscheck=xp/2; %initial guess for the solvus
        %composition, set at half xp
    xsolvusstep=xsolvuscheck/2; %distance (from the
initial guess) to check
```

```
    %calculation of solvus composition
    %For each iteration, this loop calculates the
slopes of the tie lines
    %between the gibbs free energy of the matrix and
precipitate phases for
    %three different matrix compositions. It then
chooses the composition
    %that resulted in the smallest slope as the new
guess and halves the
    %distance between guesses before creating a new low
and high guess for
    %the next iteration. The loop ends when the step
size is below 1e-10

    while xsolvusstep>0.0000000001;
        gsolvuscheck=GoA*(1-
xsolvuscheck)+GoB*xsolvuscheck+gas*tempk*(xsolvuscheck*
log(xsolvuscheck))+(1-xsolvuscheck)*log(1-
xsolvuscheck)+xsolvuscheck*(1-
xsolvuscheck)*(Aob+Aom*tempk);
            %calculates the gibbs free energy of the
currently guessed
            %solvus composition along the matrix phase
curve
        msolvuscheck=(dGfp-gsolvuscheck)/(xp-
xsolvuscheck); %calculates
            %slope of the tie line between gibbs free
energies of the
            %precipitate phase and the guessed solvus
composition


        %same as above, but with lower guess (initially
half distance
        %from middle guess to A)

        xsolvuschecklow=xsolvuscheck-xsolvusstep;
        gsolvuschecklow=GoA*(1-
xsolvuschecklow)+GoB*xsolvuschecklow+gas*tempk*(xsolvus
checklow*log(xsolvuschecklow))+(1-
xsolvuschecklow)*log(1-
```

```
xsolvuschecklow)+xsolvuschecklow*(1-
xsolvuschecklow)*(Aob+Aom*tempk);
        msolvuschecklow=(dGfp-gsolvuschecklow)/(xp-
xsolvuschecklow);


        %same as above, but with higher guess
(initially half distance
        %from middle guess to precipitate composition)

        xsolvuscheckhigh=xsolvuscheck+xsolvusstep;
        gsolvuscheckhigh=GoA*(1-
xsolvuscheckhigh)+GoB*xsolvuscheckhigh+gas*tempk*(xsolv
uscheckhigh*log(xsolvuscheckhigh))+(1-
xsolvuscheckhigh)*log(1-
xsolvuscheckhigh)+xsolvuscheckhigh*(1-
xsolvuscheckhigh)*(Aob+Aom*tempk);
        msolvuscheckhigh=(dGfp-gsolvuscheckhigh)/(xp-
xsolvuscheckhigh);


        %select the composition with the highest slope
out of the guess and
        %lower step (slopes are neg so the highest
slope is most shallow)

        if msolvuschecklow>msolvuscheckhigh
            msolvuscheck=msolvuschecklow;
            xsolvuscheck=xsolvuschecklow;
        end


        %select the composition with the highest slope
between the winner
        %of the last block and the higher step

        if msolvuscheckhigh>msolvuscheck
            msolvuscheck=msolvuscheckhigh;
            xsolvuscheck=xsolvuscheckhigh;
        end
```

```
        %halves the checkstep size, to focuse in on the
solvus composition

        xsolvusstep=xsolvusstep/2;

    end


    %sets the newly found solvus composition

    xsolvus(cookstepcount)=xsolvuscheck;


    %loop for every timestep within this heat treatment
step, nucleating,
    %growing, and dissolving precipitates

    while
cooksteptime(totalbinnumber)<cooktime(cookstepcount)


        %determine the gibbs free energy of
compositions slightly above
        %and below the matrix composition, and use
these values to find the
        %slope and intercept of a tangential line to
the energy curve. This
        %tangential line is used to determine the
change in gibbs energy
        %due to the formation of precipitate volume

        xmathigh=xmatrix(totalbinnumber)+dx;
        xmatlow=xmatrix(totalbinnumber)-dx;
        gmatrix=GoA*(1-
xmatrix(totalbinnumber))+GoB*xmatrix(totalbinnumber)+ga
s*tempk*(xmatrix(totalbinnumber)*log(xmatrix(totalbinnu
mber))+(1-xmatrix(totalbinnumber))*log(1-
xmatrix(totalbinnumber)))+xmatrix(totalbinnumber)*(1-
xmatrix(totalbinnumber))*(Aob+Aom*tempk);
        gmathigh=GoA*(1-
xmathigh)+GoB*xmathigh+gas*tempk*(xmathigh*log(xmathigh
)+(1-xmathigh)*log(1-xmathigh))+xmathigh*(1-
xmathigh)*(Aob+Aom*tempk);
```

```
        gmatlow=GoA*(1-
xmatlow)+GoB*xmatlow+gas*tempk*(xmatlow*log(xmatlow)+(1
-xmatlow)*log(1-xmatlow))+xmatlow*(1-
xmatlow)*(Aob+Aom*tempk);
        mmatrix=(gmathigh-gmatlow)/(xmathigh-xmatlow);
        bmatrix=gmatrix-
mmatrix*xmatrix(totalbinnumber);
        Gpm=mmatrix*xp+bmatrix;
        dGv(totalbinnumber)=(dGfp-Gpm)/molvol;
        dGs=3*misfit^2*dp*(1-1/(1+(3*dm*(1-
v))/(dp*(1+v))-dm/dp));


        %calculate the critical radius of nucleation,
based on surface
        %energy, which can vary at very low radii due
to preferential
        %formation of the most preferential interfaces.
Here it is assumed
        %to vary linearly up to a radius of
radsurfenchange

        rcritnuc(totalbinnumber)=-
2*isurfen/(dGv(totalbinnumber)+dGs+2*msurfen);

        if
rcritnuc(totalbinnumber)>=radsurfenchange||rcritnuc(tot
albinnumber)<0
            rcritnuc(totalbinnumber)=-
2*fsurfen/(dGv(totalbinnumber)+dGs);
        end


        %if dGv + dGs is neg, the crit radius will be
calculated as neg,
        %which should not be rewritten as dissolution
size, as
        %precipitation is extremely unlikely in this
scenario.

        if rcritnuc(totalbinnumber)<0

rcritnuc(totalbinnumber)=rcritnuc(totalbinnumber-1);
```

```
        end

        %Reset critical radius to the minimum possible
precipitate size if
        %it is impossibly small, so only realistic
precipitates form

        if rcritnuc(totalbinnumber)<dissolutionsize
            rcritnuc(totalbinnumber)=dissolutionsize;
        end


        %Calculate surface energy for precipitates with
critical radius.
        %Done now in case dissolution size was above
radsurfenchange and
        %rcritnuc was just reset

        if rcritnuc(totalbinnumber)>=radsurfenchange
            surfen=fsurfen;
        else

surfen=(msurfen*rcritnuc(totalbinnumber)+isurfen);
        end


        %Calculate nucleation of precips for the
current timestep

        atomvolm=(1-
xmatrix(totalbinnumber)/xp)/totalatomsam*(am^3)+xmatrix
(totalbinnumber)/xp*(ap^3)/totalatomsap;
            %calculating the average volume per atom in
the matrix,
            %assuming identical crystal structures and
that the lattice
            %stretches around each B atom as if it was
in precipitate phase

Z(totalbinnumber)=atomvolm*(dGv(totalbinnumber)+dGs)^2/
(8*pi*sqrt(surfen^3*boltz*tempk));
            %calculating the Zeldovich nonequilibrium
factor
```

```
Bstar(totalbinnumber)=(16*pi*surfen^2*xmatrix(totalbinn
umber)*Diff)/((dGv(totalbinnumber)+dGs)^2*(ap)^4);
            %calculating beta star, rate of atomic
attachment to an embryo

tau=(8*boltz*tempk*surfen*(ap)^4)/(atomvolm^2*(dGv(tota
lbinnumber)+dGs)^2*Diff*xmatrix(totalbinnumber));
            %calculating the incubation time required
for nucleation

nucrate(totalbinnumber)=(Binmatpercum(totalbinnumber)-
(4*xsolvus(cookstepcount))/(am^3))*Z(totalbinnumber)*Bs
tar(totalbinnumber)*exp((-
4*pi*surfen*rcritnuc(totalbinnumber)^2)/(3*boltz*tempk)
)*exp(-
tau/(tau*taufract(cookstepcount)+cooksteptime(totalbinn
umber)));
            %calculating the homogeneous nucleation
rate        #/m^3/s

numberofnucleations(totalbinnumber)=timestep*nucrate(to
talbinnumber);
            %calculating the number of nucleations this
            %timestep, more useful if timestep is
variable      #/m^3


        %If precipitates were formed during this time
step: store radius
        %(critical radius), calculate # of B atoms used
for each
        %precipitate and for the sum of all newly
formed precips

        if
numberofnucleations(totalbinnumber)>=1&&rcritnuc(totalb
innumber)>=dissolutionsize


steprad(totalbinnumber)=rcritnuc(totalbinnumber);
                %the radius of the precipitates formed
at this step
```

```
Binprecippercum(totalbinnumber)=Binprecippercumconst*nu
mberofnucleations(totalbinnumber)*steprad(totalbinnumbe
r)^3;
                %the amount of B atoms in all precips
per m^3
            numprecippercum(totalbinnumber) =
numberofnucleations(totalbinnumber);
                %number of precips per m^3, incomplete
at this point
                %because preexisting precips haven't
been added yet

        else

            steprad(totalbinnumber)=0;

        end


        %loop to calculate coarsening behavior of all
previously formed
        %precipitates, starting with first historical
timestep with
        %nucleation

        Iteratingbinnumber=1;

        while Iteratingbinnumber<totalbinnumber

            if
steprad(Iteratingbinnumber)>=dissolutionsize


                %if radius of precipitates nucleated at
time
                %Iteratingbinnumber is physically
possible, the precipitate
                %will grow/shrink depending on Gibbs-
Thomson relations

                if
steprad(Iteratingbinnumber)>=radsurfenchange
```

```
                    surfen=fsurfen;
                else

surfen=(msurfen*steprad(Iteratingbinnumber)+isurfen);
                end


xar=xsolvus(cookstepcount)*exp(xarconst*surfen/(tempk*s
teprad(Iteratingbinnumber)));
                    %the effective equilibrium
composition at edge of
                    %precipitates in this bin,
accounting for gibbs-thomson

steprad(Iteratingbinnumber)=steprad(Iteratingbinnumber)
+timestep*(Diff*(xmatrix(totalbinnumber)-xar))/((xp-
xar)*steprad(Iteratingbinnumber));
                    %calculated radius of precipitates
in this bin after
                    %the current timestep
                numprecippercum(totalbinnumber) =
numprecippercum(totalbinnumber)+numberofnucleations(Ite
ratingbinnumber);

            else

                %dissolve precipitates if they are
below the minimal
                %physical precipitate size.

                steprad(Iteratingbinnumber)=0;
            end


Binprecippercum(totalbinnumber)=Binprecippercum(totalbi
nnumber)+Binprecippercumconst*numberofnucleations(Itera
tingbinnumber)*steprad(Iteratingbinnumber)^3;

            %look at the next historical timestep and
loop

            Iteratingbinnumber=Iteratingbinnumber+1;
```

```
        end


        %Calculate number of B atoms still in the
matrix after all
        %nucleation/coarsening and calculate the new
matrix composition

        if numprecippercum(totalbinnumber)>0

            aveBperprecip(totalbinnumber) =
Binprecippercum(totalbinnumber) /
numprecippercum(totalbinnumber);

        else
            aveBperprecip(totalbinnumber)=0;
        end


averad(totalbinnumber)=(averadconst*aveBperprecip(total
binnumber))^(1/3);

        Binmatpercum(totalbinnumber)=nvinitial-
(Binprecippercum(totalbinnumber));

xmatrix(totalbinnumber+1)=Binmatpercum(totalbinnumber)*
(am^3)/totalatomsam;

Binmatpercum(totalbinnumber+1)=Binmatpercum(totalbinnum
ber);

        %strengthening calculations

        phasefraction(totalbinnumber)=(xmatrix(1)-
xmatrix(totalbinnumber+1))/xp;

precipedgespacing(totalbinnumber)=averad(totalbinnumber
)*(sqrt(2*pi/(3*phasefraction(totalbinnumber)))-pi/2);

solidsolution(totalbinnumber)=solidsolutionconst*xmatri
x(totalbinnumber)^(2/3);
```

```
ordered(totalbinnumber)=orderedconst*sqrt(phasefraction
(totalbinnumber));

mismatch(totalbinnumber)=mismatchconst*sqrt(phasefracti
on(totalbinnumber)/gm)*(averad(totalbinnumber)/burgers)
^0.275;

coherency(totalbinnumber)=coherencyconst*sqrt(averad(to
talbinnumber)*phasefraction(totalbinnumber)/burgers);

mismatchandcoherency(totalbinnumber)=mismatch(totalbinn
umber)+coherency(totalbinnumber);

        if averad(totalbinnumber)>0

orowan(totalbinnumber)=(orowanconst*log(2*averad(totalb
innumber)/burgers))/(pi*precipedgespacing(totalbinnumbe
r)*sqrt(1-v));
        else

            %if no precipitates have formed, averad is
0, and the orowan
            %equation returns NaN because of log(0).
Therefore we bypass it
            %and set orowan strength to 0 so the code
can handle it

            orowan(totalbinnumber)=0;
        end


        %Determine which strengthening mechanism is
dominant (represented
        %by 1, 2, and 3) and record predicted effective
strengthening

        if
mismatchandcoherency(totalbinnumber)<orowan(totalbinnum
ber)&&mismatchandcoherency(totalbinnumber)<ordered(tota
lbinnumber)
```

```
strength(totalbinnumber)=solidsolution(totalbinnumber)+
mismatchandcoherency(totalbinnumber);
            dominantmechanism(totalbinnumber)=1;
        elseif
ordered(totalbinnumber)<orowan(totalbinnumber)

strength(totalbinnumber)=solidsolution(totalbinnumber)+
ordered(totalbinnumber);
            dominantmechanism(totalbinnumber)=2;
        else

strength(totalbinnumber)=solidsolution(totalbinnumber)+
orowan(totalbinnumber);
            dominantmechanism(totalbinnumber)=3;
        end

        totalbinnumber=totalbinnumber+1;


totaltime(totalbinnumber)=totaltime(totalbinnumber-
1)+timestep;

cooksteptime(totalbinnumber)=cooksteptime(totalbinnumbe
r-1)+timestep;

        %Loop unless the time for this heat treatment
step has expired

    end

    %Move to the next heat treatment step and loop
unless all of the heat
    %treatment steps have been run


taufract(cookstepcount+1)=taufract(cookstepcount)+cooks
teptime(totalbinnumber)/tau;

    outtab(cookstepcount,1)=cooktemp(cookstepcount);
    outtab(cookstepcount,2)=totaltime(totalbinnumber);
    outtab(cookstepcount,3)=xmatrix(totalbinnumber);
    outtab(cookstepcount,4)=taufract(cookstepcount+1);
```

```
    outtab(cookstepcount,5)=strength(totalbinnumber-1);

outtab(cookstepcount,6)=dominantmechanism(totalbinnumbe
r-1);

outtab(cookstepcount,7)=numprecippercum(totalbinnumber-
1);
    outtab(cookstepcount,8)=averad(totalbinnumber-1);
    outtab(cookstepcount,9)=rcritnuc(totalbinnumber-1);

    clc

End_of_Step_Table=array2table(outtab,'VariableNames',{'
Temp','Time','Matrix_Composition','Fraction_Tau_Complet
ed','Strength','Mechanism','Precipitates_per_m3','Avera
ge_Radius','Critical_Radius'})
    cookstepcount=cookstepcount+1; %moves to the next
heat treatment step

end

%For each array to be plotted, set all zeros to NaN so
they don't plot as 0

xmatrix(~xmatrix)=nan;
averad(~averad)=nan;
nucrate(~nucrate)=nan;
numprecippercum(~numprecippercum)=nan;
mismatchandcoherency(~mismatchandcoherency)=nan;
solidsolution(~solidsolution)=nan;
ordered(~ordered)=nan;
orowan(~orowan)=nan;
strength(~strength)=nan;

%Create a condensed matrix for the data and export it
to excel

row=2;
Iteratingbinnumber=1;

while Iteratingbinnumber<=totalbinnumber

    condenseddata(row,1)=totaltime(Iteratingbinnumber);
```

```
    condenseddata(row,2)=xmatrix(Iteratingbinnumber);
    condenseddata(row,3)=averad(Iteratingbinnumber);
    condenseddata(row,4)=nucrate(Iteratingbinnumber);

condenseddata(row,5)=numprecippercum(Iteratingbinnumber
);

condenseddata(row,6)=solidsolution(Iteratingbinnumber);

condenseddata(row,7)=mismatchandcoherency(Iteratingbinn
umber);
    condenseddata(row,8)=ordered(Iteratingbinnumber);
    condenseddata(row,9)=orowan(Iteratingbinnumber);
    condenseddata(row,10)=strength(Iteratingbinnumber);

condenseddata(row,11)=dominantmechanism(Iteratingbinnum
ber);


Iteratingbinnumber=Iteratingbinnumber+excelshortener;
    row=row+1;

end

xlswrite(filename,condenseddata,sheet)
xlswrite(filename,{'Total Time (s)','Concentration (at%
Sc)','Average Radius (nm)','Nucleation Rate
(#/s/m^3)','Number Density (#/m^3)','Solid Solution
Strength (Pa)','Mismatch and Coherency Strength
(Pa)','Ordered Strength (Pa)','Orowan Strength
(Pa)','Total Strength (Pa)','Dominant
Mechanism'},sheet)

Plot the chosen arrays (can choose other arrays as
suits your purpose)

figure

plot(totaltime,xmatrix)
title('Hist Matrix Sc Conc')
xlabel('Time (s)')
ylabel('Sc Conc (at%)')
```

```
set(gcf, 'units','normalized','outerposition',[0 0 1
1]); %Maximize figure.

figure

plot(totaltime,averad)
title('Hist Avg Radius (m)')
xlabel('Time (s)')
ylabel('Radius (m)')

set(gcf, 'units','normalized','outerposition',[0 0 1
1]); %Maximize figure.

figure

plot(totaltime,nucrate)
title('Hist Nuc Rate (per m3)')
xlabel('Time (s)')
ylabel('Nucleation Rate (/s/m^3)')

set(gcf, 'units','normalized','outerposition',[0 0 1
1]); %Maximize figure.

figure

plot(totaltime,numprecippercum)
title('Hist Number of Precips')
xlabel('Time (s)')
ylabel('Precipitates (/m^3)')

set(gcf, 'units','normalized','outerposition',[0 0 1
1]); %Maximize figure.

figure

plot(totaltime,solidsolution)
title('Solid Solution Strength')
xlabel('Time (s)')
ylabel('Strength (Pa)')

set(gcf, 'units','normalized','outerposition',[0 0 1
1]); %Maximize figure.

figure
```

```
plot(totaltime,mismatchandcoherency)
title('Mismatch and Coherency Strength')
xlabel('Time (s)')
ylabel('Strength (Pa)')

set(gcf, 'units','normalized','outerposition',[0 0 1
1]); %Maximize figure.

figure

plot(totaltime,ordered)
title('Ordered Strength')
xlabel('Time (s)')
ylabel('Strength (Pa)')

set(gcf, 'units','normalized','outerposition',[0 0 1
1]); %Maximize figure.

figure

plot(totaltime,orowan)
title('Orowan Strength')
xlabel('Time (s)')
ylabel('Strength (Pa)')

set(gcf, 'units','normalized','outerposition',[0 0 1
1]); %Maximize figure.

figure

plot(totaltime,solidsolution,'y',totaltime,mismatchandc
oherency,'r',totaltime,ordered,'g',totaltime,orowan,'b'
)
title('Precipitation Strength')
xlabel('Time (s)')
ylabel('Strength (Pa)')

set(gcf, 'units','normalized','outerposition',[0 0 1
1]); %Maximize figure.

figure

plot(totaltime,strength)
```

```
title('Precipitation Strength')
xlabel('Time (s)')
ylabel('Strength (Pa)')

set(gcf, 'units','normalized','outerposition',[0 0 1
1]); %Maximize figure.
```

A.3: Thermocalc Ternary Driving Force Data Extractor

Thermocalc has a great deal of useful data that can be difficult to ouput in an easily useful manner. In order to extract a function dictating the driving forces of precipitation in ternary alloys, a method has been developed to rapidly output relevant data using a Thermocalc console mode program into multiple CSV files (A.3.1). These files are then run through an Excel VBA program (A.3.2) that delimits them, extracts the data, closes them, and organizes the data for ease of polynomial fitting in a third program. Bivariate polynomial fitting is performed in Mathematica for each temperature (A.3.3), and then the resulting functions are solved to adjust for temperature change.

A.3.1: Thermocalc - Driving Force Output

```
@@ Go to the Data module to get started
go data
@@ Switch the database to the latest Al one
switch
tcal4
@@ Define the system
def-sys
al sc zr
@@ 'Reject' all of the phases at first, and then 'restore' the ones we are interested in
rej pha *
res pha fcc_a1 al3sc al3zr_d023
@@ Tell TC to get the data for the defined system and phases
```

```
get
@@ Go to the Poly Module, for defining and calculating equilibriums
go pol
@@ Change the state of the precipitate phases to dormant, as the driving force depends
@@ on the solution atoms being entirely in solid solution
ch-st pha
al3sc al3zr_d023
dormant
@@ Set the conditions of the system, (x(zr)) means molar fraction of Zr in the alloy
s-c
n=1 p=101325 t=773.15 x(sc)=0.1e-2 x(zr)=0.0001
@@Define the driving force functions so they will output recognisable results
ent-sym funct df1=-8.3144*T*DGV(al3sc)

ent-sym funct df2=-8.3144*T*DGV(al3zr_d023)

@@ Compute equilibrium for the system
co-eq
@@ Set up compositional stepping of 1 solute atom for the simulation
s-a-v
1
x(sc)
0
0.004

@@ Now begin stepping
step

@@ Create a table for this temp with the variables of interest (composition, df, etc)
enter table
awesome
x(sc) x(zr) df1 df2

@@ Call the table and save it to a text file
tab
awesome
file \\mtucifs3.iso.mtu.edu\home\AlScZr\773_0001

@@ Repeat! I just made 40 variations of this code in Notepad (changing the two
@@ instances of "0001"), and then copy pasted it into console mode of TC. Then I
@@ would Ctrl+F, Replace all "773" with "748", and copy/paste it in again. This makes
@@ a large number of files.

go data
switch
```

```
tcal4
def-sys
al sc zr
rej pha *
res pha fcc_a1 al3sc al3zr_d023
get
go pol
ch-st pha
al3sc al3zr_d023
dormant
s-c
n=1 p=101325 t=773.15 x(sc)=0.1e-2 x(zr)=0.0002
ent-sym funct df1=-8.3144*T*DGV(al3sc)

ent-sym funct df2=-8.3144*T*DGV(al3zr_d023)

co-eq
s-a-v
1
x(sc)
0
0.004

step

enter table
awesome
x(sc) x(zr) df1 df2

tab
awesome
file \\mtucifs3.iso.mtu.edu\home\AlScZr\773_0002

(etc)
```

A.3.2: Excel VBA - Combine and rearrange TC data

```
Sub Importer()
    'This sub imports and combines all of the data from the Thermocalc files that
    were 'generated using the code in A.3.1. After this sub is ran in a workbook
    (which does not 'have to be blank, but does have to have a "Sheet1") which shares
    a location path with the 'Thermocalc files, that worksheet will accumulate all of
    the data. The next sub, 'Organizer(), is used to organize the data perfectly for use
    in Mathematica.
```

```
Dim sPath As String
Dim temp(1 To 11) As Integer
Dim ws As Worksheet
        'Turn off alerts and updating, so the program runs faster and doesn't crash
Application.DisplayAlerts = False
Application.ScreenUpdating = False

        'Delete all previously created sheets and data to make room for the next results
For Each ws In Worksheets
If ws.Name <> "Sheet1" Then ws.Delete
Next

        'List the temperatures of interest so they can be recorded properly
temp(1) = 473
temp(2) = 523
temp(3) = 573
temp(4) = 598
temp(5) = 623
temp(6) = 648
temp(7) = 673
temp(8) = 698
temp(9) = 723
temp(10) = 748
temp(11) = 773


        'This is the one's digit of the concentration of the second solute atom (the addition
        'that is different in every TC output file). It is separated from the ten's digit to
        'make calling filenames, etc easier (x10e-4 atomic fraction)
concones = 1
        'This is the ten's digit of the second solute concentration (x10e-4 atomic fraction)
conctens = 0
        'This is the concentration of second solute addition in the file that is currently
being worked on, (x10e-4 atomic fraction)
conc = concones + 10 * conctens
        'This is the max concentration of solute addition observed (x10e-4 at. fraction)
maxconc = 40
        'Counters for keeping track of the different temperatures/data/etc
tempcount = 1
maxtempcount = 11
columncount = 2

        'This block adds the first sheets with names similar to the TC files
```

```
ThisWorkbook.Sheets.Add(After:=ThisWorkbook.Sheets(ThisWorkbook.Sheets.Count)).
Name = temp(tempcount) & " df1"
ThisWorkbook.Sheets.Add(After:=ThisWorkbook.Sheets(ThisWorkbook.Sheets.Count)).
Name = temp(tempcount) & " df2"

        'This block opens the first TC text file as a delimited spreadsheet
sPath = ThisWorkbook.Path & "\" & temp(tempcount) & "_00" & conctens & concones
Workbooks.OpenText Filename:= _
sPath, DataType:=xlDelimited, Space:=True, Local:=True

        'This block copies the first solute concentration column from the first TC file into
        'the main workbook
ActiveWorkbook.Sheets(temp(tempcount) & "_00" & conctens & concones).Columns(4).Copy  Destination:=ThisWorkbook.Sheets(temp(tempcount) & " df1").Columns(1)
ActiveWorkbook.Sheets(temp(tempcount) & "_00" & conctens & concones).Columns(4).Copy  Destination:=ThisWorkbook.Sheets(temp(tempcount) & " df2").Columns(1)

        'This loop is to ensure each temperature is represented
Do While tempcount <= maxtempcount

        'This loop is to cycle through all the required ten's digits
Do While conctens * 10 < maxconc

        'This loop is to cycle through the one's digits for every ten's digit
Do While concones <= 9

        'This calculates the concentration (x10e-4 atomic fraction) of the second solute for
        'the current operation
conc = concones + 10 * conctens

        'This kicks the code out of the loop as soon as the limit is reached
If conc > maxconc Then GoTo cheeseburger

        'This block opens the next TC file
sPath = ThisWorkbook.Path & "\" & temp(tempcount) & "_00" & conctens & concones
Workbooks.OpenText Filename:= _
sPath, DataType:=xlDelimited, Space:=True, Local:=True

        'This workbook copies the data out of the current TC file into the main workbook
ActiveWorkbook.Sheets(temp(tempcount) & "_00" & conctens & concones).Columns(9).Copy  Destination:=ThisWorkbook.Sheets(temp(tempcount) & " df1").Columns(columncount)
```

```
ActiveWorkbook.Sheets(temp(tempcount) & "_00" & conctens & concones).Columns(11).Copy Destination:=ThisWorkbook.Sheets(temp(tempcount) & " df2").Columns(columncount)

        'This iterates to the next column, so the importing data does not overlap
columncount = columncount + 1

        'This closes the TC file, so they do not build up and slow the computer
ActiveWorkbook.Close

        'This iterates the one's digit to move to the next higher concentration TC file
concones = concones + 1

Loop

        'This iterates the ten's digit to continue moving to higher concentration TC files
concones = 0
conctens = conctens + 1

Loop

        'This is where the 'goto' kicks you if maximum concentration is reached
cheeseburger:

        'This 'goto' ends the program if the max temp is done, to avoid errors
If tempcount = maxtempcount Then GoTo pizza

        'This block iterates to begin copying data from the next temperature
tempcount = tempcount + 1
concones = 1
conctens = 0
columncount = 2

        'This block adds sheets for the new temp after each precipitate phase's last sheet
ThisWorkbook.Sheets.Add(After:=ThisWorkbook.Sheets(temp(tempcount - 1) & " df1")).Name = temp(tempcount) & " df1"
ThisWorkbook.Sheets.Add(After:=ThisWorkbook.Sheets(temp(tempcount - 1) & " df2")).Name = temp(tempcount) & " df2"

        'This block brings in the next temperature's file
sPath = ThisWorkbook.Path & "\" & temp(tempcount) & "_00" & conctens & concones
Workbooks.OpenText Filename:= _
sPath, DataType:=xlDelimited, Space:=True, Local:=True
```

```
        'This block adds the column showing the first solute addition's concentration to
        'the newly made sheet
ActiveWorkbook.Sheets(temp(tempcount) & "_00" & conctens & concones).Columns(4).Copy Destination:=ThisWorkbook.Sheets(temp(tempcount) & "df1").Columns(1)
ActiveWorkbook.Sheets(temp(tempcount) & "_00" & conctens & concones).Columns(4).Copy Destination:=ThisWorkbook.Sheets(temp(tempcount) & "df2").Columns(1)

Loop

        'This is where the 'goto' kicks to when the last temperature has been fully finished
pizza:

        'This re-enables alerts and screenupdating
Application.DisplayAlerts = True
Application.ScreenUpdating = True

End Sub

Sub Organizer()
        'This sub takes the newly collected data straight from Importer() and organizes it
        'for function fitting in Mathematica (and to avoid overflowing Excel by having
        'too long of a column). This sub has a similar flow to the previous sub, so many of
        'the blocks will be left undescribed. See Importer() for more descriptions

Dim sPath As String
Dim temp(1 To 11) As Integer

Application.DisplayAlerts = False
Application.ScreenUpdating = False

temp(1) = 473
temp(2) = 523
temp(3) = 573
temp(4) = 598
temp(5) = 623
temp(6) = 648
temp(7) = 673
temp(8) = 698
temp(9) = 723
temp(10) = 748
temp(11) = 773

concones = 1
```

```
conctens = 0
conc = concones + 10 * conctens
maxconc = 40
tempcount = 1
maxtempcount = 11
columncount = 2


Do While tempcount <= maxtempcount

        'This block deletes 3 blank rows at the top that were imported from the TC files
ThisWorkbook.Sheets(temp(tempcount) & " df1").Rows(2).Delete
ThisWorkbook.Sheets(temp(tempcount) & " df1").Rows(3).Delete
ThisWorkbook.Sheets(temp(tempcount) & " df1").Rows(4).Delete
ThisWorkbook.Sheets(temp(tempcount) & " df2").Rows(2).Delete
ThisWorkbook.Sheets(temp(tempcount) & " df2").Rows(3).Delete
ThisWorkbook.Sheets(temp(tempcount) & " df2").Rows(4).Delete

        'This counter references row numbers, and the following loop aims at rearranging
        'the imported TC data from low concentration to high, as TC decides to take the
        'smallest concentrations and put them at the end of the data in reverse order.
i = 39

Do While i <= 55

        'This line adds a blank row in row 2, shifting all other rows down
ThisWorkbook.Sheets(temp(tempcount) & " df1").Rows(2).Insert shift:=xlShiftDown
        'This line cuts the target row and inserts it into te blank row just created at 2
ThisWorkbook.Sheets(temp(tempcount) & " df1").Cells(i, 1).EntireRow.Cut
Destination:=ThisWorkbook.Sheets(temp(tempcount) & " df1").Cells(3, 1)

        'This block does the same as the last, but for the driving force of the second solute
ThisWorkbook.Sheets(temp(tempcount) & " df2").Rows(2).Insert shift:=xlShiftDown
ThisWorkbook.Sheets(temp(tempcount) & " df2").Cells(i, 1).EntireRow.Cut
Destination:=ThisWorkbook.Sheets(temp(tempcount) & " df2").Cells(3, 1)

        'This iterates to the next offending row
i = i + 2

Loop

        'This block tidies up from the last operation and adds a header denoting which
        'concentration runs vertical and which horizontal (Sc and Zr in this example)
ThisWorkbook.Sheets(temp(tempcount) & " df1").Rows(2).Delete
ThisWorkbook.Sheets(temp(tempcount) & " df2").Rows(2).Delete
```

```
ThisWorkbook.Sheets(temp(tempcount) & " df1").Cells(1, 1).Value = "Sc\Zr"
ThisWorkbook.Sheets(temp(tempcount) & " df2").Cells(1, 1).Value = "Sc\Zr"

        'This loop adds the concentration of the second solute atom (Zr in the above
        'example) to the top row as column headers
Do While conctens * 10 < maxconc

Do While concones <= 9

conc = concones + 10 * conctens

If conc > maxconc Then GoTo cheeseburger

ThisWorkbook.Sheets(temp(tempcount) & " df1").Cells(1, columncount).Value = conc *
10 ^ -4
ThisWorkbook.Sheets(temp(tempcount) & " df2").Cells(1, columncount).Value = conc *
10 ^ -4

columncount = columncount + 1
concones = concones + 1

Loop

concones = 0
conctens = conctens + 1

Loop

cheeseburger:

If tempcount = maxtempcount Then GoTo pizza

tempcount = tempcount + 1
concones = 1
conctens = 0
columncount = 2

Loop

pizza:

Application.DisplayAlerts = True
Application.ScreenUpdating = True

End Sub
```

A.3.3: Mathematica - Fitting the Data

```
data=Import["desktop/AlScZr Importer.xls"][[1]];
dims=Dimensions[data]
```

```
{40,40}
```

```
axisx=Transpose[data][[1]][[2;;dims[[1]]]];
axisy=data[[1]][[2;;dims[[2]]]];
```

```
plotdata=Take[data,-dims[[1]]+1,-dims[[2]]+1];
ListPlot3D[plotdata,InterpolationOrder→3,DataRange→{{F
irst[axisx],Last[axisx]},{First[axisy],Last[axisy]},Aut
omatic},MeshStyle→Opacity[0.4],InterpolationOrder→3,Co
lorFunction→"Rainbow"]
```

```
plotdata[[2,1]]
```

```
-4.02297×10^8
```

```
ListPlot3D[plotdata,PlotTheme→"Scientific",InterpolationOrd
er→3,DataRange→{{0.0001,0.004},{0.0001,0.0039},Automatic},
MeshStyle→Opacity[0.4],InterpolationOrder→3,ColorFunction→
"Rainbow"]
```

```
General::ivar:
_{0.0001,0.0002,0.0003,0.0004,0.0005,0.0006,0.0007,0.0008,0.
0009,0.001,0.0012,0.0013,0.0014,0.0015,0.0016,0.0017,0.0018
,0.0019,□3□,0.0023,0.0024,0.0025,0.0026,0.0027,0.0028,0.002
```

9,0.003,0.0031,0.0032,0.0033,0.0034,0.0035,0.0036,0.0037,0.

0038,0.0039,0.004}_ is not a valid variable. □

```
(*data2={{axisx[[1]],axisy[[1]],plotdata[[1,1]]}};*)
data2={};
For[i=1,i<40,i++,
 For
[j=1,j<40,j++,AppendTo[data2,{axisx[[i]],axisy[[j]],plo
tdata[[j,i]]}]]]
```

data2

{{0.0001,0.0001,-3.35426×10^8},{0.0001,0.0002,-

4.02297×10^8},{0.0001,0.0003,-4.4162×10^8},{0.0001,0.0004,-

4.69665×10^8}, ≡1514≡ ,{0.004,0.0037,-

7.17936×10^8},{0.004,0.0038,-7.20907×10^8},{0.004,0.0039,-

7.23815×10^8}}

```
fit=NonlinearModelFit[data2,a1*x+a2*y+a3*x*y+a4*x^2+a5*
y^2+a6*x^3+a7*y^3+a8*x*y^2+a9*y*x^2+a10,{a1,a2,a3,a4,a5
,a6,a7,a8,a9,a10},{x,y}];
original=ListPlot3D[plotdata,InterpolationOrder→3,Data
Range→{{First[axisx],Last[axisx]},{First[axisy],Last[a
xisy]},Automatic},MeshStyle→Opacity[0.4],Interpolation
Order→3,ColorFunction→"Rainbow"];
```

Show[original,Plot3D[fit["BestFit"],{x,0,0.004},{y,0,0.004}

]]

Normal[fit]

-3.46474×10^8-3.77158×10^9 x-1.10753×10^11 x^2+6.55504×10^12 x^3-

3.08377×10^11 y+1.67575×10^10 x y+3.28663×10^11 x^2 y+1.06633×10^14

y^2-2.96439×10^11 x y^2-1.33531×10^16 y^3